

ABSTRACT

KOO, HYUNG JUN. Biologically Inspired Electronic, Photovoltaic and Microfluidic Devices Based on Aqueous Soft Matter. (Under the direction of Dr. Orlin D. Velev).

Hydrogels are a water-based soft material where three dimensional networks of hydrophilic polymer retain large amounts of water. We developed hydrogel based devices with new functionalities inspired by materials, structures and processes in nature. The advantages, such as softness, biocompatibility and high ionic conductivity, could enable hydrogels to be novel materials for biomimetic devices operated by ionic current. Moreover, microfluidic patterns are easily embedded in moldable hydrogels and allow for unique convective/diffusive transport mechanism in porous gel to be used for uniform delivery of reagent solution.

We first developed and characterized a device with unidirectional ionic current flow across a SiO_2 /Gel junction, which showed highly efficient rectification of the ionic current by non-linear conductivity of SiO_2 films. Addition of polyelectrolytes and salt to the gel layer significantly improved the performance of the new diode device because of the enhanced gel conductance.

A soft matter based diode composed of hydrogel and liquid metal (eutectic gallium indium, EGaIn) was also presented. The ability to control the thickness, and thus resistivity, of an insulating oxide skin on the metal enables the current rectification. The effect of ionic conductivity and pH on the formation of the insulating oxide was investigated in a simple model system with liquid metal/electrolyte solution or hydrogel/Pt interfaces. Finally, we present a diode composed entirely of soft materials by replacing the platinum electrode with a second liquid metal electrode.

A new type of hydrogel-based photovoltaic systems (HGPs) was constructed. Two photosensitive ionized molecules embedded in aqueous gel served as photoactive species. The HGPs showed performance comparable with or higher than those of some other biomimetic or ionic photovoltaic systems reported recently. We suggest a provisional mechanism of the device operation, based on a synergetic effect of the two dye molecules. To reduce the fabrication cost without efficiency loss, we found an inexpensive replacement of the expensive Pt counter-electrode with copper coated with carbon materials. Biologically

derived photoactive molecules, such as Chlorophyll and Photosystem II, were successfully operated in the aqueous gel of such HGPVs.

As a proof of demonstration of biomimetic structures, a light driven biomimetic reactor was developed by using hydrogel media with embedded photocatalytic TiO₂ nanoparticles. Uniform supply of the reactants and extraction of the products was accomplished via a microfluidic channel network, broadly similar to the vein structure of live leaves. The dyes were transported in the gel between the microchannels and degraded by photocatalytic oxidation by the illuminated TiO₂ particles. Quantitative analysis of the photocatalytic degradation rate of the injected dyes revealed that the microvascular reactor has high quantum efficiency per catalyst mass.

Numerical modeling was performed to explore how a soluble reagent could be supplied rapidly and efficiently through microfluidic channel networks embedded in hydrogels. The computational model takes into account the fluid transport in porous media and the solute convection and diffusion, to simulate the solute distribution and outflux with time in microfluidic hydrogel media. The effect of the channel dimensions and shapes on mass transport rapidity and efficiency was quantitatively evaluated. Experimental data proved the validity of the time dependent concentration profile calculated by the simulation.

Lastly, a microfluidic hydrogel solar cell with biomimetic regeneration functionality was demonstrated as a result of the above experimental and modeling studies. A new concept of open and replenishable photovoltaics was constructed on the basis of dye-sensitized solar cells. Photovoltaic reagents, dyes and redox electrolytes, were uniformly delivered via microfluidic networks embedded in a hydrogel, resulting in increase of photocurrent generation. The regeneration process was established, based on the pH dependence of adsorption/desorption kinetics of the dye molecules on a TiO₂ photoanode. Complete and reliable recovery of the photocurrent after an accelerated photodegradation in the biomimetic photovoltaics was demonstrated.

© Copyright 2012 by Hyung Jun Koo

All Rights Reserved

Biologically Inspired Electronic, Photovoltaic and Microfluidic Devices
Based on Aqueous Soft Matter

by
Hyung Jun Koo

A dissertation submitted to the Graduate Faculty of
North Carolina State University
in partial fulfillment of the
requirements for the degree of
Doctor of Philosophy

Chemical Engineering

Raleigh, North Carolina

2012

APPROVED BY:

Orlin D. Velev
Committee Chair

Jan Genzer

Anatoli V. Melechko

John F. Muth

Gregory N. Parsons

DEDICATION

*This dissertation is dedicated
to my wife, Ju-Hee, my daughter, Minseo (Allison),
and my parents, Noh-Geun Koo and Kyoung-Hae Jeon,
for their encouragement, support, sacrifices and love.*

BIOGRAPHY

Hyung Jun Koo was born in September, 1978 in Busan, the second largest city of South Korea with more than 3.5 million people. He graduated Yangjeong Elementary School, Dong-Eui Middle School and Yangjung High School. He lived in Busan until he moved to Seoul in 1997 to enter Seoul National University (SNU). He earned a bachelor degree in 2004 and a master degree in 2006 in Chemical and Biological Engineering from SNU. For his master's research, he developed a nanoporous thin film with a low-dielectric constant under the guidance of Dr. Kookheon Char. After receiving his degrees, he worked at the Korea Institute of Science and Technology (KIST) as a researcher for one and a half years. During the work experience, he focused on improving the efficiency of Dye-sensitized Solar Cells by utilizing a light scattering effect. He joined the Department of Chemical and Biomolecular Engineering at North Carolina State University in Fall 2007. Since then, he has been pursuing a Ph.D. degree under the guidance of Dr. Orlin D. Velev.

ACKNOWLEDGEMENTS

This work couldn't be done without many people's help and support. First and foremost, I would like to thank to my advisor, Professor Orlin D. Velev. He always gives me motivation and positive thoughts with his passion, enthusiasm and positive attitude. His intuition and accurate judgement always led me in the right direction and made work more effective. I have learned many things from him, from academic knowledge to leadership. His office door is always open and he always welcomed with his waving hand and a big smile whenever I want to talk with him. Thank you so much for everything, Dr. Velev. I was so lucky to have you as my advisor. I am really sorry that I can't hear your jokes anymore. They were so funny and hilarious!

I respectfully acknowledge Professors Jan Genzer, Anatoli Melechko, John Muth and Gregory Parsons, for serving as my committee members and for providing helpful advice. I appreciate my coworkers, Professor Michael Dickey, Dr. Slocik and Dr. Naik for their invaluable contribution to soft matter electronics and photovoltaics projects. Dr. Dickey, you are also the best advisor for my wife and I really enjoyed our collaborative work as a member of the "Fantastic Four"!

I would like to extend my appreciation to Velev group members for their assistance and helpful discussion. I appreciate Suk Tai Chang for helping me adapt to the group when I first joined and providing useful advice regarding research and group life. I thank Sejong Kim and Stoyan for their consideration and helpful discussions coming from their knowledge and experience. I enjoyed my lab life more thanks to my great classmate and sports teammate, Burak and old neighbors, Vinayak, Sumit and Elena. I was happy to work with Rachita and

Daniel on metallosoe and gel projects. Daniel was also willing to spend time to review the draft of my thesis. Of course, I am grateful to everyone in our group, Lindsey, Jairus, Liz, Jess, Stephanie, Tian, Alex, Shan and Etienne for their friendship and kind support. I would also like to thank all the staff members in our department for their help. My life at NCSU was made more fun and enjoyable thanks to my Korean department friends, Young Kuk Jhon, Jeong-Seok Na, Hyunkwan Yang, Dohan Kim, Kyoungmi Lee, Daniel (Jeong-Choel) Seo and Sangdon Han. I also had a great time with other Korean friends in the MSE, Chemistry and Textile departments, Yong-Jae Choi, Jinwoo Kim, Yohan Yoon, Yunho Kim and Hun Lee, who made me feel relaxed and refreshed.

I owe a debt to my parents for their unconditional love and endless support. They always respect my decisions and are on my side as enthusiastic supporters. I am also grateful to my parents-in-law and brother-in-law for their generous support and encouraging words. I am thankful to my sister, Yeon-Jeong, and her new family for always cheering me on and encouraging me. Lastly, but most importantly, I would like to express my deepest thanks to my wife as well as my coworker, Ju-Hee for her devotion and love. I can't imagine how I could it make through my Ph.D without her. We had our lovely daughter, Allison Min-Seo Koo, thanks to your sacrifice. I truly thank and love you.

TABLE OF CONTENTS

LIST OF TABLES	x
LIST OF FIGURES	xi
Chapter 1. General Introduction of Hydrogel Based Systems	1
1.1. Introduction	2
1.2. General Information on Hydrogels and Naturally Derived Agarose Hydrogels	2
1.3. A New Class of Diodes and Photovoltaics Based on Aqueous Soft Matter	5
<i>1.3.1. Ionic Current Diodes and Comparison of the Rectification Performance</i>	5
<i>1.3.2. Types of Conventional Solar Cells</i>	9
<i>1.3.3. Methods for Measurement of Photovoltaic Properties</i>	12
<i>1.3.4. Biomimetic Light Harvesting Systems</i>	13
<i>1.3.5. Hydrogel Based Electronics and Photovoltaics</i>	15
1.4. A New Class of Microfluidic Systems Based on Aqueous Soft Matter	17
<i>1.4.1. Unconventional Applications of Microfluidic Systems</i>	17
<i>1.4.2. Functional Microvascular Materials Based on Soft Matter</i>	19
<i>1.4.3. Hydrogel Based Microfluidic Systems</i>	21
1.5. Layout of this Dissertation	22
1.6. References	23
Chapter 2 Ion-Current Diode with Aqueous Gel/SiO₂ Nanofilm Interfaces	33
2.1. Introduction	34
2.2. Experimental Section	35
<i>2.2.1. Materials</i>	35
<i>2.2.2. Device Fabrication</i>	35
2.2.3. Measurement of Current Rectification	36
2.3. Results and Discussion	36
<i>2.3.1. Ionic Current Rectification and Agarose Concentration Effect</i>	36
<i>2.3.2. Proposed Mechanism of the Ionic Current Rectification</i>	39
<i>2.3.3. Effect of Salt and Polyelectrolyte on Rectification Performance</i>	42

2.3.4. <i>Transient Response and Long Term Stability of SNAGI Diodes</i>	44
2.4. Conclusions	46
2.5. Acknowledgements	46
2.6. References	47

Chapter 3. Ionic Current Rectification in Soft Matter Diodes with Liquid Metal

Electrodes	51
3.1. Introduction	52
3.2. Experimental Section	54
3.2.1. <i>Materials and Device Fabrication</i>	54
3.2.2. <i>I-V Measurement</i>	54
3.3. Results and Discussion	55
3.3.1 <i>Ionic current rectification at the interface of EGaIn/electrolyte/Pt</i>	55
3.3.2 <i>Effect of the conductivity and pH of the electrolyte solutions</i> <i>on the rectification at the interface of EGaIn/electrolyte/Pt</i>	60
3.3.3 <i>Ionic current rectification at the interface of EGaIn/hydrogel/Pt</i>	63
3.3.4 <i>All soft matter diodes formed using asymmetric polyelectrolyte gels</i> <i>with different pH</i>	64
3.4. Conclusions	67
3.5. Acknowledgements	68
3.6. References	68

Chapter 4. Aqueous soft matter based photovoltaic devices

4.1. Introduction	73
4.2. Experimental Section	75
4.2.1. <i>Materials and Device Fabrication</i>	75
4.2.2. <i>Measurement of Photovoltaic Properties</i>	77
4.3. Results and Discussion	77

4.3.1. Initial Evaluation of the Photovoltaic Properties	77
4.3.2. Provisional Mechanism of Photocurrent Generation of HGPVs	79
4.3.3. Ionic mechanism of HGPV operation	83
4.3.4. Low-cost flexible HGPV devices with carbon coated copper counter electrode	86
4.3.5. Biomimetic photovoltaics with biologically derived dyes	88
4.4. Conclusions	90
4.5. Acknowledgements	91
4.6. References	91

Chapter 5. Photocatalytic Hydrogel Reactor with a Microfluidic Network

Mimicking Plant Leaves	95
5.1. Introduction	96
5.2. Experimental Section	97
5.3. Results and Discussion	99
5.3.1. Transport of Injected Dye in a Hydrogel Reactor with Embedded Microfluidic Channels	99
5.3.2. Simulation for Solute Transport in Hydrogel Microfluidic Devices	99
5.3.3. Photocatalytic Reaction of Injected Dyes in the Microfluidic Hydrogel Reactor	101
5.3.4. Quantitative Analysis of Infusion and Photocatalytic Degradation Rate	104
5.3.5. Calculation of Quantum Efficiency	105
5.4. Conclusions	107
5.5. Acknowledgements	108
5.6. References	108

Chapter 6. Computational Modeling and Optimization of Solute Supply through Hydrogel Based Porous Microfluidic Devices	110
---	------------

6.1. Introduction	111
6.2. Designs of Microfluidic Channels Embedded in Hydrogel and Numerical Simulation	112
6.3. Results and Discussion	114
6.3.1. <i>Solute Transport in Porous Gels with Linear Channel Design and Numerical Parameters for Evaluation of Channel Designs</i>	114
6.3.2. <i>Effect of Secondary Branches on Rapid and Efficient Supply of Solutes</i>	119
6.3.3. <i>Comparison of Simulation and Experiment Results for Solute Transport in Microfluidic Hydrogels</i>	124
6.4. Conclusions	125
6.5. References	126
Chapter 7. Microvascular Hydrogel Photovoltaics with Biomimetic Regeneration Functionality	128
7.1. Introduction	129
7.2. Experimental Section	130
7.3. Results and Discussion	131
7.3.1. <i>Supply of Photovoltaic Reagents into μ-FGPVs</i>	131
7.3.2. <i>Development of Biomimetic Regeneration Process</i>	133
7.3.3. <i>Demonstration of Regeneration of Photo-degraded μ-FGPVs</i>	137
7.4. Conclusions	138
7.5. References	139
Chapter 8. Summary and Future Outlook	142
8.1. Summary	143
8.2. Future Outlook	145

LIST OF TABLES

Table 1.1.	Rectification ratios of ionic and organic diode systems reported in the literature	8
Table 6.1.	Numerical parameters for the evaluation of the rapidity and the efficiency of the linear channel-embedded hydrogels with different channel lengths: Molar rate, the required time (T), solute loss (C_{out}) and efficiency for 72% and 76% of coverage. The graphs of the efficiencies as a function of time are shown in Figure 6.4. C_{out} and efficiency were not obtained for the channel lengths of 1.5 cm and 2.5 cm where the 72% coverage was not achieved within 7200 s	119

LIST OF FIGURES

Figure 1.1.	(a) The primary structure of the agarose polymer without substitution of the functional groups. ¹⁸ (b) The transformation of the agarose polymer network during gelation. “a” and “b” indicate the formation of double helices and suprafibers, respectively. ¹⁸	4
Figure 1.2.	Examples of ionic-current rectifying systems. (a) Schematic diagram of the modulation of cations (red) and anions (blue) by gate bias within aligned mesoporous silica channels. ⁴² (b) Ionic current rectification within a nanochannel with asymmetric charge distribution. ⁴³ (c) Electro-mechanical mechanism of ionic current rectification through a cone-shaped nanotube where anionic DNA chains are attached. ⁴⁴ (d) A quartz-based pipet electrode for ionic current rectification. Nonlinear current response has been induced by an electrical double layer on negatively charged quartz surface at low electrolyte concentration. ⁴⁵ (e) Structure of an electrolyte diode. An ionic rectifying junction is formed in the gel cylinder. ⁴⁶	7
Figure 1.3.	Operation mechanisms of the representative types of solar cells.	10
Figure 1.4.	The J - V curve (red line) by the bias sweep method. The x and y intercepts represent the open circuit voltage (V_{oc}) and the short circuit current (J_{sc}), respectively. The area of the blue colored rectangle fitting in the J - V curve represents the actual output power.	12
Figure 1.5.	Examples of biomimetic light harvesting systems. (a) Assembly of photosystem I protein on a gold electrode with a molecular connector. ⁷⁷ (b) Anchoring of photosystem I on a surface-treated nanoporous gold substrate. Higher surface area of the gold substrate results in more uptake of the bio-photosensitive molecules. ⁷¹ (c) Schematic of the photochemical cell based on a photosystem II adsorbed gold electrode and a carbon nanotube counter electrode. ⁷⁹ (d) Schematic of the formation of a $\text{Ru}(\text{bpy})_3^{2+}$ -conjugated phospholipid/alkanethiol bilayer on a gold electrode. ⁷²	14
Figure 1.6.	Hydrogel based electronics and photoresponsive systems. (a) Structure and operating mechanism of a polyelectrolyte gel based diode. ⁶² (b) Photograph of an entirely soft memristor circuit and resistive-switching performance of individual nodes. ⁸⁹ (c) Current-voltage curves under dark and illuminated conditions of ZnO nanorods/Pt and ZnO nanorods/agarose gel/Pt systems. ⁹⁰	16

Figure 1.7.	Examples of unconventional applications of microfluidic systems. (a) Self-healing epoxy substrate with embedded three microvascular networks. ⁹⁸ Thermal control by fluid flowing through the third network (green) could accelerate the polymerization of epoxy resin (blue) and hardener (red) in a crack plane. (b) A sheath-flow microfluidic device for synthesis of homogeneous and Janus hydrogel granules. ¹⁰² (c) Control of liquid-core flow by varying the relative flow rates of the liquid cladding in the microfluidic optical waveguide. ¹⁰⁶ Right optical micrograph shows light exiting the waveguide at the end of the channels. (d) Schematic of a membraneless microfluidic fuel cell. ¹⁰⁷	18
Figure 1.8.	New functional microfluidic materials based on soft matter. (a) Soft materials of controlled shape and stiffness. ¹¹¹ Microvascular networks filled with a photocurable polymer allow to retain a certain shape with UV illumination. (b) Three-dimensional metallic microstructures embedded in a microfluidic soft matrix. ¹¹² Liquid solder was injected into the channels, followed by solidification by cooling. (c) Reversibly deformable and self-healing microfluidic antenna with liquid-metal alloy. ¹¹³ (d) An elastomeric adhesive layer with embedded microfluidic channels. ¹¹⁶ (e) Schematic and optical image of a self-healing microfluidic material filled with a polymerizable healing agent. ¹¹⁷ The healed cracks are shown in the image.	20
Figure 1.9.	Hydrogel based microfluidic systems (a) Cross-sectional images of live (green)/dead (red) staining of cells embedded in agarose gel based channels. The cells near the channels remained viable after 3 days with supply of cell culture media. ¹¹⁸ (b) Fluorescence images of an alginate gel scaffold with embedded microfluidic networks during sequential supply of fluorescein (green) and rhodamine B (red). ¹¹⁹	21
Figure 2.1.	Schematic of the structure of the SiO ₂ nanofilm/aqueous gel interface (SNAGI) diodes. The active area of agarose gel contacting the SiO ₂ layer was around 0.2 cm ² , and the thickness of the gel layer was 450 μm. Drawing not to scale.	36
Figure 2.2.	Effect of gel composition on the performance of SNAGI diode; (a) Current density as a function of applied bias. Inset: the rescaled plots to examine the current density difference in the forward bias region. (b) Current rectification ratio in terms of agarose concentration. The rectification ratios were calculated from the current density at ± 5 V bias. The dotted line is a guide to the eye. Inset: the rectification ratios of the SNAGI diode after addition of 0.05 M PSS polyelectrolyte and/or 0.05 M NaCl salt. Each point was obtained by averaging results from 4 ~	

	9 measurements except the point for the device with the pure water/SiO ₂ interfaces (0 wt. %), which was obtained by averaging data from 27 measurements.	38
Figure 2.3.	Effect of agarose gel composition on the conductance of the gel layer. The conductance values were obtained by differentiation of the I-V curves (inset). The gels were sandwiched between FTO electrodes for measurement of I-V curves. Addition of a small amount of agarose increased the conductance of the gel. Higher concentration of agarose, however, was less effective. These results are in good agreement with the trend of the rectification ratios of the SNAGI diodes in terms of agarose concentration.	39
Figure 2.4.	Proposed mechanism for nonlinear ionic conductance of SNAGI diode under forward and backward biases.	40
Figure 2.5.	Current response as a function of applied bias for SNAGI diodes with different thickness of the SiO ₂ layers. Larger negative bias is required to “turn on” the current through thicker SiO ₂ layer. The values for turn-on voltage are -3 V for 170 nm SiO ₂ and -13.3 V for 580 nm SiO ₂ , respectively. Current across the SiO ₂ layers was measured in both cases, which indicated that the tunneling may not be the dominant mechanism for the charge transport in the SiO ₂ nanofilm.	41
Figure 2.6.	Effect of salt (NaCl) concentration on the rectification ratio of SNAGI diode. Agarose gel concentration in all devices was 2 wt. %. As the amount of the salt added to the gel increased, the rectification ratio was enhanced because of the higher conductance of the gel. While the backward current did not show any dependence on the addition of salt, the current under the forward bias increased with the concentration of the salt. These results also confirmed that the introduction of the gel material improved the rectification performance. The solid lines are to guide the eye.	42
Figure 2.7.	Effect of polyelectrolytes on the rectification ratio of SNAGI diodes. All samples contain 2 wt. % agarose. For the deionization of the charged polymer backbone, polyelectrolyte-embedded gels were desalinated by washing with distilled water for 43 hours. The rectification ratio of the PSS gel devices dramatically decreased when the gel, which has positively charged mobile ions (Na ⁺), was desalinated. The slight decrease of the rectification ratio after desalination in devices without polyelectrolyte suggests that the surface conductance of the agarose gel also contributes to the ion conductance of the gel.	43

Figure 2.8.	Transient current response of SNAGI diode under AC bias with various frequencies. The SNAGI diode displayed good rectification below 100 Hz, above which, however, the rectification deteriorated because of the capacitive effects by the SiO ₂ layer and ion transfer in the gel.	45
Figure 2.9.	Forward current as a function of time from a typical SNAGI diode at a constant forward (-5V) bias. The current through the SiO ₂ nanofilm/aqueous gel interface stabilized rapidly and then remained constant for our experimental duration (~ 90 min). The gel layer contains 2 wt. % of agarose.	46
Figure 3.1.	(a) Current rectification of an EGaIn/electrolyte solution (aq)/Pt diode. The negative (forward) bias reduces the insulating oxide layer at the interface of the liquid metal. The positive (backward) bias oxidizes the liquid metal resulting in a resistive barrier for electrical current. The electrolyte is NaH ₂ PO ₄ /Na ₂ HPO ₄ buffer solution with a conductivity of 3.2 mS/cm. (b) Schematics of the experimental setup of EGaIn/electrolyte solution or water/Pt diode. The surface of the EGaIn electrode was observed under an optical microscope to obtain the images shown in Figure 3.2.	56
Figure 3.2.	Top-down optical microscope images of an EGaIn liquid metal electrode of a diode comprised of EGaIn/H ₂ O/Pt before (middle) and after (left and right) applying biases. The surface of the liquid metal is oxidized or reduced by applying + 5 V or - 5 V, respectively. The schematic of the experimental setup is shown in Figure 3.1(b).	57
Figure 3.3.	Current of an EGaIn/H ₂ O/Pt diode under repetitive (a) oxidative (+ 3 V) and (b) reductive (- 3 V) biases with time. The filled and empty arrows indicate the time when the bias was turned on and off, respectively.	58
Figure 3.4.	Current vs. time under continuous (a) reductive (- 5 V) or (b) oxidative (+ 5 V) bias. Inset in (b) is the magnified plot of (b) after 500 seconds. ...	59
Figure 3.5.	Effect of the conductivity of the electrolyte on the rectification behavior. (a) Current as a function of applied voltage of the devices with different conductivity of the electrolyte. (b) Current values and (c) rectification ratios at ± 5 V in terms of the conductivity of the electrolyte. The conductivity of the electrolyte varies by the phosphate buffer concentration. The rectification ratios were calculated from the current at ± 5 V bias. The pH of the electrolyte buffer solutions is ~ 7.	61

Figure 3.6.	Effect of pH of the electrolyte interfacing the liquid metal electrode on the rectification behavior. (a) Current as a function of voltage of the device with electrolytes of different pH values. (b) Current values at ± 5 V bias and rectification ratios in terms of pH of the electrolytes. The conductivity of the electrolyte solutions are $\sim 810 \mu\text{S}/\text{cm}$	62
Figure 3.7.	Representative I-V trace of a diode comprised of EGaIn/hydrogel/Pt. The hydrogel is made of an aqueous sodium phosphate buffer solution with a conductivity of $31 \text{ mS}/\text{cm}$	63
Figure 3.8.	(a) Photograph of a prototype diode composed entirely of soft matter. (b) Current as a function of applied voltage and (c) transient voltage response of the soft matter diode under AC signal. The EGaIn interfacing the PEI gel is grounded. The output voltage is the voltage applied to the diode under AC bias with amplitude of $\pm 3 \text{ V}$. (d) A schematic depiction of the soft matter diode with asymmetrically configured polyelectrolyte gels under forward and backward biases.	65
Figure 3.9.	(a) Current as a function of applied voltage and (b) transient voltage response under wave AC field of the Pt/PEI gel/PAA gel/Pt device. The slight asymmetry of the output signals may result from the interface between two different polyelectrolyte gels.	66
Figure 4.1.	Schematic of the hydrogel photovoltaic cells (HGPs). The dyes were originally infused into two different agarose gel layers as shown here, but over time the dyes became redistributed because of diffusion in the aqueous gel.	76
Figure 4.2.	(a) Typical J - V curves of gel photovoltaic cell prototypes under dark conditions and after illumination for increasing times. The bias was swept from -0.9 V to 0.1 V at a rate of $14 \text{ mV}/\text{s}$. The light source was a fiber optic illuminator. (b) The effect of dye concentration on photovoltaic performance. When the dye concentration was increased 3 times ($7.5 \times 10^{-8} \text{ mol}$ in each gel layer) than that of the prototype device ($2.5 \times 10^{-8} \text{ mol}$ in each gel layer), both photovoltaic parameters, J_{sc} and V_{oc} , were improved by 125% and 67%, respectively. The bias was swept from -0.6 V to 0.1 V at a sweep rate of $\sim 9.5 \text{ mV}/\text{s}$	78
Figure 4.3.	The photocurrent responses in terms of the original position of the dyes: (a) DAS^- and (b) $[\text{Ru}(\text{bpy})_3]^{2+}$. The light was turned on at time = 10 s. The currents level off as the diffusing dyes redistribute through the hydrogel.	80

Figure 4.4.	Provisional mechanism for the operation of the hydrogel based photovoltaic devices.	81
Figure 4.5.	UV-Vis absorption spectra of DAS ⁻ and [Ru(bpy) ₃] ²⁺ dyes. The energy gaps between the HOMO and LUMO of the DAS ⁻ and the [Ru(bpy) ₃] ²⁺ dyes for the provisional mechanism were estimated from the wavelength values at the maximum peak position.	82
Figure 4.6.	Photocurrent densities as a function of time and original dye location. (a) DAS ⁻ was added to the device first, followed by [Ru(bpy) ₃] ²⁺ addition. (b) [Ru(bpy) ₃] ²⁺ was added to the device first, followed by DAS ⁻ . Both results show large increase of photocurrent densities when the other dye was introduced. The light was turned on at 10 seconds.	83
Figure 4.7.	Photocurrent responses of (a) HGPVs and (b) DSSCs under dark and illumination conditions. White and black arrows represent the times when the light was turned on and off, respectively.	84
Figure 4.8.	Examples of the transient characteristics of the photovoltaic properties of HGPVs: (a) photocurrent density at V = 0 V and (b) photovoltage at zero current. The arrows indicate the saturated values of J _{sc} and V _{oc} . The light intensity was ~ 88 mW/cm ² . The photovoltage was recorded from four subsequent measurements under continuous illumination. The three spikes in (b) result from restarting the source meter and illustrate the slow establishment of the open circuit voltage. The light was turned on at 10 seconds for both measurement and was turned off at ~400 seconds for J _{sc} measurement.	85
Figure 4.9.	(a) Data comparison illustrating the effect of carbon nanotube coating on the photovoltaic performance compared to the one of uncoated Pt and Cu electrodes. The amount of the carbon nanotube coated on the Cu electrode was ~ 0.03 mg/cm ² . (b) J-V characteristics of a prototype flexible HGPV cell, where the Cu foil coated with graphite/carbon black mixture was used as a counter electrode. (c) Photograph of the real prototype flexible device with an active area ~125 mm ² . The light intensity was ~180 mW/cm ² . All of the samples were characterized after illumination for 5 min.	87
Figure 4.10.	(a) Photocurrent densities and (b) photovoltage of gel-based cells operating on biological photosynthesizing complexes. The red arrows indicate the time when the light turned on.	89

Figure 5.1.	(a) Schematics of the light-driven microvascular gel reactor. The TiO ₂ -embedded hydrogel with the branched channel network was enclosed in a PDMS spacer and sandwiched by two glass substrates. Two pieces of Tygon tubing were inserted into the inlet and outlet of the device for supply of a reactant and drainage of the processed solution. (b) Photograph of the TiO ₂ -embedded gel with the microfluidic network. The white arrows point to examples of larger TiO ₂ particle aggregates inside the hydrogel medium. The TiO ₂ composition was lowered to 0.5 wt.% in this gel for clear observation of the particles. Top view images of the microfluidic gel reactor after the injection of a solution of 1 mM Allura Red and 1 mM Methylene Blue dyes for (c) 30 min and (d) 60 min.	97
Figure 5.2.	SEM images of the dried agarose gel with the embedded TiO ₂ particles. Note that the sub-micron clusters of the TiO ₂ catalyst are uniformly dispersed throughout the gel matrix.	98
Figure 5.3.	Simulation result for the dye penetration through the gel-microvascular network after dye injection for 30, 60 and 120 min. The rectangle with dotted lines in the image for 120 min indicates the “reaction area” through which most of the dye solution flows under illumination.	100
Figure 5.4.	Temporal distribution of the dye mixture solution (0.2 mM Methylene Blue and 0.2 mM Allura Red) as a function of time. The UV illumination started 220 min after the dye injection and continued for 50 min. The flow pattern of the partially degraded dye under the UV light for 3 min is shown in Figure 5.5. Asterisks (*) denote images taken during the post-illumination recovery.	101
Figure 5.5.	Partial degradation of the Methylene Blue and Allura Red dye in the light-driven gel reactor (a) before and (b) after UV illumination for 3 min. The dye solutions were continuously supplied during the UV illumination. The concentration of both dyes in the mixed solution is 1 mM. The area surrounded by the dotted line is a non-reactive region, where the photocatalytic reaction does not take place because of the absence of TiO ₂ catalyst.	102
Figure 5.6.	(a) Effect of the presence of TiO ₂ particles on the color change of the solution of Allura Red and Methylene Blue dye mixture under UV illumination. (b) UV-vis absorption spectra of the dye solutions in (a). The absorbance of both dyes with TiO ₂ catalysts drastically decreases under UV illumination. Thus, TiO ₂ particles facilitate the degradation of the dyes even though a slight degradation of the Allura Red in the dye solution without TiO ₂ catalyst was observed. The Allura Red dye may be more susceptible to UV degradation.	103

Figure 5.7.	UV-vis absorption spectra of the dye solution exiting the light-driven gel reactor (a) before, (b) during and (c) after UV illumination. The time interval between the spectra collection is 30 min for (a) and (c) and 10 min for (b). (d) The absorbance peak intensity of the solution exiting the light-driven gel reactor as a function of time. The intensity was measured at 524 nm and 670 nm, which are the maximum absorption wavelengths of Allura Red and Methylene Blue in water, respectively. ...	104
Figure 5.8.	UV-vis absorbance of the solution exiting the TiO ₂ -hydrogel reactor as a function of (a) time and (b) UV-vis spectra at the “Pseudo-steady states”. The device was illuminated from 145 min to 330 min indicated by the red-colored box. The light was incident from the channel side of the microfluidic device. The collected solution was diluted before UV-vis absorption measurement at 640 nm. It was confirmed that the absorbance intensity is linearly proportional to the concentration of the dye solution in the concentration regime used for the measurement.	107
Figure 6.1.	(a) A linear microfluidic design for finite element calculations. Light-green colored region is filled with porous hydrogel. The rectangle enclosed by the dotted lines indicates “active area” where solutes are supposed to be supplied. Solute concentration and efficiency of the device is calculated within this area. (b) Three representative designs of porous microfluidic channels compared in this study. Not to scale.	112
Figure 6.2.	Simulation results for solute distribution at various points of time in linear-microfluidic gel devices with different channel length (L). The arrows in the device with 2.95 cm long channels indicate the direct drainage from the source channels to the outlet.	115
Figure 6.3.	Degree of solute penetration of the linear-microfluidic gel devices with different channel lengths as a function of time. The area of solute coverage was obtained by using Photoshop. Two dotted lines represent 72% and 76% of coverage in the active area.	116
Figure 6.4.	(a) The amount of the reagent loss and (b) the efficiency as a function of time in linear-microfluidic gel devices with different channel length.	118
Figure 6.5.	(a-c) Simulation results for solute distribution at 2700 s in T-shaped channel-embedded hydrogels with different channel lengths. (a) 2.5 cm, (b) 2.75 cm, (c) 2.95 cm. (d) Simulation results for solute distribution at 2700 s in branched channel-embedded gels. The channel length is 2.75 cm. The length of secondary branches from the primary channels is 1.5 mm in all designs.	120

Figure 6.6.	Comparison of the molar injection rate of solute, the time for 76% solute coverage, the solute loss and the efficiency at $T_{76\%}$ between linear and T-shaped channels with different lengths of the primary channels.	121
Figure 6.7.	Comparison of the molar injection rate of solute, the time for 76% solute coverage, the solute loss and the efficiency at $T_{76\%}$ of microfluidic devices with linear, T-shaped and branched channels. The primary channel length is 2.75 cm in all devices.	122
Figure 6.8.	Simulation results for reagent distribution at 2700 s in T-shaped microfluidic devices with different branch length. (a) no tail (linear channels), (b) 0.5 cm, (c) 1.0 cm, (d) 1.5 cm.	123
Figure 6.9.	The effect of the length of the secondary branches in T-shaped design on (a) the solute loss and (b) the efficiency at $T_{76\%}$	124
Figure 6.10.	Comparison of simulation and experiment results for time-lapse dye transport in hydrogel microfluidic devices. (a) 5 min, (b) 10 min, (c) 20 min and (d) 30 min after injection of the dye solution.	125
Figure 7.1.	(a) A schematic cross-section view of the μ -FGPVs. (b) A photograph of the prototype device of the μ -FGPVs.	130
Figure 7.2.	(a) Images illustrating the infusion of dye and electrolytes through the gel-vascular network at 5 and 15 min after injection of the solution. The injection rate is 10 μ l/min. (b) I-V curves of the μ -FGPVs under illuminated condition after the injection of the aqueous solution of dye and electrolytes. The device is illuminated with a solar simulator with 300 W Xenon lamp (100 mW/cm ² , New Port).	132
Figure 7.3.	The distribution of Peclet number in the μ -FGPVs. The graph on the right shows the Peclet numbers along the dotted line on the left figure. ...	133
Figure 7.4.	(a) The regeneration process of the μ -FGPVs. (b) Repetitive recovery of the photocurrent exhibited by the μ -FGPVs.	134
Figure 7.5.	(a) I-V curves of the μ -FGPVs after different regeneration process, showing the importance of the activation step. The device (1) was washed with aqueous NaOH solution for 3 hrs, followed by treating with aqueous HCl solution for 3 hrs before the dye replenishment. The devices (2) and (3) were washed with H ₂ O or aqueous NaOH solution for 6 hrs, respectively, before the dye replenishment. All samples were measured after the 1hr dye-supply step. (b) Effect of the activation	

duration on the regeneration efficiency of the μ -FGPVs. The injection rate of all solutions is 10 μ l/min. 136

Figure 7.6. (Left) TiO_2 films before and after the intense UV illumination. The photographs were taken under illumination. (Right) The effect of UV illumination time on the photovoltaic performance of the μ -FGPVs. 137

Figure 7.7. Demonstration of the photocurrent recovery of the μ -FGPVs after accelerated degradation by intense UV. W/A stands for the washing and activation steps. The device was washed and activated for 5 hr each. The violet and the red colored regions represent the periods of UV illumination and the dye replenishment, respectively. 138

Chapter 1

General Introduction of Hydrogel Based Systems

1.1. Introduction

The main objective of my doctoral research is to create new functionalities for hydrogel based devices. Hydrogels are a form of organic soft matter made of highly hydrated polymer networks. Due to their high water content, the hydrogels are generally ion-conductive and biologically inert. Hydrogels are widely used in biology research for various applications ranging from biomolecule separation to cell encapsulation. The advantages of ionic conductivity and biocompatibility enable hydrogels to serve as a novel medium for biomimetic devices, which operate based on ionic currents, inspired by important processes in living organisms, such as energy transfer, metabolism and neural transmission. The main body of my thesis describes how to develop electronic, photovoltaic and microfluidic devices based on hydrogel media. Prior to discussing the results of my graduate research, this chapter provides basic information on hydrogels and briefly reviews the recent development of bio-inspired electronic and photovoltaic devices as well as new applications of microfluidic systems and materials.

1.2. General Information on Hydrogels and Naturally Derived Agarose Hydrogels

Hydrogels are water-based soft matter systems composed of hydrophilic polymer networks which are hydrated and swollen, but insoluble in water. Due to their high water content, hydrogels are generally biocompatible, and therefore, have been used for many bio-related applications,¹ e.g. biosensors,^{2,3} bioassays,^{4,5} scaffolds for tissue engineering,⁶⁻¹⁰ drug delivery¹¹⁻¹⁵ and media for cell encapsulation¹⁶ and separation.¹⁷ Hydrogel network polymers are classified into naturally derived polymers and synthetic polymers. Representative network-forming polymers derived from nature include fibrin, collagen, gelatin, starch, hyaluronic acid, alginate and agarose. Examples of synthetic network polymers include poly(acrylic acid) (PAA), poly(ethylene glycol) (PEG), poly(vinyl alcohol) (PEG), poly(N-isopropylacrylamide) (PNIPAAm) and their derivatives or copolymers. Generally, hydrogels from natural polymers are more biocompatible and even biodegradable depending on the molecular weight, thereby being more preferable for biological applications. Moreover, the preparation procedure for naturally derived hydrogels does not require use of any toxic

chemical reagents. On the other hand, hydrogels from synthetic polymers have comparatively well-defined chemical structure, which can be finely tuned to control the physical and chemical properties of the hydrogel.

An agarose gel, one of the naturally derived hydrogels, typically contains ~ 99% of water and ~ 1% of agarose polymer. Agarose is derived from agar, which is a constituent of the cell walls or the intercellular matrix of marine red algae (*Rhodophyta*).¹⁸ Agar is separated by the adsorption and precipitation into two sub-fractions; anion-free agarose and anion-rich agarpectin. However, commercial agarose polymer generally contains sufficient amounts of the charged functional groups.¹⁸ Agarose gels maintain a solid medium with ionic conductivity and electrochemical properties comparable with those of aqueous phase.¹⁹ Agarose gel is one of the most used media for electrophoretic separation of proteins or biopolyanions, such as DNA and RNA. For the same polymer concentration, agarose gel has relatively high mechanical strength compared to other popular gel media for the gel electrophoresis, such as the starch gel and the polyacrylamide gel.¹⁸ Agarose gel has also been shown to be biocompatible by *in vivo* implantation study of a cell embedded agarose gel.²⁰

The agarose network in the gel consists of a repeating disaccharide unit, called agarobiose. The primary structure of the agarose polymer is shown in Figure 1.1 (a).¹⁸ Two monosaccharides, β -D-galactopyranose and 3,6-anhydro- α -L-galactose, constitute the agarobiose. Single strands of agarose have an average molecular weight about 1.2×10^5 , which is equivalent to about 392 agarobiose subunits. Hydroxyl groups are the main functional group of the agarose network, while the majority of the substituted functional groups include sulfate, pyruvate and methoxyl groups. There is possibly a small amount of other functional groups, including L-galactose, D-xylose and D-glucuronic acid.¹⁸

Agarose gel is prepared by cooling a hot aqueous agarose solution to its gelling temperature, ranging from 15 to 37 °C depending on agarose concentration.¹⁶ Due to physical crosslinking, the sol-gel transformation of the agarose gel is thermally reversible. During gelation, the single strands of the agarose polymer form double helices, presumably followed by the formation of suprafibers by further aggregation of the double helices by hydrophobic

interaction and hydrogen bonding (Figure 1.1 (b)).¹⁸ The 3-D network of the agarose suprafibers entraps water to produce a hydrogel. The hydrated volume fraction of the agarose polymer is comparable to the weight fraction of the agarose in the agarose gel.²¹

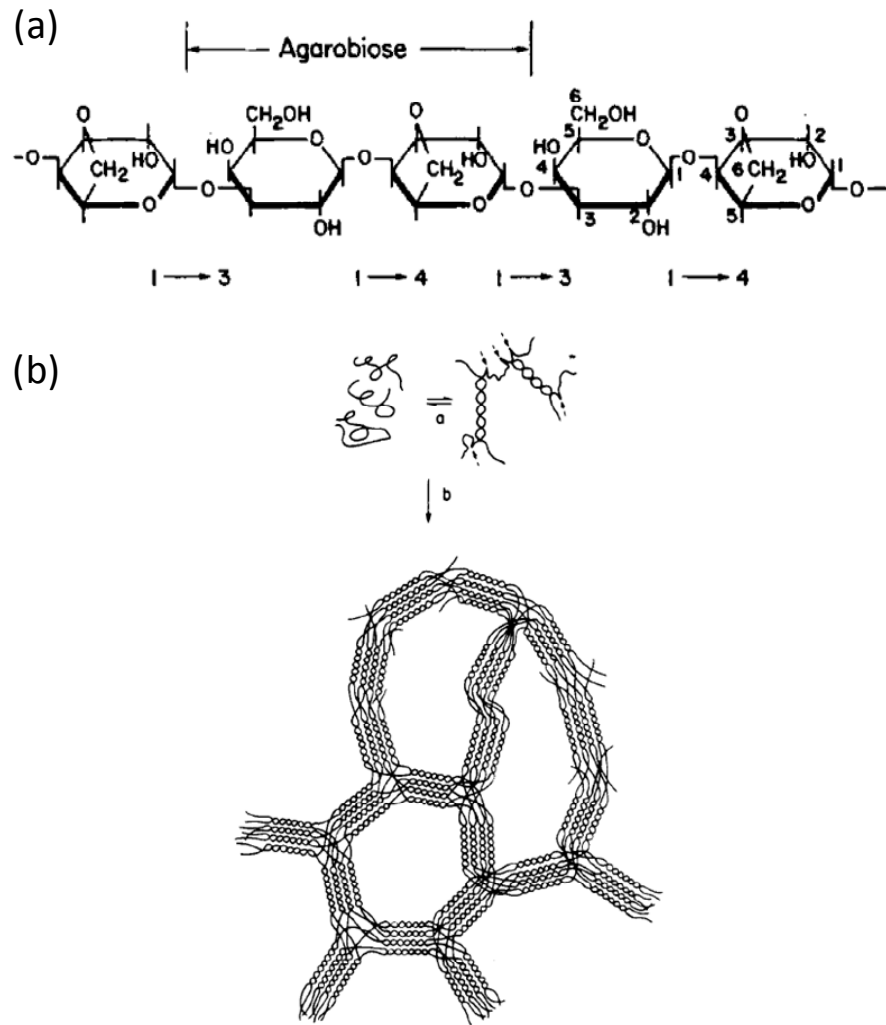


Figure 1.1. (a) The primary structure of the agarose polymer without substitution of the functional groups.¹⁸ (b) The transformation of the agarose polymer network during gelation. “a” and “b” indicate the formation of double helices and suprafibers, respectively.¹⁸

The physical and chemical properties of the naturally derived agarose gel, such as the functional groups, the charge density and the pore size, can vary from sample to sample. The functional groups in agarose backbones are negatively charged when ionized. The maximum

charge density, mostly resulting from the ionization of the pyruvic and sulfonic groups, is approximately 6.1×10^{-2} mol or 5.9×10^3 C per 1 kg of dry agarose.²² The surface charge of the agarose backbones depends on pH and is maximized at pH above 3.5. The negatively charged functional groups on the agarose backbones influence the diffusion coefficient of charged species by exhibiting attractive and repulsive interactions with cations and anions, respectively. For example, the diffusion coefficient of the cationic species decreases because of the attractive interaction with the negatively charged agarose backbones at low ionic strength. The surface charges in the agarose gel are screened when ionic strength is higher than $\sim 10^{-2}$ M.

The permeability of the porous agarose gel is an important parameter for its application as a matrix for cell-growth or propagation and a substrate for chromatography or electrophoresis. The hydraulic permeability of the agarose gel depends on the applied pressure and the agarose concentration. It was reported that the average permeability of the agarose gel at 20 kPa of applied pressure was 353 nm^2 for ~ 2 wt.% agarose and 25 nm^2 for ~ 5.5 wt.% agarose.²³ The pore size of an agarose matrix widely ranges from 1 to 900 nm depending on the agarose concentration.²⁴⁻²⁶ A study of diffusion of charged species in the agarose gel also enabled the estimation of the average pore size of ~ 36 nm for the gel with ~ 1.5 wt.% agarose.²²

1.3. A New Class of Diodes and Photovoltaics Based on Aqueous Soft Matter

1.3.1. Ionic Current Diodes and Comparison of the Rectification Performance

A diode is a basic electronic component which exhibits current rectification by allowing electric current in one direction and inhibiting current in the other direction. Various kinds of electronic diodes have been proposed using single molecules,²⁷⁻²⁹ carbon nanotubes,³⁰⁻³² nanoparticles^{33, 34} and conducting polymers.³⁵⁻³⁷ Rather than electronic current rectification, there has been recent interest in devices with nonlinear ionic current, which is a basic mechanism of essential processes in the human body, such as adenosine triphosphate (ATP) synthesis and neural transmission. Due to the capability of operation in water phase, ionic

current diodes could find a range of bio-related applications, such as sensing, separation and manipulation of biomolecules.

Ionic current can be modulated by electrostatic interactions with wall surface charges in a confined geometry at small scales.³⁸ Electric potential away from the charged surface, Ψ , exponentially decays by the equation, $\Psi(x) \approx \Psi_s \exp\left(-\frac{x}{1/\kappa}\right)$, where Ψ_s is the potential difference between the surface and the bulk, x is the distance from the surface and $1/\kappa$ is the characteristic length known as the Debye length.³⁹ Since the Debye length of aqueous solutions is usually less than 100 nm, fluidic channels with nano-sized domains could control ionic flows by modifying the surface charge of the channel walls. A theoretical study on the selective ion current in a single nanochannel has been performed, where the effects of the channel dimensions, electrolyte concentration, applied bias and surface charge density on the ionic current selectivity have been investigated.⁴⁰ Nonlinear current leakage has been also observed in electrolyte/SiO₂ nanochannels/Si interfaces.⁴¹ Application of a parallel voltage to the underlying Si substrate has been proposed to avoid the unwanted field distortion caused by the current leakage. Fan *et al.* reported selective transport of proton ions in aligned mesoporous silica channels (Figure 1.2(a)).⁴² The conductance of the positively charged ions through the silica channels depended on the pH environment and salt concentration, which proved the electrostatic gating of the mesoporous channels with negatively charged walls.

Asymmetry is a key component for unidirectional current of electrons or ions. An asymmetric distribution of the surface charge on the ion channel walls could be one reason for ionic current rectification. Daiguji *et al.* theoretically proved that a nanofluidic diode can be realized when the surface of either half of the channel is oppositely charged as shown in Figure 1.2(b).⁴³ The possible design of a nanofluidic bipolar transistor was further proposed on the basis of the study on the nanofluidic diode. Karnik *et al.* demonstrated nanofluidic diodes with asymmetric charge distribution by modifying a half of the neutral surface of biotin-adsorbed channel with the positively charged avidin proteins.⁴⁷ Gracheva *et al.* proposed a design of an electrically tunable rectifying membrane consisting of p-n semiconductor layers.⁴⁸

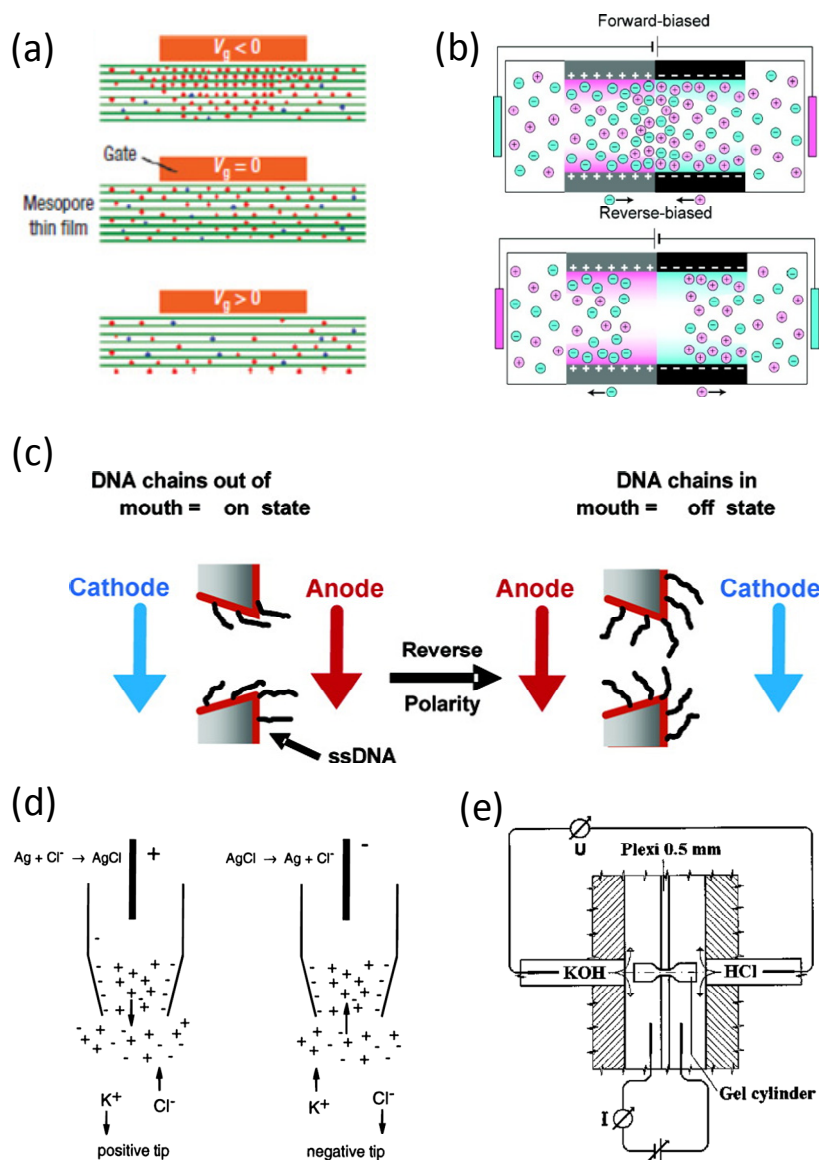


Figure 1.2. Examples of ionic-current rectifying systems. (a) Schematic diagram of the modulation of cations (red) and anions (blue) by gate bias within aligned mesoporous silica channels.⁴² (b) Ionic current rectification within a nanochannel with asymmetric charge distribution.⁴³ (c) Electro-mechanical mechanism of ionic current rectification through a cone-shaped nanotube where anionic DNA chains are attached.⁴⁴ (d) A quartz-based pipet electrode for ionic current rectification. Nonlinear current response has been induced by an electrical double layer on negatively charged quartz surface at low electrolyte concentration.⁴⁵ (e) Structure of an electrolyte diode. An ionic rectifying junction is formed in the gel cylinder.⁴⁶

Table 1.1. Rectification ratios of ionic and organic diode systems reported in the literature

Title and authors	Rectification ratios (sweep bias)
Ionic current diodes	
Ionic Circuits Based on Polyelectrolyte Diodes on a Microchip, Han <i>et al.</i> ⁵⁷	~ 100 ($\pm 1V$)
Nanofluidic Diodes Based on Nanotube Heterojunctions, Yan <i>et al.</i> ⁵⁸	~5 ($\pm 5V$)
Electromigration Current Rectification in a Cylindrical Nanopore Due to Asymmetric Concentration Polarization, Jung <i>et al.</i> ⁵⁹	~2 ($\pm 3V$)
Single Conical Nanopores Displaying pH-Tunable Rectifying Characteristics. Manipulating Ionic Transport With Zwitterionic Polymer Brushes, Yameen <i>et al.</i> ⁶⁰	22 ($\pm 2V$)
Ionic Current Rectification, Breakdown, and Switching in Heterogeneous Oxide Nanofluidic Devices, Cheng <i>et al.</i> ⁶¹	321 ($\pm 1V$)
Polyelectrolyte Diode: Nonlinear Current Response of a Junction between Aqueous Ionic Gels, Cayre <i>et al.</i> ⁶²	~40 ($\pm 5V$)
Nanofluidic Diode, Vlasiouk <i>et al.</i> ⁶³	217 ($\pm 5V$)
Nonlinear effects of electrolyte diodes and transistors in a polymer gel medium, Hegedüs <i>et al.</i> ⁴⁶	~40 ($\pm 5V$)
Organic materials based diodes	
Understanding the Anchoring Group Effect of Molecular Diodes on Rectification, Lee <i>et al.</i> ²⁸	7.4 ($\pm 1.5V$)
Long-Lifetime Polymer Light-Emitting Electrochemical Cells, Shao <i>et al.</i> ⁶⁴	~10000 ($\pm 3V$)
Self-Assembled, Chemically Fixed Homojunctions in Semiconducting Polymers, Leger <i>et al.</i> ³⁵	90 ($\pm 4V$)
Rectifying Diodes from Asymmetrically Functionalized Single-Wall Carbon Nanotubes, Wei <i>et al.</i> ³¹	1000 ($\pm 1V$)
Molecules that mimic Schottky diodes, Ashwell <i>et al.</i> ⁶⁵	3000 ($\pm 1V$)
A Conjugated Polymer pn Junction, Cheng <i>et al.</i> ³⁶	7 ($\pm 2 V$)
Molecular Rectifying Diodes from Self-Assembly on Silicon, Lenfant <i>et al.</i> ⁶⁶	37 ($\pm 1V$)
Electric current rectification by an all-organic electrochemical device, Chen <i>et al.</i> ⁶⁷	100 ($\pm 3 V$)
Molecular Rectification in a Metal–Insulator–Metal Junction Based on Self-Assembled Monolayers, Chabinyk <i>et al.</i> ⁶⁸	~10 ($\pm 1V$)
Rectification and Nonlinear Optical Properties of a Langmuir–Blodgett Monolayer of a Pyridinium Dye, Baldwin <i>et al.</i> ⁶⁹	~90 ($\sim\pm 2 V$)

The asymmetric geometry of various types of ion channels may also enable ionic current rectification. Siwy and coworkers have performed both theoretical and experimental studies on selectivity and rectification of ionic current in cone-shaped nanochannels.^{38,40,49,50}

DNA attached cone-shaped nanopores were proposed as artificial ion channels where ionic current is rectified via electromechanical mechanism of the bio-polyanions (Figure 1.2(c)).⁴⁴ A pH-tunable nanofluidic diode with a cone shaped amphoteric nanopore has also been reported.⁵¹ Similarly, ionic current rectification has been measured in nanopipettes with tapered openings (Figure 1.2(d)).^{45,52}

On a large scale, extensive studies on the ionic current rectification at a junction of acidic and basic electrolytes have been performed.^{46,53-56} The rectifying junction of the electrolyte diode is formed in the hydrogel bridge which connects two electrolyte reservoirs. During reverse bias, H^+ and OH^- ions migrating from the electrolytes form water at the junction, which is analogous to a depletion region formed by hole (h^+)/electron (e^-) carriers in a p-n junction diode.

The rectification ratio is one of the important parameters to evaluate the diode performance. This ratio is calculated by dividing the current in the allowed direction (i.e. forward current) by the current in the forbidden direction (i.e. backward current) at a specific bias. Recently reported rectification ratios of various ionic current diodes and organic material based diodes are summarized in Table 1.1.

1.3.2. Types of Conventional Solar Cells

The interest in clean, sustainable and environmentally-friendly alternative energy sources is growing rapidly. Solar energy is one of the most promising candidates for a next generation energy source. The solar energy reaching the Earth is 10^4 times larger than the energy consumed by the global population. In principle, if solar cells with 10% conversion efficiency covered only 0.1% of total earth surface, all of the energy we need can be supplied from the sunlight. The solar cells are largely classified by three types: Inorganic p-n junction solar cells, Organic photovoltaics (OPVs) and Dye sensitized solar cells (DSSCs). Figure 1.3 schematically shows these types of solar cells. Inorganic p-n junction solar cells are the most conventional among the types introduced above. Inorganic solar cells have been actively studied since the middle of 19th century when Bell laboratories accidentally found the

photovoltaic effect in a Si p-n junction.⁷⁰ The general mechanism for inorganic p-n junction solar cells is as follows:

1. The device absorbs light and electrons in the lattice of inorganic materials are excited. (Electron-hole pair generation)
2. The electron-hole pair is separated at the p-n junction. The electrons and holes are transported in one direction by an induced electric field and directed to the external circuit. (Electron-hole pair separation)

The imbalance of electrons and holes at the interface of the p-type and n-type materials creates the electrostatic field which separates the electron-holes pairs and moves them after they are generated. In inorganic solar cells, the wavelength of the absorbed light and the output voltage depend on the band-gap of the inorganic semiconducting materials. The maximum efficiency of inorganic solar cells so far is ~40% and the inorganic materials used are silicon, cadmium telluride (CdTe), copper indium gallium selenide (CIGS) and others.

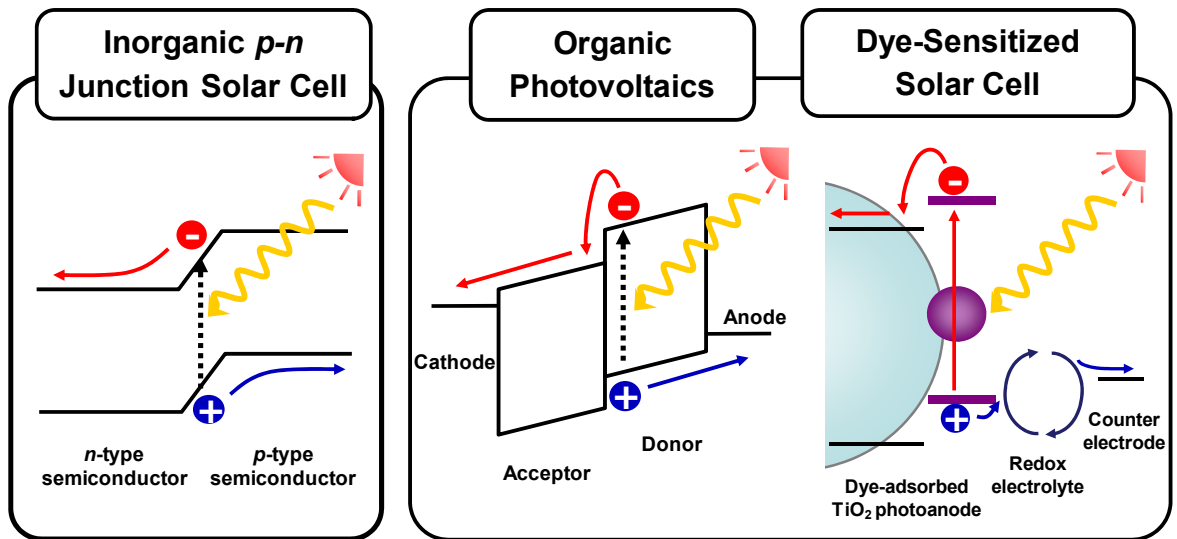


Figure 1.3. Operation mechanisms of the representative types of solar cells.

Even though the efficiency of the inorganic solar cells is sufficiently high, the commercialization of this type of solar cells has been hampered by high production costs. Organic photovoltaics (OPVs) are able to reduce production costs by replacing expensive inorganic materials with the low cost organic polymers. The mechanism of OPVs is similar to that of the inorganic p-n junction solar cells (Figure 1.3). The electron donor and acceptor organic polymers are brought into contact, analogous to the p-n junction of the inorganic solar cells. The electron-hole pairs are generated in the donor organic polymer layers and diffuse through the system. When the pairs reach the donor and acceptor interface, the electrons are captured by the electron acceptor and the electron-hole pairs are effectively separated. Polyphenylene vinylene and its derivatives, phthalocyanine, pentacene, etc. are commonly used as electron donor materials and carbon fullerenes and their derivatives (e.g. Phenyl-C61-butyric acid methyl ester (PCBM)) are usually used as electron acceptors. OPVs are potentially low-cost, light weight and flexible. However, the maximum reported efficiency is ~6%, which is not high enough for practical use. Improving the efficiency is limited by the short lifetime of the electron-hole pairs. The polymer materials are also unstable and degrade easily in the air.

Dye sensitized solar cells (DSSCs) are another candidate toward solving the high production cost of the inorganic solar cells. DSSCs usually consist of 4 parts: Large bandgap semiconducting materials, photosensitive dyes, redox electrolytes and counter electrodes. The large bandgap semiconducting materials, such as TiO_2 and ZnO , hardly absorb the sun light at the visible wavelength region which occupies more than 40% of the sun light. The dye molecules are adsorbed on the surface of the semiconducting materials to absorb visible light. Electrons in HOMO of the dye molecules are excited to LUMO by visible light, followed by injection of the excited electrons to the conduction band of the semiconducting materials as shown in Figure 1.3. The injected electrons are transported to the external electrode by diffusion. The oxidized dyes are regenerated by the electrolyte. The electrolyte carries the electrons from the counter electrode to the oxidized dyes. DSSCs have low production cost compared to inorganic solar cells and exhibit a maximum efficiency of ~12%

so far. However, they also have some drawbacks, for example, dye degradation by UV light or heat, the limited lifetime of the dyes and leakage of the liquid electrolyte.

1.3.3. Methods for Measurement of Photovoltaic Properties

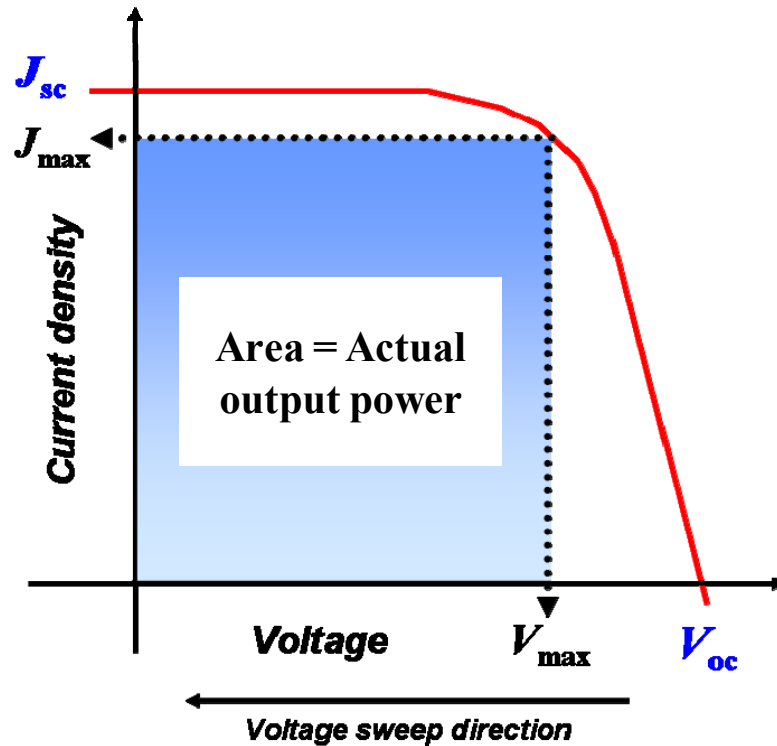


Figure 1.4. The J - V curve (red line) by the bias sweep method. The x and y intercepts represent the open circuit voltage (V_{oc}) and the short circuit current (J_{sc}), respectively. The area of the blue colored rectangle fitting in the J - V curve represents the actual output power.

The commonly accepted method to measure photovoltaic properties is to record the current densities while sweeping the voltage under illumination. For this thesis, this method will be referred to as the “bias sweep method”. An example of the resulting curve is shown in Figure 1.4. The x and y intercepts represent the open circuit voltage (V_{oc}) and the short circuit current (J_{sc}) of the photovoltaic devices, respectively. The actual power generated by the cell is less than the multiplication of J_{sc} and V_{oc} because the curve is not an exact rectangle. To

calculate the actual power of the device, a correction factor is required which is called “*fill factor (FF)*”. *FF* is the ratio of the maximum actual output power to the value by multiplying J_{sc} and V_{oc} . *FF* is normally associated with the resistance of the cell devices. Lower series resistance and higher shunt resistance result in higher *FF*. The actual output power of the cells can be obtained by multiplying J_{sc} , V_{oc} and *FF*. The efficiency of the cells is calculated by dividing the output power by the input power of the light source as summarized in the equation below.

$$\eta(\text{efficiency}) = \frac{P_{out}}{P_{input}} = \frac{J_{max} \times V_{max}}{P_{input}} = \frac{J_{sc} \times V_{oc} \times ff}{P_{input}}$$

Another method for photovoltaic property evaluation is to measure the current or the voltage response as a function of time. This method is sometimes used to measure the small current densities or voltages from new photovoltaic systems.⁷¹⁻⁷³ This method is especially useful when the transient characteristics in photovoltaic response are investigated or the system is easily affected by the external bias, such as an ionic system. However, the fill factor and the output power cannot be obtained from this method.

1.3.4. Biomimetic Light Harvesting Systems

As opposed to photovoltaic devices made by humans, nature already has its own solar harvesting system which is a plant leaf. Over the last few decades, much research has been done on a biomimetic light harvesting systems, to utilize advantages of the natural leaf developed by evolution for more than 4 billion years. Many biomimetic prototypes for generation of photoelectricity or solar fuels have been reported based on photosynthetic biomaterials, such as chloroplast and its subunits.^{71,74-79} Meunier *et al.* reported photosynthetic oxygen production with a stable thylakoid, a sub-unit of the chloroplast, entrapped within porous silica gel.⁷⁵ Terasaki *et al.*^{76,77} and Ciesielski *et al.*^{71,78} demonstrated photocurrent generation by using photosystems self-assembled on a gold electrode (Figure 1.5(a) and (b)). The photosystems are protein complexes in a thylakoid membrane, involved in photosynthesis. Yehezkeli *et al.*⁷⁹ reported a photoelectrochemical cell based on a

photosystem II-modified photoelectrode, which produced photocurrent by light-induced oxidation (Figure 1.5(c)).

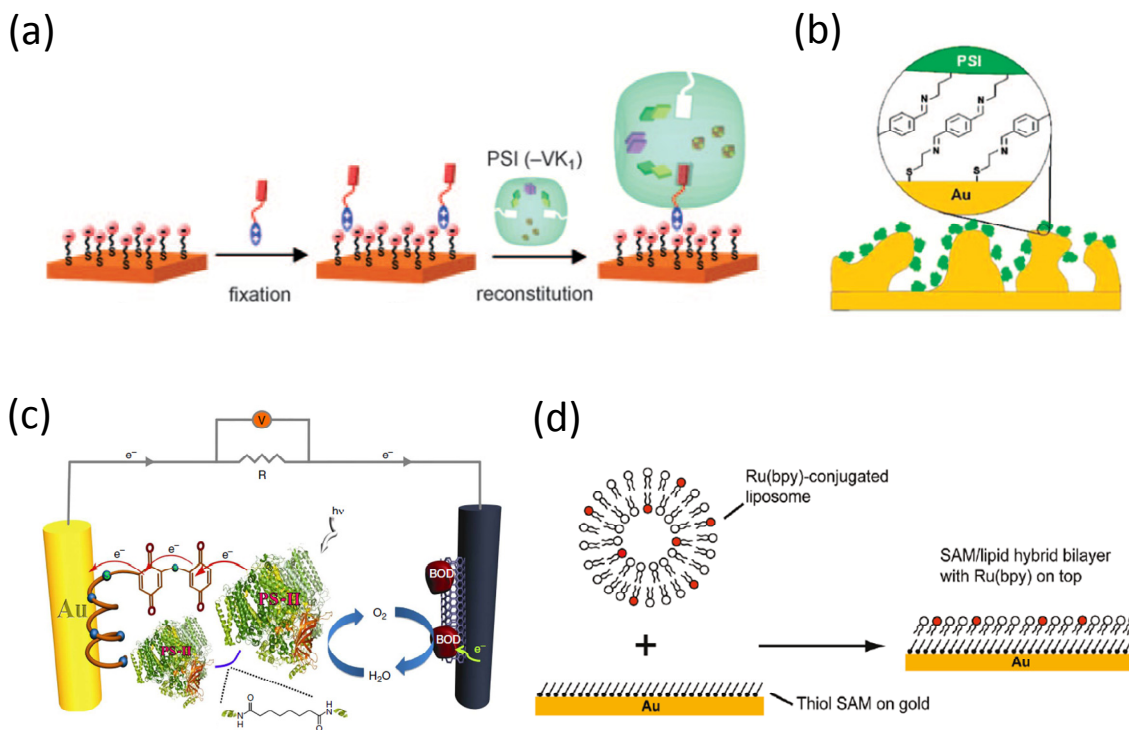


Figure 1.5. Examples of biomimetic light harvesting systems. (a) Assembly of photosystem I protein on a gold electrode with a molecular connector.⁷⁷ (b) Anchoring of photosystem I on a surface-treated nanoporous gold substrate. Higher surface area of the gold substrate results in more uptake of the bio-photosensitive molecules.⁷¹ (c) Schematic of the photochemical cell based on a photosystem II adsorbed gold electrode and a carbon nanotube counter electrode.⁷⁹ (d) Schematic of the formation of a Ru(bpy)₃²⁺-conjugated phospholipid/alkanethiol bilayer on a gold electrode.⁷²

Biologically derived or biocompatible materials were also used as a basis medium to construct new biomimetic photovoltaic systems. Zhan and co-workers have constructed a photocurrent generating system based on a bilayer structure of phospholipids, a major component of cell membranes (Figure 1.5(d)).^{72,80} Photoactive dyes and fullerenes have been immobilized within the lipid bilayer for photosensitization and efficient charge separation. Water-based electrolytes have been examined to fabricate biocompatible photovoltaic cells with reasonable photo-conversion efficiency.⁸¹⁻⁸³ Lai *et al.* demonstrated natural dye-based

DSSCs with a biocompatible aqueous electrolyte.⁸³ A gold nanoparticle layer on the photoanode surface could form a Schottky barrier to solve the problem of efficiency deterioration by the water electrolyte.

The structure and photosynthesis process have been adopted to propose a new concept for artificial leaf. Zhou *et al.* reported an inorganic artificial leaf composed of N-doped TiO₂ with a hierarchical structure derived from a natural leaf, which was used for efficient photochemical hydrogen production.⁸⁴ Park and coworkers presented a light-harvesting porphyrin-containing molecule⁸⁵ and peptide nanotube⁸⁶ to mimic the photochemical regeneration of nicotinamide cofactors by chlorophylls in photosynthesis. The cofactor regeneration and photoenzymatic synthesis of photosynthesis were also realized in a microfluidic platform.⁸⁷ Ham *et al.* demonstrated a biomimetic self-repair process in a light harvesting system based on photo-electrochemical complexes of photosynthetic reaction centers, phospholipids and carbon nanotubes.⁸⁸ The assembly, for the photoelectrochemical operation, and disassembly, for the replacement of damaged components, of the complexes were controlled by addition and removal of a surfactant.

1.3.5. Hydrogel Based Electronics and Photovoltaics

Hydrogels are soft, inexpensive, moldable and biocompatible. Despite their potential advantages as a medium, hydrogels have not been used much in electronic or photovoltaic devices because of their high water content. However, “ionics”, electronic devices operated by ionic currents, can be constructed on the basis of the hydrogel media. Recently, a few ionics based on hydrogel have been reported. Cayre *et al.* presented observation of nonlinear current response at the interface of two polyelectrolyte hydrogel layers (Figure 1.6(a)).⁶² The oppositely charged polyelectrolytes were embedded in the hydrogel layers, where the mobile counter ions formed a rectifying junction analogous to electron and hole carriers in an inorganic p-n junction diode. A quasi-liquid resistive-switching memory device and circuit composed of hydrogel and liquid metal have also been demonstrated (Figure 1.6(b)).⁸⁹ Asymmetric pH environments provided by two polyelectrolyte gel layers caused different

formation rates of the oxide skin on two liquid metal electrodes. The oxide skin was electrically insulating, which determined the resistance of the whole device.

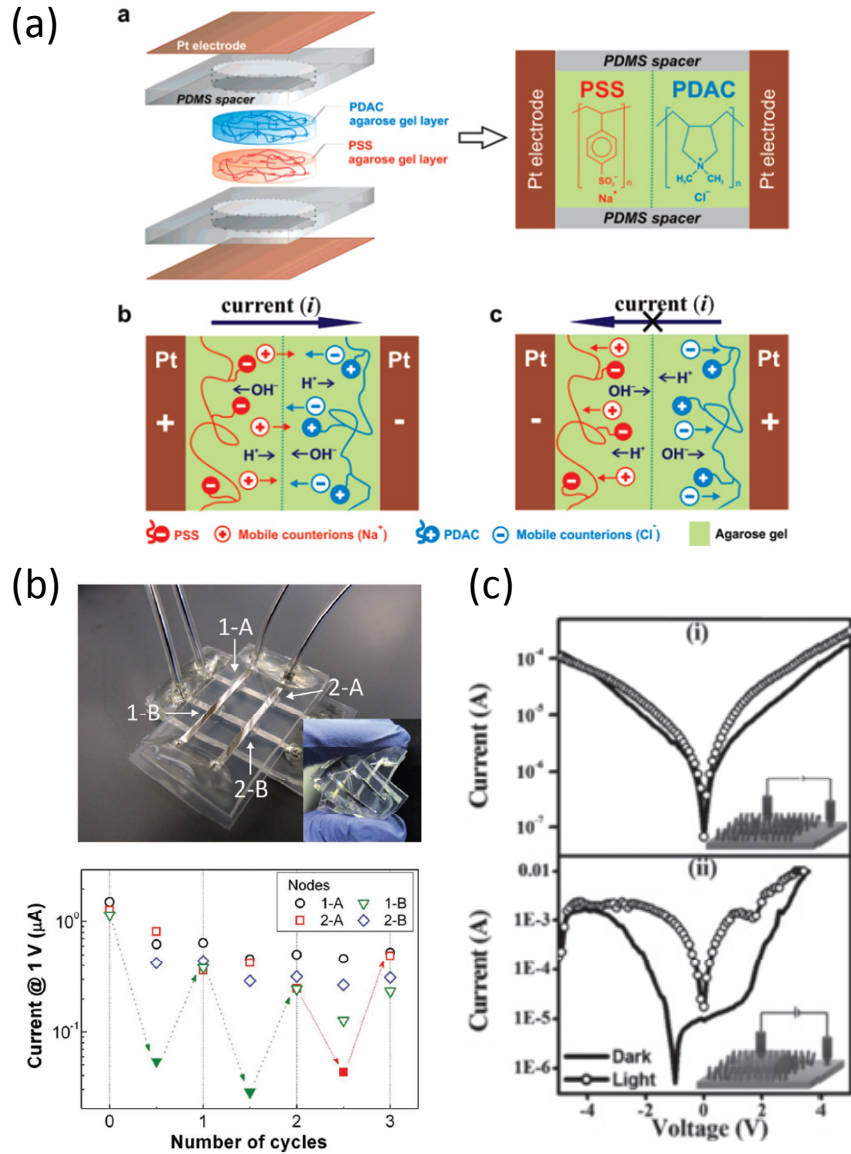


Figure 1.6. Hydrogel based electronics and photoresponsive systems. (a) Structure and operating mechanism of a polyelectrolyte gel based diode.⁶² (b) Photograph of an entirely soft memristor circuit and resistive-switching performance of individual nodes.⁸⁹ (c) Current-voltage curves under dark and illuminated conditions of ZnO nanorods/Pt and ZnO nanorods/agarose gel/Pt systems.⁹⁰

Little research has been done on hydrogel based photovoltaic systems. A couple of photoresponsive systems, where the hydrogel has been used as an ion conductor, have been reported. Polymer nanosheet photodiodes based on agarose hydrogel electrolytes have been studied, where the gel media has played a role of a quasi-solid electrolyte for reliable photocurrent generation of the dye-embedded polymer sheets.⁷³ Mandal *et al.* presented a light-harvesting photodetector with a ZnO-hydrogel interface (Figure 1.6(c)).⁹⁰ The agarose gel forms a solid contact with the ZnO nanostructure and increases ionic conductivity, thereby significantly improving the photoresponse time and magnitude.

1.4. A New Class of Microfluidic Systems Based on Aqueous Soft Matter

1.4.1. Unconventional Applications of Microfluidic Systems

Due to the advantages of microfluidic systems, such as small sample volume and device size, low production cost, high sensitivity and rapid analysis time, many of their applications lie in the field of biological research, e.g. biological assay, protein and cell separation and analysis and drug delivery.⁹¹⁻⁹⁶ In addition to such biological applications, the microfluidic systems could also find other useful applications. The microvascular network enables uniform supply of a fluid throughout a channel embedded medium. Wu *et al.* investigated efficient fluid transport in biomimetic bifurcating channel structures, which can be adapted for active cooling and tissue engineering.⁹⁷ It has been found that the maximum efficiency could be achieved when the sums of the radii of the parent and child channels are same. Hansen *et al.* reported catalytic polymerization accelerated by rapid heating with a temperature-controlled fluid, which was circulated in the embedded microfluidic networks (Figure 1.7(a)).⁹⁸ Due to the facile control of fluids at the microscale, microfluidic systems were used a novel platform for synthesis of monodisperse particles of polymers^{99,100} and hydrogels¹⁰¹ by *in situ* photopolymerization. Janus hydrogel particles have also been synthesized by using the coflowing laminar fluid streams in a sheath-flow microfluidic device (Figure 1.7(b)).¹⁰² Dendukuri *et al.*¹⁰³ and Shepherd *et al.*¹⁰⁴ demonstrated the formation of the particles with more complex shapes by using stop-flow lithography in a microfluidic device. Chung *et al.*

showed railed microfluidic devices where a groove was formed on the top channel surface to guide and assemble *in situ* polymerized microstructures.¹⁰⁵

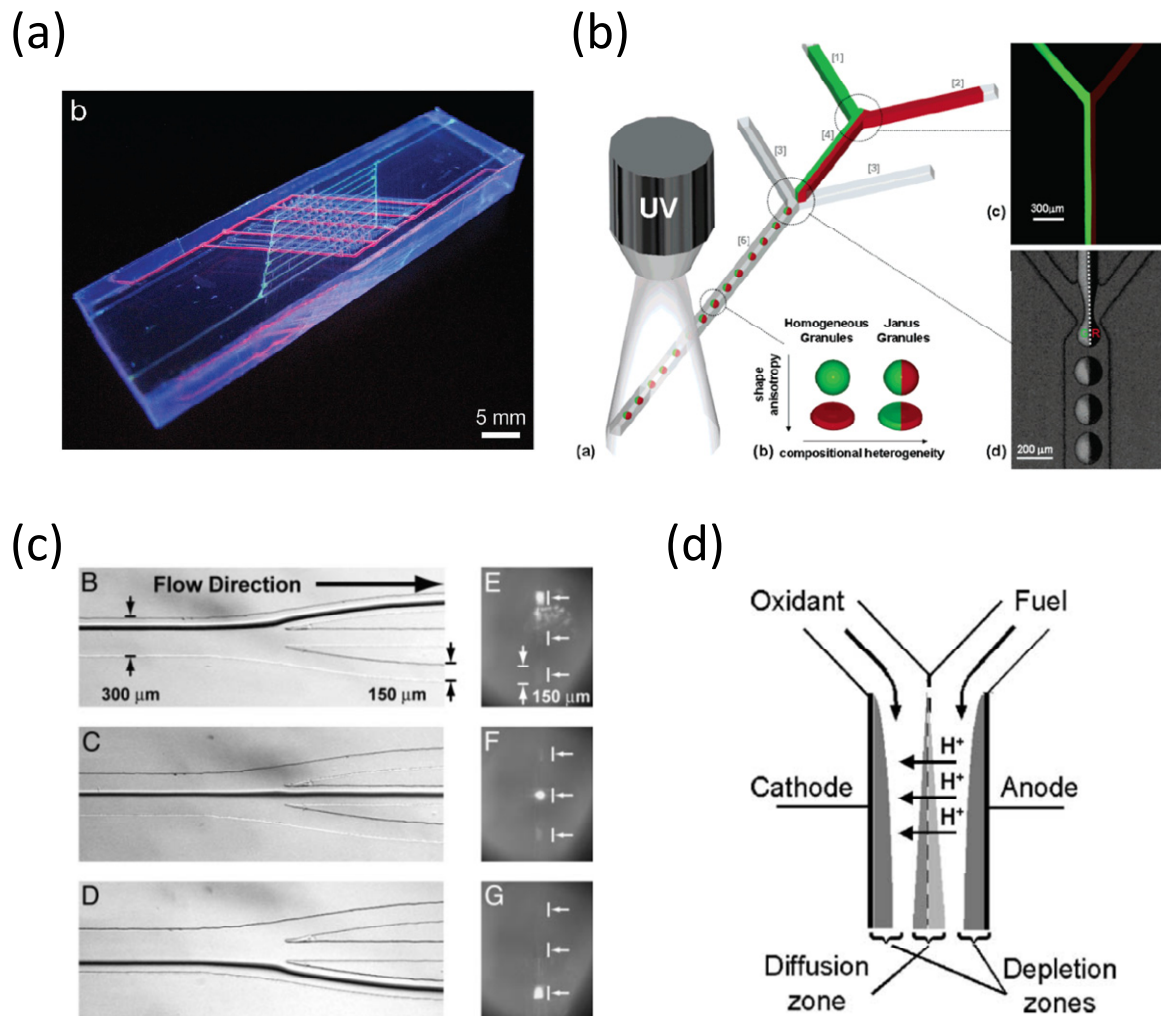


Figure 1.7. Examples of unconventional applications of microfluidic systems. (a) Self-healing epoxy substrate with embedded three microvascular networks.⁹⁸ Thermal control by fluid flowing through the third network (green) could accelerate the polymerization of epoxy resin (blue) and hardener (red) in a crack plane. (b) A sheath-flow microfluidic device for synthesis of homogeneous and Janus hydrogel granules.¹⁰² (c) Control of liquid-core flow by varying the relative flow rates of the liquid cladding in the microfluidic optical waveguide.¹⁰⁶ Right optical micrograph shows light exiting the waveguide at the end of the channels. (d) Schematic of a membraneless microfluidic fuel cell.¹⁰⁷

The multiple streams flowing at low Reynolds number in the microfluidic channels create smooth interfaces where the position of the interface can be easily controlled by changing the flow rate. Such characteristics of microfluidics have been used for many applications ranging from microfabrication to energy harvesting systems. Wolfe *et al.* presented waveguides and optical switching by using multiple streams with different refractive indices (Figure 1.7(c)).¹⁰⁶ Kenis *et al.* fabricated metal, organic and inorganic microwires at the smooth interface between the laminar flows of source solutions in the microfluidic channels.¹⁰⁸ Membraneless fuel cells were proposed and developed,^{107,109,110} where two laminar streams in anodic and cathodic compartments are intrinsically separated without convective mixing (Figure 1.7(d)).¹⁰⁷

1.4.2. Functional Microvascular Materials Based on Soft Matter

Soft materials with embedded microvascular network can be a flexible and reconfigurable template for constructing 2-D or 3-D architectures of fluidic substance. Depending on the physical, chemical and electrical properties of the filling substance in the channels, the resulting microvascular materials can achieve a wide variety of functionalities. Chang *et al.* reported a shape-memory elastomer with microvascular networks (Figure 1.8(a)).¹¹¹ The liquid photocurable polymer in the channels was solidified by UV, thereby retaining the various user-defined shapes. Siegel *et al.* reported a technique called microsolidics by injecting liquid solder into microfluidic channels and solidifying by cooling (Figure 1.8(b)).¹¹² The technique has offered a facile way to construct a complex metallic structure. So *et al.*¹¹³ and Kubo *et al.*¹¹⁴ described a technique for fabricating a flexible and stretchable microfluidic antenna, where the channels were filled with a highly conductive liquid metal alloy (Figure 1.8(c)). A simple stretchable radio frequency electronic device was also demonstrated with a liquid alloy-filled microfluidic antenna.¹¹⁵ Majumder *et al.* proposed a clean and reusable adhesive layer with the embedded microfluidic channels (Figure 1.8(d)).¹¹⁶ The oil-filled microchannels caused viscous dissipation and compressive stress, thereby enhancing the adhesive force. Toohey *et al.* reported a 3-D microvascular network-embedded material with a self-healing function, inspired by capillary networks in the human

skin (Figure 1.8(e)).¹¹⁷ The microvascular channels rapidly and efficiently supplied a liquid healing agent, which enabled repetitive healing of the cracked surface of the materials.

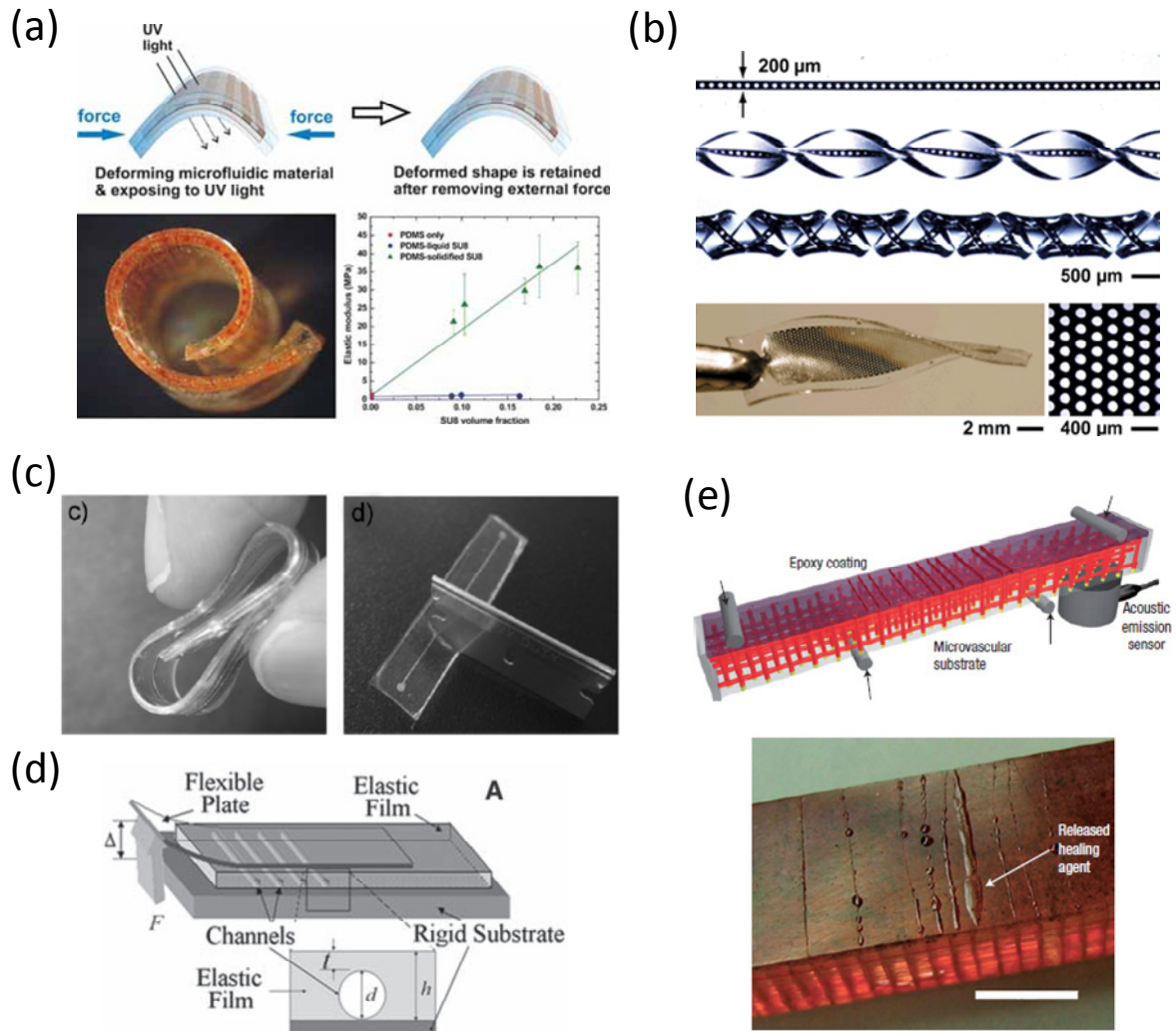


Figure 1.8. New functional microfluidic materials based on soft matter. (a) Soft materials of controlled shape and stiffness.¹¹¹ Microvascular networks filled with a photocurable polymer allow to retain a certain shape with UV illumination. (b) Three-dimensional metallic microstructures embedded in a microfluidic soft matrix.¹¹² Liquid solder was injected into the channels, followed by solidification by cooling. (c) Reversibly deformable and self-healing microfluidic antenna with liquid-metal alloy.¹¹³ (d) An elastomeric adhesive layer with embedded microfluidic channels.¹¹⁶ (e) Schematic and optical image of a self-healing microfluidic material filled with a polymerizable healing agent.¹¹⁷ The healed cracks are shown in the image.

1.4.3. Hydrogel Based Microfluidic Systems

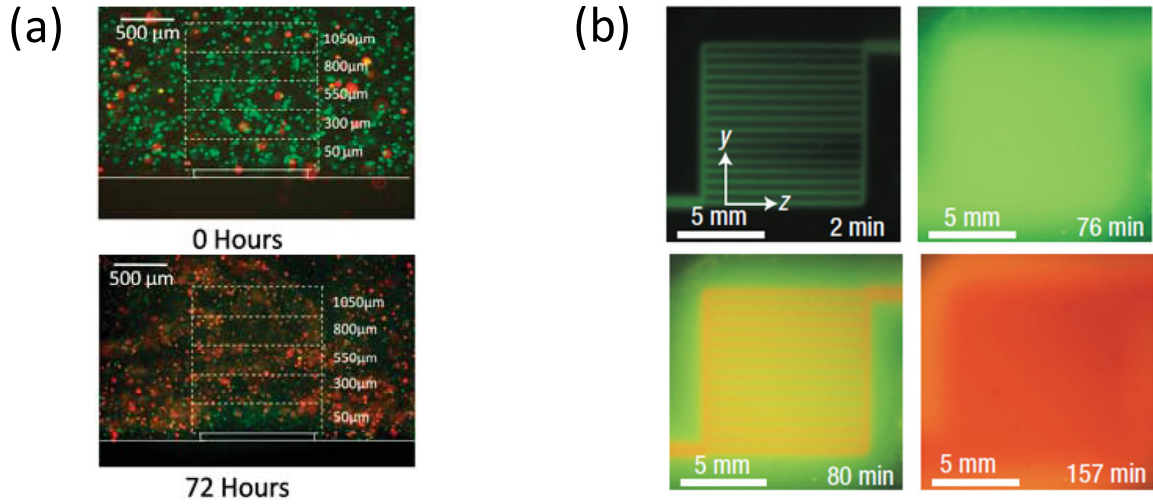


Figure 1.9. Hydrogel based microfluidic systems (a) Cross-sectional images of live (green)/dead (red) staining of cells embedded in agarose gel based channels. The cells near the channels remained viable after 3 days with supply of cell culture media.¹¹⁸ (b) Fluorescence images of an alginate gel scaffold with embedded microfluidic networks during sequential supply of fluorescein (green) and rhodamine B (red).¹¹⁹

Since naturally derived, physically crosslinked hydrogels, such as agarose gel, alginate gel and gelatin, are transformed from liquid phase to solid (sol-gel transformation) simply by controlling temperature or adding divalent ions or enzymes, the microfluidic channels can be easily formed in the hydrogel substrate by soft lithographic technique.¹¹⁸⁻¹²² Due to their biocompatibility, the hydrogel based microfluidic devices could find many potential applications, especially related to biological fields. Another characteristic feature of the hydrogel based microfluidic devices is associated with the porous structure of the gel matrix. As opposed to microfluidic devices made of conventional non-porous materials, highly porous gel-based microfluidic devices could utilize the diffusion of solutes through the channel walls. As a representative example, Ling *et al.* demonstrated a technique for fabrication of microfluidic devices based on cell-laden agarose gel (Figure 1.9(a)).¹¹⁸ The cells embedded in the microfluidic gel matrix remained viable when cell culture media were injected through the channels, followed by reaching the cells by diffusion through the gel.

Cheng *et al.* demonstrated a steady linear chemical concentration gradient generated between chemical source and sink channels formed in a hydrogel matrix.¹²⁰ The chemical gradient was used for the studies of cell chemotaxis. Stroock and coworkers reported microfluidic scaffolds based on the alginate hydrogel for tissue engineering (Figure 1.9(b)).^{119,121} The convective and diffusive transport mechanisms in the microfluidic hydrogel matrices with various channel structures have been investigated as means to control the distribution and supply of solutes in a bio-scaffold.

1.5. Layout of this Dissertation

The main objective of my graduate research is the development of electronic, photovoltaic and microfluidic devices based on a naturally derived hydrogel and bio-inspired structures. An agarose based hydrogel, which is soft, moldable, biocompatible and highly ion-conductive, is used as a novel medium for the devices with the various functionalities. Chapter 2 introduces an ionic current diode with the SiO₂ nanofilm/agarose gel interface (SNAGI diode). Its mechanism of the ionic current rectification based on electrostatic gating of SiO₂ film is discussed. Extremely high rectification performance is achieved by increasing ionic conductivity with addition of polyelectrolyte and salt to the gel matrix. Chapter 3 describes another ionic current diode composed entirely of soft matter by combining hydrogel media and liquid metal electrodes. Two polyelectrolyte embedded hydrogel layers provide different pH environments to the liquid metal surface, which affect the insulating oxide skin formation at the interface of hydrogel and liquid metal. How the asymmetric configuration of two polyelectrolyte gel layers interfacing liquid metal electrodes enables ionic current rectification is discussed. Chapter 4 presents hydrogel based photovoltaic devices (HGPVs). The hydrogel layers infused with two photosensitive dye ions exhibit photocurrent response. A provisional operational mechanism of HGPVs is suggested based on the dependence of the photocurrent on the dye location in the gel and synergistic effect of the two dye ions. A flexible and low cost HGPV device is constructed by using a conducting plastic substrate and a carbon-coated copper counter electrode. A successful operation of biologically derived photosensitive reagents in HGPVs is demonstrated.

Chapter 5 demonstrates a light driven microfluidic reactor based on a hydrogel. The porous hydrogel matrix with the embedded microfluidic channels provides hierarchical pathways to injected solutes. The convective and diffusive transport mechanism in the microfluidic hydrogel reactor enables the reactant solutes to be uniformly supplied and efficiently reach to the surface of the photo-catalysts, which are three dimensionally distributed in the gel matrix. Chapter 6 discusses the computational study on the transport of solutes in the microfluidic channel embedded hydrogel media. The simulation results using COMSOL predict a time dependent-concentration profile of the injected solutes, thereby enabling the optimization of the channel design. The validity of the simulation procedure is proven by experimental results. In Chapter 7, a new biomimetic photovoltaic concept is presented, inspired by the venation network and regeneration functionality of a natural leaf. The microfluidic channel-embedded hydrogel media uniformly deliver the reagents for the photovoltaic operation. Efficient replacement of the degraded photosensitive molecules is demonstrated by the established regeneration process. Chapter 8 summarizes my graduate research and gives the future outlook for extending this work.

1.6. References

1. Peppas, N. A., Hilt, J. Z., Khademhosseini, A. & Langer, R. Hydrogels in biology and medicine: From molecular principles to bionanotechnology. *Adv. Mater.* **18**, 1345-1360 (2006).
2. Han, I. S. *et al.* Constant-volume hydrogel osmometer: A new device concept for miniature biosensors. *Biomacromolecules* **3**, 1271-1275 (2002).
3. Hendrickson, G. R. & Andrew Lyon, L. Bioresponsive hydrogels for sensing applications. *Soft Matter* **5**, 29-35 (2009).
4. Allcock, H. R., Phelps, M. V. B., Barrett, E. W., Pishko, M. V. & Koh, W.-G. Ultraviolet photolithographic development of polyphosphazene hydrogel microstructures for potential use in microarray biosensors. *Chem. Mater.* **18**, 609-613 (2006).
5. Zhou, J. *et al.* Viscoelastic behavior and in vivo release study of microgel dispersions with inverse thermoreversible gelation. *Biomacromolecules* **9**, 142-148 (2007).

6. Gutiérrez, M. C. *et al.* Hydrogel scaffolds with immobilized bacteria for 3D cultures. *Chem. Mater.* **19**, 1968-1973 (2007).
7. Song, J., Saiz, E. & Bertozzi, C. R. A New approach to mineralization of biocompatible hydrogel scaffolds: An efficient process toward 3-dimensional bonelike composites. *J. Am. Chem. Soc.* **125**, 1236-1243 (2003).
8. Drury, J. L. & Mooney, D. J. Hydrogels for tissue engineering: scaffold design variables and applications. *Biomaterials* **24**, 4337-4351 (2003).
9. Yan, H., Saiani, A., Gough, J. E. & Miller, A. F. Thermoreversible protein hydrogel as cell scaffold. *Biomacromolecules* **7**, 2776-2782 (2006).
10. Nguyen, K. T. & West, J. L. Photopolymerizable hydrogels for tissue engineering applications. *Biomaterials* **23**, 4307-4314 (2002).
11. Malmsten, M. Soft drug delivery systems. *Soft Matter* **2**, 760-769 (2006).
12. Jo, Y. S., Gantz, J., Hubbell, J. A. & Lutolf, M. P. Tailoring hydrogel degradation and drug release via neighboring amino acid controlled ester hydrolysis. *Soft Matter* **5**, 440-446 (2009).
13. Cavalieri, F. *et al.* Novel PVA-based hydrogel microparticles for doxorubicin delivery. *Biomacromolecules* **9**, 1967-1973 (2008).
14. Missirlis, D., Tirelli, N. & Hubbell, J. A. Amphiphilic hydrogel nanoparticles. preparation, characterization, and preliminary assessment as new colloidal drug carriers. *Langmuir* **21**, 2605-2613 (2005).
15. Li, Y., Rodrigues, J. & Tomas, H. Injectable and biodegradable hydrogels: gelation, biodegradation and biomedical applications. *Chem. Soc. Rev.* **41**, 2193-2221 (2012).
16. Uludag, H., De Vos, P. & Tresco, P. A. Technology of mammalian cell encapsulation. *Adv. Drug Delivery Rev.* **42**, 29-64 (2000).
17. Arai, F. *et al.* On chip single-cell separation and immobilization using optical tweezers and thermosensitive hydrogel. *Lab Chip* **5**, 1399-1403 (2005).
18. Serwer, P. Agarose gels: Properties and use for electrophoresis. *Electrophoresis* **4**, 375-382 (1983).
19. Ueno, H. & Kaneko, M. Investigation of a nanostructured polysaccharide solid medium for electrochemistry. *J. Electroanal. Chem.* **568**, 87-92 (2004).

20. Rahfoth, B. *et al.* Transplantation of allograft chondrocytes embedded in agarose gel into cartilage defects of rabbits. *Osteoarthr. Cartilage* **6**, 50-65 (1998).
21. Johnson, E. M., Berk, D. A., Jain, R. K. & Deen, W. M. Diffusion and partitioning of proteins in charged agarose gels. *Biophys. J.* **68**, 1561-1568 (1995).
22. Fatin-Rouge, N., Milon, A., Buffle, J., Goulet, R. R. & Tessier, A. Diffusion and partitioning of solutes in agarose hydrogels: The relative influence of electrostatic and specific interactions. *J. Phys. Chem. B* **107**, 12126-12137 (2003).
23. Johnson, E. M. & Deen, W. M. Hydraulic permeability of agarose gels. *AIChE J.* **42**, 1220-1224 (1996).
24. Waki, S., Harvey, J. D. & Bellamy, A. R. Study of agarose gels by electron microscopy of freeze-fractured surfaces. *Biopolymers* **21**, 1909-1926 (1982).
25. Pernodet, N., Maaloum, M. & Tinland, B. Pore size of agarose gels by atomic force microscopy. *Electrophoresis* **18**, 55-58 (1997).
26. Jokerst, J. V. *et al.* Location of biomarkers and reagents within agarose beads of a programmable bio-nano-chip. *Small* **7**, 613-624 (2011).
27. Metzger, R. M. Electrical rectification by a molecule: The advent of unimolecular electronic devices. *Acc. Chem. Res.* **32**, 950-957 (1999).
28. Lee, Y., Carsten, B. & Yu, L. Understanding the anchoring group effect of molecular diodes on rectification. *Langmuir* **25**, 1495-1499 (2008).
29. Jiang, P., Morales, G. M., You, W. & Yu, L. Synthesis of diode molecules and their sequential assembly to control electron transport. *Angew. Chem. Int. Ed.* **43**, 4471-4475 (2004).
30. Liao, L. *et al.* Multiwall boron carbonitride/carbon nanotube junction and its rectification behavior. *J. Am. Chem. Soc.* **129**, 9562-9563 (2007).
31. Wei, Z., Kondratenko, M., Dao, L. H. & Perepichka, D. F. Rectifying diodes from asymmetrically functionalized single-wall carbon nanotubes. *J. Am. Chem. Soc.* **128**, 3134-3135 (2006).
32. Jiao, L. *et al.* Fabrication of Carbon Nanotube Diode with Atomic Force Microscopy Manipulation. *J. Phys. Chem. C* **112**, 7544-7546 (2008).
33. Mohanta, K. & Pal, A. J. Rectifying junctions from an assembly of two dissimilar nanoparticles. *J. Phys. Chem. C* **112**, 3232-3238 (2008).

34. Mohanta, K., Batabyal, S. K. & Pal, A. J. pn-Junction rectifiers based on p-ZnO and n-ZnO nanoparticles. *Chem. Mater.* **19**, 3662-3666 (2007).
35. Leger, J. M., Rodovsky, D. B. & Bartholomew, G. P. Self-assembled, chemically fixed homojunctions in semiconducting polymers. *Adv. Mater.* **18**, 3130-3134 (2006).
36. Cheng, C. H. W. & Lonergan, M. C. A Conjugated polymer pn junction. *J. Am. Chem. Soc.* **126**, 10536-10537 (2004).
37. Cheng, C. H. W., Boettcher, S. W., Johnston, D. H. & Lonergan, M. C. Unidirectional current in a polyacetylene hetero-ionic junction. *J. Am. Chem. Soc.* **126**, 8666-8667 (2004).
38. Siwy, Z., Heins, E., Harrell, C. C., Kohli, P. & Martin, C. R. Conical-nanotube ion-current rectifiers: The role of surface charge. *J. Am. Chem. Soc.* **126**, 10850-10851 (2004).
39. Israelachvili, J. N. *Intermolecular & surface forces*. 2 ed., Academic Press, San Diego, 1992.
40. Vlasiouk, I., Smirnov, S. & Siwy, Z. Ionic selectivity of single nanochannels. *Nano Lett.* **8**, 1978-1985 (2008).
41. Zhang, Y. *et al.* Electric field control and analyte transport in Si/SiO₂ fluidic nanochannels. *Lab Chip* **8**, 1671-1675 (2008).
42. Fan, R., Huh, S., Yan, R., Arnold, J. & Yang, P. D. Gated proton transport in aligned mesoporous silica films. *Nat. Mater.* **7**, 303-307 (2008).
43. Daiguji, H., Oka, Y. & Shirono, K. Nanofluidic diode and bipolar transistor. *Nano Lett.* **5**, 2274-2280 (2005).
44. Harrell, C. C., Kohli, P., Siwy, Z. & Martin, C. R. DNA-nanotube artificial ion channels. *J. Am. Chem. Soc.* **126**, 15646-15647 (2004).
45. Wei, C., Bard, A. J. & Feldberg, S. W. Current rectification at quartz nanopipet electrodes. *Anal. Chem.* **69**, 4627-4633 (1997).
46. Hegedüs, L. *et al.* Nonlinear effects of electrolyte diodes and transistors in a polymer gel medium. *Chaos* **9**, 283-297 (1999).
47. Karnik, R., Duan, C., Castelino, K., Daiguji, H. & Majumdar, A. Rectification of ionic current in a nanofluidic diode. *Nano Lett.* **7**, 547-551 (2007).

48. Gracheva, M. E., Vidal, J. & Leburton, J.-P. p-n Semiconductor membrane for electrically tunable ion current rectification and filtering. *Nano Lett.* **7**, 1717-1722 (2007).
49. Siwy, Z. S. Ion-current rectification in nanopores and nanotubes with broken symmetry. *Adv. Funct. Mater.* **16**, 735-746 (2006).
50. Davenport, M., Rodriguez, A., Shea, K. J. & Siwy, Z. S. Squeezing ionic liquids through nanopores. *Nano Lett.* **9**, 2125-2128 (2009).
51. Ali, M., Ramirez, P., Mafel, S., Neumann, R. & Ensinger, W. A pH-tunable nanofluidic diode with a broad range of rectifying properties. *ACS Nano* **3**, 603-608 (2009).
52. Umehara, S. *et al.* Current rectification with poly-l-lysine-coated quartz nanopipettes. *Nano Lett.* **6**, 2486-2492 (2006).
53. Lovrecek, B., Despic, A. & Bockris, J. O. M. Electrolytic junctions with rectifying properties. *J. Phys. Chem.* **63**, 750-751 (1959).
54. Lindner, J., Snita, D. & Marek, M. Modelling of ionic systems with a narrow acid-base boundary. *Phys. Chem. Chem. Phys.* **4**, 1348-1354 (2002).
55. Ivan, K., Wittmann, M., Simon, P. L., Noszticzius, Z. & Vollmer, J. Electrolyte diodes and hydrogels: Determination of concentration and pK value of fixed acidic groups in a weakly charged hydrogel. *Phys. Rev. E* **70**, 061402 (2004).
56. Hegedüs, L., Wittmann, M., Kirschner, N. & Noszticzius, Z. Reaction, diffusion, electric conduction and determination of fixed ions in a hydrogel. *Prog. Colloid Polm. Sci.* **102**, 101-109 (1996).
57. Han, J.-H., Kim, K. B., Kim, H. C. & Chung, T. D. Ionic circuits based on polyelectrolyte diodes on a microchip. *Angew. Chem. Int. Ed.* **48**, 3830-3833 (2009).
58. Yan, R., Liang, W., Fan, R. & Yang, P. Nanofluidic diodes based on nanotube heterojunctions. *Nano Lett.* **9**, 3820-3825 (2009).
59. Jung, J.-Y., Joshi, P., Petrossian, L., Thornton, T. J. & Posner, J. D. Electromigration current rectification in a cylindrical nanopore due to asymmetric concentration polarization. *Anal. Chem.* **81**, 3128-3133 (2009).
60. Yameen, B. *et al.* Single conical nanopores displaying pH-tunable rectifying characteristics. Manipulating ionic transport with zwitterionic polymer brushes. *J. Am. Chem. Soc.* **131**, 2070-2071 (2009).

61. Cheng, L.-J. & Guo, L. J. Ionic current rectification, breakdown, and switching in heterogeneous oxide nanofluidic devices. *ACS Nano* **3**, 575-584 (2009).
62. Cayre, O. J., Chang, S. T. & Velev, O. D. Polyelectrolyte diode: Nonlinear current response of a junction between aqueous ionic gels. *J. Am. Chem. Soc.* **129**, 10801-10806 (2007).
63. Vlasiouk, I. & Siwy, Z. S. Nanofluidic diode. *Nano Lett.* **7**, 552-556 (2007).
64. Shao, Y., Bazan, G. C. & Heeger, A. J. Long-lifetime polymer light-emitting electrochemical cells. *Adv. Mater.* **19**, 365-370 (2007).
65. Ashwell, G. J., Urasinska, B. & Tyrrell, W. D. Molecules that mimic Schottky diodes. *Phys. Chem. Chem. Phys.* **8**, 3314-3319 (2006).
66. Lenfant, S., Krzeminski, C., Delerue, C., Allan, G. & Vuillaume, D. Molecular rectifying diodes from self-assembly on silicon. *Nano Lett.* **3**, 741-746 (2003).
67. Chen, M., Nilsson, D., Kugler, T., Berggren, M. & Remonen, T. Electric current rectification by an all-organic electrochemical device. *Appl. Phys. Lett.* **81**, 2011-2013 (2002).
68. Chabinyk, M. L. *et al.* Molecular rectification in a metal-insulator-metal junction based on self-assembled monolayers. *J. Am. Chem. Soc.* **124**, 11730-11736 (2002).
69. Baldwin, J. W. *et al.* Rectification and nonlinear optical properties of a Langmuir-Blodgett monolayer of a pyridinium dye. *J. Phys. Chem. B* **106**, 12158-12164 (2002).
70. Chapin, D. M., Fuller, C. S. & Pearson, G. L. A new silicon p-n junction photocell for converting solar radiation into electrical power. *J. Appl. Phys.* **25**, 676-677 (1954).
71. Ciesielski, P. N. *et al.* Functionalized nanoporous gold leaf electrode films for the immobilization of photosystem I. *ACS Nano* **2**, 2465-2472 (2008).
72. Jiang, K., Xie, H. & Zhan, W. Photocurrent generation from Ru(bpy)₃²⁺ immobilized on phospholipid/alkanethiol hybrid bilayers. *Langmuir* **25**, 11129-11136 (2009).
73. Matsui, J., Abe, K., Mitsuishi, M., Aoki, A. & Miyashita, T. Quasi-solid-state optical logic devices based on redox polymer nanosheet assembly. *Langmuir* **25**, 11061-11066 (2009).
74. Bhardwaj, R., Pan, R. L. & Gross, E. L. Solar energy conversion by chloroplast photoelectrochemical cells. *Nature* **289**, 396-398 (1981).

75. Meunier, C. F., Van Cutsem, P., Kwon, Y.-U. & Su, B.-L. Thylakoids entrapped within porous silica gel: towards living matter able to convert energy. *J. Mater. Chem.* **19**, 1535-1542 (2009).
76. Terasaki, N. *et al.* Fabrication of novel photosystem I-gold nanoparticle hybrids and their photocurrent enhancement. *Thin Solid Films* **499**, 153-156 (2006).
77. Terasaki, N. *et al.* Plugging a molecular wire into photosystem I: Reconstitution of the photoelectric conversion system on a gold electrode. *Angew. Chem. Int. Ed.* **48**, 1585-1587 (2009).
78. Ciesielski, P. N. *et al.* Enhanced photocurrent production by photosystem I multilayer assemblies. *Adv. Funct. Mater.* **20**, 4048-4054 (2010).
79. Yehezkeli, O. *et al.* Integrated photosystem II-based photo-bioelectrochemical cells. *Nat. Commun.* **3**, 742 (2012).
80. Zhan, W. & Jiang, K. A Modular photocurrent generation system based on phospholipid-assembled fullerenes. *Langmuir* **24**, 13258-13261 (2008).
81. Murakami, T. N., Saito, H., Uegusa, S., Kawashima, N. & Miyasaka, T. Water-based dye-sensitized solar cells: Interfacial activation of TiO₂ mesopores in contact with aqueous electrolyte for efficiency development. *Chem. Lett.* **32**, 1154-1155 (2003).
82. Law, C. *et al.* Water-based electrolytes for dye-sensitized solar cells. *Adv. Mater.* **22**, 4505-4509 (2010).
83. Lai, W. H., Su, Y. H., Teoh, L. G. & Hon, M. H. Commercial and natural dyes as photosensitizers for a water-based dye-sensitized solar cell loaded with gold nanoparticles. *J. Photochem. Photobiol., A* **195**, 307-313 (2008).
84. Zhou, H. *et al.* Artificial inorganic leafs for efficient photochemical hydrogen production inspired by natural photosynthesis. *Adv. Mater.* **22**, 951-956 (2010).
85. Kim, J. H., Lee, S. H., Lee, J. S., Lee, M. & Park, C. B. Zn-containing porphyrin as a biomimetic light-harvesting molecule for biocatalyzed artificial photosynthesis. *Chem. Commun.* **47**, 10227-10229 (2011).
86. Kim, J. H., Lee, M., Lee, J. S. & Park, C. B. Self-assembled light-harvesting peptide nanotubes for mimicking natural photosynthesis. *Angew. Chem. Int. Ed.* **51**, 517-520 (2012).
87. Lee, J. S., Lee, S. H., Kim, J. H. & Park, C. B. Artificial photosynthesis on a chip: microfluidic cofactor regeneration and photoenzymatic synthesis under visible light. *Lab Chip* **11**, 2309-2311 (2011).

88. Ham, M.-H. *et al.* Photoelectrochemical complexes for solar energy conversion that chemically and autonomously regenerate. *Nat. Chem.* **2**, 929-936 (2010).
89. Koo, H.-J., So, J.-H., Dickey, M. D. & Velev, O. D. Towards all-soft matter circuits: Prototypes of quasi-liquid devices with memristor characteristics. *Adv. Mater.* **23**, 3559-3564 (2011).
90. Mandal, L. *et al.* A Quasi-liquid iontronic–electronic light-harvesting hybrid photodetector with giant response. *Adv. Mater.*, In press.
91. Gomez, F. A. *Biological Applications of Microfluidics*, Wiley. John Wiley & Sons, Inc., Hoboken, NJ, 2008.
92. Stone, H. A., Stroock, A. D. & Ajdari, A. Engineering flows in small devices. *Annu. Rev. Fluid Mech.* **36**, 381-411 (2004).
93. Yager, P. *et al.* Microfluidic diagnostic technologies for global public health. *Nature* **442**, 412-418 (2006).
94. Tudos, A. J., Besselink, G. A. J. & Schasfoort, R. B. M. Trends in miniaturized total analysis systems for point-of-care testing in clinical chemistry. *Lab Chip* **1**, 83-95 (2001).
95. Delamarche, E., Juncker, D. & Schmid, H. Microfluidics for processing surfaces and miniaturizing biological assays. *Adv. Mater.* **17**, 2911-2933 (2005).
96. Khandurina, J. & Guttman, A. s. Bioanalysis in microfluidic devices. *J. Chromatogr. A* **943**, 159-183 (2002).
97. Wu, W. *et al.* Direct-write assembly of biomimetic microvascular networks for efficient fluid transport. *Soft Matter* **6**, 739-742 (2010).
98. Hansen, C. J., White, S. R., Sottos, N. R. & Lewis, J. A. Accelerated self-healing via ternary interpenetrating microvascular networks. *Adv. Funct. Mater.* **21**, 4320-4326 (2011).
99. Xu, S. *et al.* Generation of monodisperse particles by using microfluidics: Control over size, shape, and composition. *Angew. Chem. Int. Ed.* **44**, 724-728 (2005).
100. Dendukuri, D., Pregibon, D. C., Collins, J., Hatton, T. A. & Doyle, P. S. Continuous-flow lithography for high-throughput microparticle synthesis. *Nat. Mater.* **5**, 365-369 (2006).

101. Jeong, W. J. *et al.* Continuous fabrication of biocatalyst immobilized microparticles using photopolymerization and immiscible liquids in microfluidic systems. *Langmuir* **21**, 3738-3741 (2005).
102. Shepherd, R. F. *et al.* Microfluidic assembly of homogeneous and janus colloid-filled hydrogel granules. *Langmuir* **22**, 8618-8622 (2006).
103. Dendukuri, D., Gu, S. S., Pregibon, D. C., Hatton, T. A. & Doyle, P. S. Stop-flow lithography in a microfluidic device. *Lab Chip* **7**, 818-828 (2007).
104. Shepherd, R. F. *et al.* Stop-Flow lithography of colloidal, glass, and silicon microcomponents. *Adv. Mater.* **20**, 4734-4739 (2008).
105. Chung, S. E., Park, W., Shin, S., Lee, S. A. & Kwon, S. Guided and fluidic self-assembly of microstructures using railed microfluidic channels. *Nat. Mater.* **7**, 581-587 (2008).
106. Wolfe, D. B. *et al.* Dynamic control of liquid-core/liquid-cladding optical waveguides. *Proc. Natl. Acad. Sci. U.S.A.* **101**, 12434-12438 (2004).
107. Choban, E. R., Markoski, L. J., Wieckowski, A. & Kenis, P. J. A. Microfluidic fuel cell based on laminar flow. *J. Power Sources* **128**, 54-60 (2004).
108. Kenis, P. J. A., Ismagilov, R. F. & Whitesides, G. M. Microfabrication inside capillaries using multiphase laminar flow patterning. *Science* **285**, 83-85 (1999).
109. Ferrigno, R., Stroock, A. D., Clark, T. D., Mayer, M. & Whitesides, G. M. Membraneless vanadium redox fuel cell using laminar flow. *J. Am. Chem. Soc.* **124**, 12930-12931 (2002).
110. Kjeang, E., Michel, R., Harrington, D. A., Djilali, N. & Sinton, D. A microfluidic fuel cell with flow-through porous electrodes. *J. Am. Chem. Soc.* **130**, 4000-4006 (2008).
111. Chang, S. T. *et al.* Materials of controlled shape and stiffness with photocurable microfluidic endoskeleton. *Adv. Mater.* **21**, 2803-2807 (2009).
112. Siegel, A. C., Bruzewicz, D. A., Weibel, D. B. & Whitesides, G. M. Microsolidics: Fabrication of three-dimensional metallic microstructures in poly(dimethylsiloxane). *Adv. Mater.* **19**, 727-733 (2007).
113. So, J.-H. *et al.* Reversibly deformable and mechanically tunable fluidic antennas. *Adv. Funct. Mater.* **19**, 3632-3637 (2009).
114. Kubo, M. *et al.* Stretchable microfluidic radiofrequency antennas. *Adv. Mater.* **22**, 2749-2752 (2010).

115. Cheng, S. & Wu, Z. Microfluidic stretchable RF electronics. *Lab Chip* **10**, 3227-3234 (2010).
116. Majumder, A., Ghatak, A. & Sharma, A. microfluidic adhesion induced by subsurface microstructures. *Science* **318**, 258-261 (2007).
117. Toohey, K. S., Sottos, N. R., Lewis, J. A., Moore, J. S. & White, S. R. Self-healing materials with microvascular networks. *Nat. Mater.* **6**, 581-585 (2007).
118. Ling, Y. *et al.* A cell-laden microfluidic hydrogel. *Lab Chip* **7**, 756-762 (2007).
119. Choi, N. W. *et al.* Microfluidic scaffolds for tissue engineering. *Nat. Mater.* **6**, 908-915 (2007).
120. Cheng, S.-Y. *et al.* A hydrogel-based microfluidic device for the studies of directed cell migration. *Lab Chip* **7**, 763-769 (2007).
121. Cabodi, M. *et al.* A microfluidic biomaterial. *J. Am. Chem. Soc.* **127**, 13788-13789 (2005).
122. Paguirigan, A. & Beebe, D. J. Gelatin based microfluidic devices for cell culture. *Lab Chip* **6**, 407-413 (2006).

Chapter 2

Ion-Current Diode with Aqueous Gel/SiO₂ Nanofilm Interfaces*

* Partially based on Koo, Chang and Velev, *Small*, 2010, 6, 1393

2.1. Introduction

Nonlinear ion transport through nanoscale structures can be used in new types of microcircuits, inspired by biological processes such as adenosine triphosphate synthesis and neural transmission.¹⁻⁶ The nonlinear current resulting from preferential direction of ion flow can be used for signal transmission as well as signal processing, e.g., ionic current rectification and amplification as in electronic circuits. Electronic signal processing systems using ionic current conduction are capable of operation in aqueous phase, which makes them suitable for biomedical applications such as molecular delivery and sensing.⁷⁻¹⁰

Recent advances in nanofabrication have enabled control of selective ionic transport by designing various nanostructures of controlled surface charge, such as aligned nanochannels,¹¹⁻¹⁴ nanopipettes^{15, 16} and cone-shaped nanotubes.¹⁷⁻²¹ Ionic flows can be selectively gated by electrostatic field at the charged channel walls. Furthermore, asymmetric distribution of charges on two surfaces of the nanofluidic channel walls creates an ionic junction in the channels and engenders one-directional ionic flows. On a larger scale, the so-called “electrolyte diodes” provide an example of device-like structures operating on ionic conductance. Aqueous electrolyte junctions between acidic (e.g. HCl) and basic (e.g. KOH) solutions exhibit rectifying properties analogous to the junction of n- and p-type semiconductors.²²⁻²⁷ Our group reported earlier a practical ionic rectifier – hydrogel-based polyelectrolyte diode constructed by bringing in contact two gels doped with polyelectrolytes of opposite charges.²⁸ The junction formed at the interface between the gel layers rectifies the ionic current. This aqueous gel based device has good compatibility with biological materials.

Similar effect of nonlinear current response has also been observed at SiO₂/electrolyte interfaces.²⁹ Nonlinear conductivity of SiO₂ films, which enables current flows in a preferential direction, has been mentioned in the literature.^{30, 31} However, a simple SiO₂/electrolyte solution interface does not allow for easy making of encapsulated device with long-term stability. Here, we demonstrate an electrochemical diode based on a SiO₂ Nanofilm/Aqueous Gel Interface (“SNAGI” diode), where a SiO₂ layer provides selective conduction of the ionic current between the aqueous gel and the electrode. The aqueous gel not only effectively encapsulates the liquid but also improves the ionic conductance and

rectification ratio. The SNAGI diodes showed high current density and rectification ratio as high as 3.8×10^4 , which is two orders of magnitude higher than the ratio in the best nanofluidic channel devices.³² These devices could be biocompatible and the process of their preparation is simple and scalable.

2.2. Experimental Section

2.2.1. Materials

To prepare the hydrogel matrix, agarose (biochemistry research grade, Acros Organics) was added to pure Milli-Q water or NaCl solution under continuous stirring and the mixture was boiled on a hot plate. When the agarose was thoroughly dissolved, the mixture was cooled down to room temperature and gelled. The minimum concentration of the agarose was 0.5 wt. %, below which the gelation did not occur. For desalination, the polyelectrolyte embedded gels were soaked in distilled water for 43 hours. The water was replaced two or three times during the procedure. The SiO₂ layer was grown on a highly n-doped Si wafer (Silicon Valley Microelectronics, Inc., 0.008-0.02 Ω-cm, 525 +/- 25μm thick) by a standard thermal oxidation process (wet oxidation, ~800 °C). The resulting thicknesses were about 170 nm and 580 nm, which were measured by an ellipsometer (Auto EL^R, Rudolph Technologies, Inc.).

2.2.2. Device Fabrication

A poly(dimethylsiloxane) (PDMS) spacer with 450 μm thickness was punched to make a 5-mm diameter hole and placed on fluorine-doped tin oxide electrode (FTO, Pilkington). The PDMS chamber was filled with the hydrogel melted by microwave heating using a micro-pipette, and then covered with cover glass to prepare the same shape and size gel with the hole. The cover glass was removed when the hydrogel was cooled and the n-doped Si wafer electrode with SiO₂ layer was placed on the PDMS spacer to contact the hydrogel.

2.2.3. Measurement of Current Rectification

The current-voltage characteristics were measured by using a computer-controlled source meter (Keithley 2602, Keithley Instruments Inc.) at room temperature. The transient responses of SNAGI diode to AC bias were measured using a function generator, digital multimeter, and computer-controlled digital oscilloscope (22120A, 34405A, and DSO3202A, correspondingly, all products of Agilent Technologies). A ± 10 V AC square-wave signal with frequency ranging from 0.1 Hz to 1 kHz was applied to a SNAGI diode connected in a series with a 15 k Ω resistor. The voltage data were measured on the resistor load. This voltage is inversely proportional to the current through the diodes. A DC regulated power supply (Extech Instruments) and a digital multimeter were used to investigate the long term device stability under continuous application of DC voltage.

2.3. Results and Discussion

2.3.1. Ionic Current Rectification and Agarose Concentration Effect

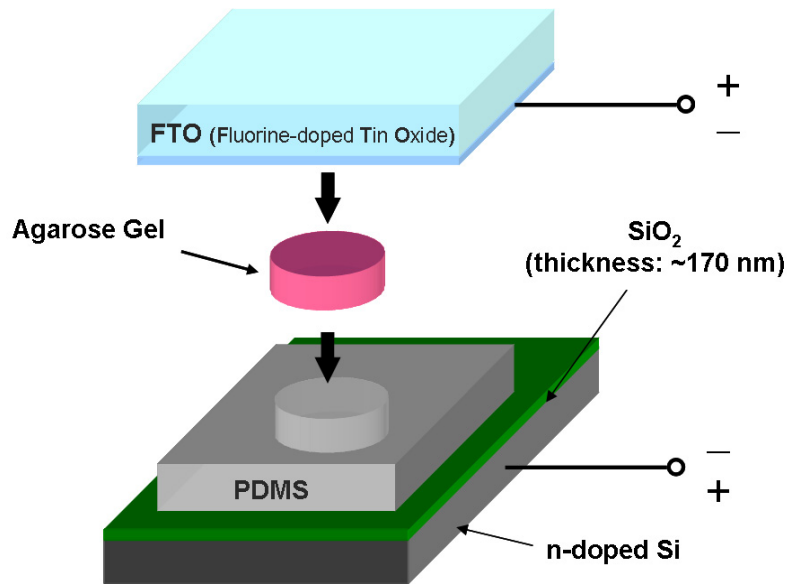


Figure 2.1. Schematic of the structure of the SiO₂ nanofilm/aqueous gel interface (SNAGI) diodes. The active area of agarose gel contacting the SiO₂ layer was around 0.2 cm², and the thickness of the gel layer was 450 μ m. Drawing not to scale.

The structure of the SNAGI diodes is illustrated in Figure 2.1. Highly n-doped Si was used as a conductive electrode on which a SiO₂ layer was grown by thermal oxidation. The SiO₂ layer thickness measured by ellipsometry was 171.1±1.5 nm. An agarose gel slab enclosed in silicone rubber was placed on the SiO₂ layer to form the SiO₂-gel interface. Fluorine-doped tin oxide (FTO) glass was used as the counter electrode. The current density of a typical SNAGI diode as a function of the applied bias is presented in Figure 2.2(a). The concentration of the agarose in the hydrogel was varied between 0 (pure water) and 8 wt. %. When positive voltage was applied to the n-doped Si (backward bias), the current density was suppressed up to the order of 10⁻⁸ A/cm², while, when the polarity was inversed (forward bias), the current drastically increased above around -3 V applied bias.

The current in the forward bias depended on the concentration of the agarose in the hydrogel. The current rectification ratio at ± 5 V as a function of the agarose concentration is displayed in Figure 2.2(b). The diode structure with water/SiO₂ interfaces (0 % agarose) had a rectification ratio of around 1000. For the SNAGI diode with 0.5 wt. % agarose gel phase, the rectification ratio sharply increased to more than 5000. However, the rectification ratio of the diode with 1 wt. % agarose gel decreased and became comparable to that of the diode with water/SiO₂ interfaces. Above 1 wt. %, the rectification ratio slightly decreased as the concentration of the agarose increased. The dependence of the rectification ratio on the agarose concentration seems to be associated with the ionic conductance of the gel layer. To examine the conductance of the gels in terms of the agarose concentration, we measured separately I-V characteristics of the gels inside a symmetric cell with FTO electrodes on both sides. The I-V curves of gels with various agarose concentrations (Figure 2.3) proved that they carry higher current densities than pure water and the 0.5 wt. % gel exhibited the highest conductance. The maximum in the gel conductance at this agarose concentration may be a result of the competition of two opposite effects. Higher concentration of agarose may increase the conductance of the gel because of negatively charged groups on the backbone and the correspondingly increased surface conductance of the mobile counter ionic double layers.^{33, 34} However, the ionic diffusivity in the agarose gels will be suppressed when the polymer fraction is increased because of the decrease of the pore sizes in the gel.³⁵ The

interplay of these two competing effects may lead to the maximum rectification ratio at an optimal agarose concentration of 0.5 wt. %.

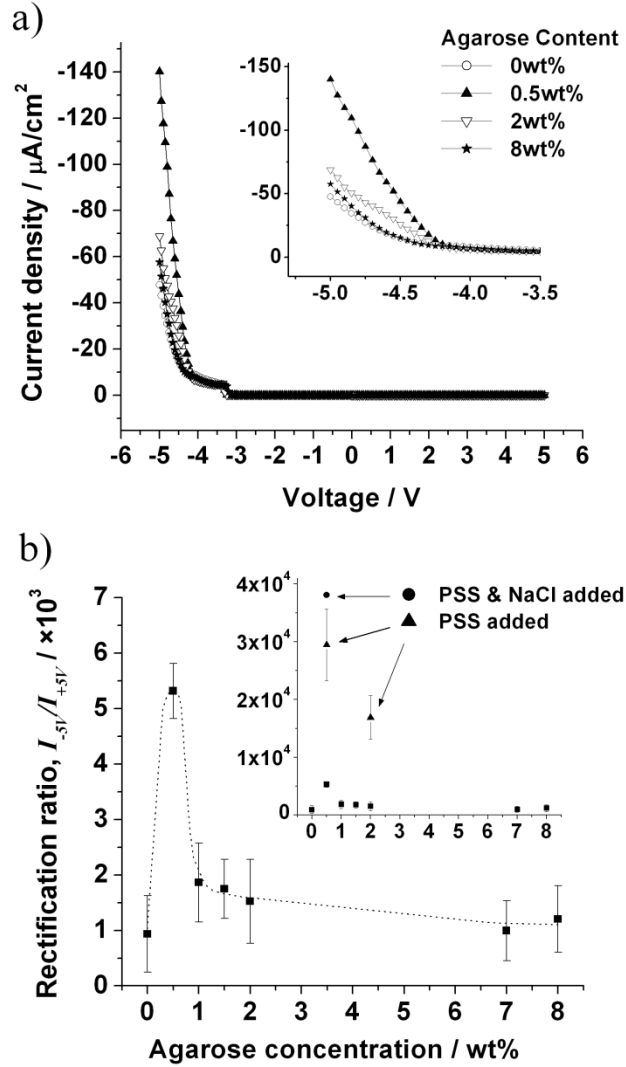


Figure 2.2. Effect of gel composition on the performance of SNAGI diode; (a) Current density as a function of applied bias. Inset: the rescaled plots to examine the current density difference in the forward bias region. (b) Current rectification ratio in terms of agarose concentration. The rectification ratios were calculated from the current density at ± 5 V bias. The dotted line is a guide to the eye. Inset: the rectification ratios of the SNAGI diode after addition of 0.05 M PSS polyelectrolyte and/or 0.05 M NaCl salt. Each point was obtained by averaging results from 4 ~ 9 measurements except the point for the device with the pure water/ SiO_2 interfaces (0 wt. %), which was obtained by averaging data from 27 measurements.

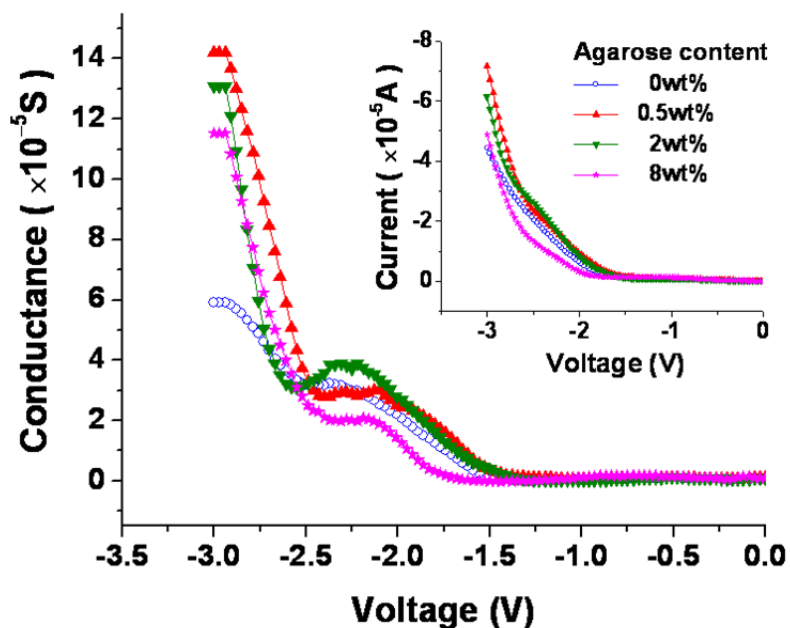


Figure 2.3. Effect of agarose gel composition on the conductance of the gel layer. The conductance values were obtained by differentiation of the I-V curves (inset). The gels were sandwiched between FTO electrodes for measurement of I-V curves. Addition of a small amount of agarose increased the conductance of the gel. Higher concentration of agarose, however, was less effective. These results are in good agreement with the trend of the rectification ratios of the SNAGI diodes in terms of agarose concentration.

2.3.2. Proposed Mechanism of the Ionic Current Rectification

The proposed mechanism of operation of the SNAGI diode is outlined in Figure 2.4. The key factor for the rectification appears to be the charge and type of conductance of the SiO_2 layer. When a negative bias is applied to the doped Si (forward bias), H^+ ions from the hydrogel diffuse through the nanopores of the SiO_2 layer driven by the electric field.³⁶⁻³⁹ Once the ions reach the doped Si, they are possibly reduced and form hydrogen by electrolysis. At the FTO side, anions, such as OH^- , are transported and oxidized, so that the electrons are transferred to the FTO electrode to complete the circuit. When a high current of a couple of milliamperes flowed under forward bias as high as -10 V , gas bubbles were formed on the Si/ SiO_2

electrode, possibly resulting from the generation of H_2 gas by reduction. On the other hand, when positive bias is applied to n-doped Si (backward bias), the OH^- ionic current is blocked by the SiO_2 nanolayer. Since the isoelectric point of SiO_2 is around pH 2, the surface of the SiO_2 layer at neutral pH is negatively charged, which probably prevents the penetration and/or diffusion of the anions by electrostatic repulsion. Thus, the rectification of SNAGI diodes seems to result from selective ion conductivity by the electrostatic gating of the SiO_2 nanolayer. This mechanism is broadly analogous to Donnan membrane equilibria, where a semipermeable ion-exchange membrane creates an exclusion zone for oppositely charged ions.⁴⁰⁻⁴³

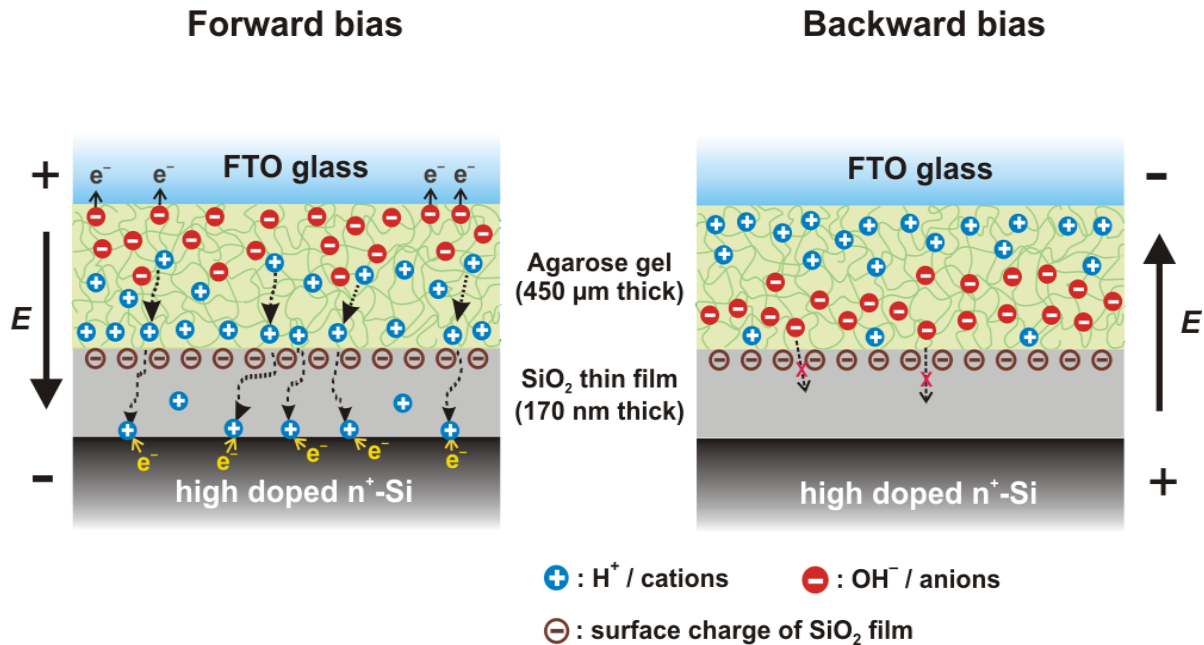


Figure 2.4. Proposed mechanism for nonlinear ionic conductance of SNAGI diode under forward and backward biases.

An alternative mechanism for current rectification in the SNAGI diodes might be asymmetric Fowler-Nordheim (F-N) tunneling through the SiO_2 layer.^{30, 31} However, the data do not support this hypothesis. When bias from -10 V to $+10$ V was applied to a device where we layered metal (Cu or Pt)/170 nm thick SiO_2 /n-doped Si, neither current larger than 1 nA nor rectification were observed. On the other hand, forward current was observed in a

SNAGI diode structure with a 580 nm thick SiO₂ layer (Figure 2.5), where electron tunneling is hardly expected to occur. For F-N tunneling, a high electric field in the range of 7.5 ~ 10 MV cm⁻¹ should be imposed across the insulating layer.³¹ The maximum electric field across the 170 nm thick SiO₂ layer of the SNAGI diode was less than 3 × 10⁵ V cm⁻¹, which is much lower than the electric field required for F-N tunneling. While F-N tunneling is not expected to be a main mechanism of the operation of the SNAGI diode, tunneling might occur when the protons inside the SiO₂ layer closely approach the n-doped Si electrode. It is possible that SiO₂ nanofilms thinner than the ones studied here might have better rectification and/or current density.

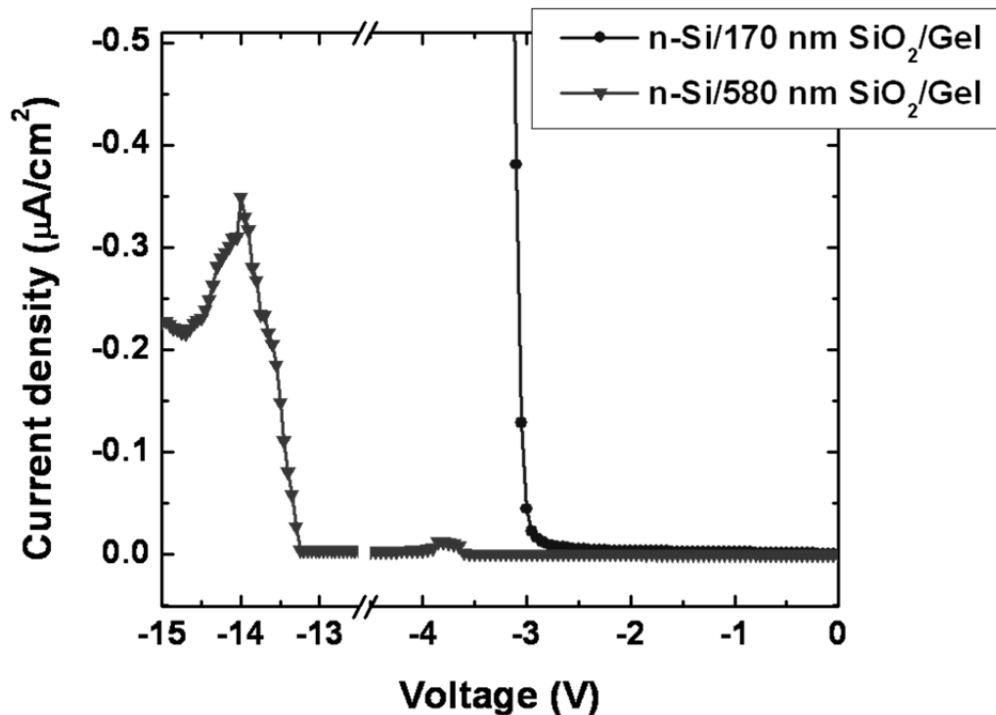


Figure 2.5. Current response as a function of applied bias for SNAGI diodes with different thickness of the SiO₂ layers. Larger negative bias is required to “turn on” the current through thicker SiO₂ layer. The values for turn-on voltage are -3 V for 170 nm SiO₂ and -13.3 V for 580 nm SiO₂, respectively. Current across the SiO₂ layers was measured in both cases, which indicated that the tunneling may not be the dominant mechanism for the charge transport in the SiO₂ nanofilm.

2.3.3. Effect of Salt and Polyelectrolyte on Rectification Performance

The role of the gel in the device is to contain the medium while ensuring efficient ionic conduction. Addition of sodium chloride to the water phase enhances the ionic conductivity because Na^+ and Cl^- ions suppress the electrode polarization by buildup of OH^- and H^+ ions resulting from electrolysis. Indeed, the current rectification ratio increased with the concentration of NaCl (Figure 2.6). Na^+ or Cl^- may also participate in the electrochemical electrode events in the forward bias. The reduction of Na^+ is less likely than proton because the diffusion of Na^+ through the oxide layer is slower and its reduction potential is higher than that of the proton.³⁶ The oxidation of Cl^- ions is likely to contribute to the electron transfer to FTO electrode because Cl^- is oxidized more easily than OH^- .⁴⁴

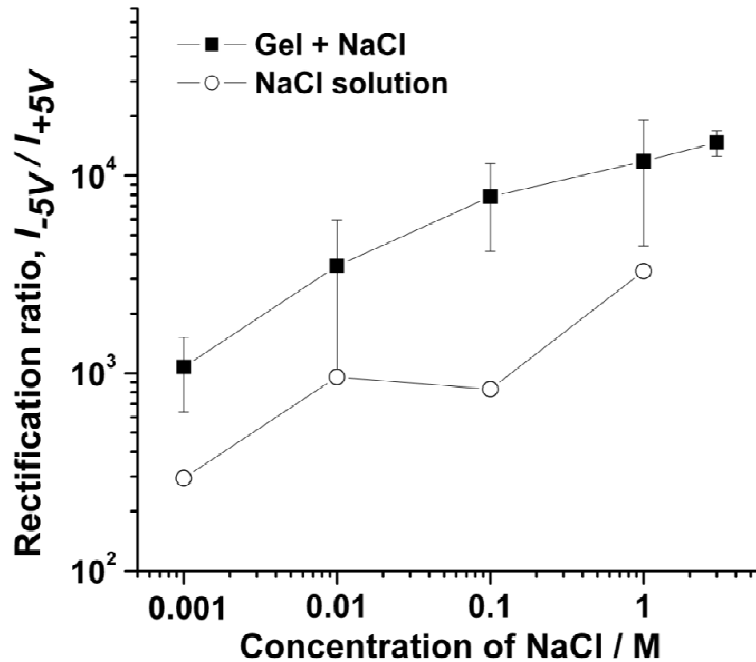


Figure 2.6. Effect of salt (NaCl) concentration on the rectification ratio of SNAGI diode. Agarose gel concentration in all devices was 2 wt. %. As the amount of the salt added to the gel increased, the rectification ratio was enhanced because of the higher conductance of the gel. While the backward current did not show any dependence on the addition of salt, the current under the forward bias increased with the concentration of the salt. These results also confirmed that the introduction of the gel material improved the rectification performance. The solid lines are to guide the eye.

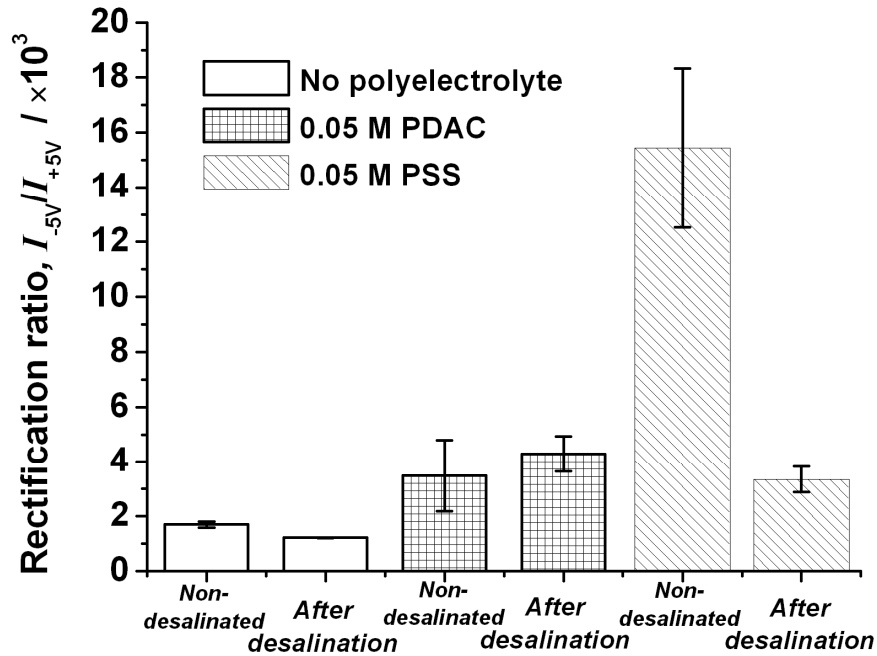


Figure 2.7. Effect of polyelectrolytes on the rectification ratio of SNAGI diodes. All samples contain 2 wt. % agarose. For the deionization of the charged polymer backbone, polyelectrolyte-embedded gels were desalinated by washing with distilled water for 43 hours. The rectification ratio of the PSS gel devices dramatically decreased when the gel, which has positively charged mobile ions (Na^+), was desalinated. The slight decrease of the rectification ratio after desalination in devices without polyelectrolyte suggests that the surface conductance of the agarose gel also contributes to the ion conductance of the gel.

Polyelectrolyte can further improve the performance of the device because the enhanced surface conductance of the charged macromolecular backbone increases the ionic conductance of the gel. Two polyelectrolytes with opposite charges were added to the agarose gel: poly(diallyl dimethylammonium chloride) (PDAC) and poly(styrene sulfonic acid), sodium salt (PSS). PDAC has positively charged macromolecular backbone and mobile anions (Cl^-) and PSS has negatively charged polymer backbone and mobile cations (Na^+). Compared to the SNAGI diode without polyelectrolyte, the rectification ratio of the

device with PDAC increased slightly, while that with PSS increased by one order of magnitude (Figure 2.7). This drastic increase in the rectification ratio with PSS is probably due to an improvement in proton conductivity facilitated by the PSS. The surface conductance of the negatively charged PSS backbone may enhance proton transport both through the gel layer and the interface (note that the H^+ ions also carry the current through the SiO_2 nanolayer). To clarify the role of the surface conductance of PSS, we compared the rectification ratios of the devices prepared from the polyelectrolyte gels before and after desalination. The desalination procedure decreases the concentration of free bulk ions and lowers the charge density of the polyelectrolyte by partial deionization of the charged side groups. The rectification ratio of SNAGI diodes with desalinated PSS gels largely decreased and was on the same order of magnitude as other devices with PDAC or agarose gels. Thus, polyelectrolyte doping can improve the current rectification of the SNAGI diode, which probably results from the enhanced surface conductance of the charged macromolecules.

The performance of the SNAGI diodes with the optimal concentration of 0.5 wt. % agarose improved drastically when PSS was added to the gel (Figure 2.2(b) inset). The current in forward bias increased significantly and the rectification ratio increased up to 3×10^4 . The highest performance of 3.8×10^4 was achieved by further adding salt to the PSS containing gel (Figure 2.2(b) inset). This rectification ratio is two orders of magnitude higher than the ratio in the devices with the nanofluidic channels,³² conjugated ionomer junction,⁴⁵ and conjugated polymer interfaces.⁴⁶ The SNAGI diode performance is also three orders of magnitude better than the diodes with two layers of polyelectrolyte gel that we investigated earlier.²⁸ Although both devices operate on ionic conductance, the replacement of the polyelectrolyte doped gel with very thin film of charged uniform nanoporous oxide leads to drastic improvement of the rectification ratio.

2.3.4. Transient Response and Long Term Stability of SNAGI Diodes

The transient response of the SNAGI diode can be estimated from the data in Figure 2.8. The devices showed good rectification up to a frequency of 100 Hz for more than 30 min field application. The signal shape deteriorated above 100 Hz possibly because of the capacitive

effects by the SiO_2 layer and relatively slow ion transfer in the gel. To examine the long term stability of the devices, we applied continuous DC forward bias of -5V and compared their output current to that of the devices with pure water instead of hydrogel. For the devices with pure water (i.e. diodes with SiO_2 nanofilm/pure water interfaces), the current decayed with time and nearly disappeared within 50 min. These devices were also prone to leaks. The devices with agarose gel sustained a continued forward current for more than 90 min (Figure 2.9). The agarose gel reliably encapsulated the water and kept contact with the SiO_2 layer, which resulted in better stability of the devices.

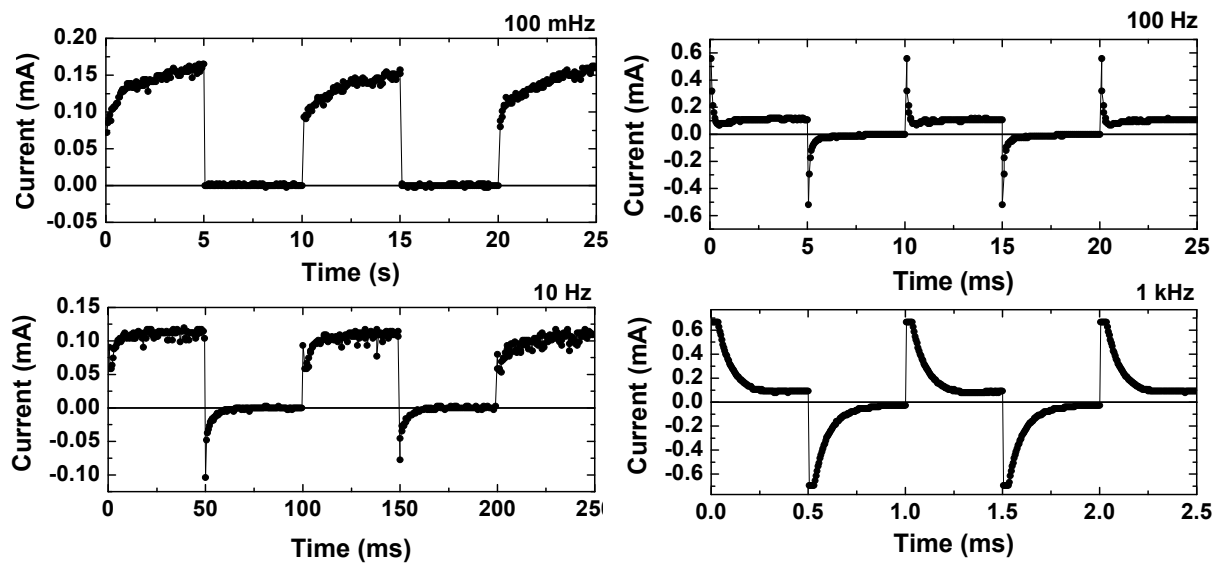


Figure 2.8. Transient current response of SNAGI diode under AC bias with various frequencies. The SNAGI diode displayed good rectification below 100 Hz, above which, however, the rectification deteriorated because of the capacitive effects by the SiO_2 layer and ion transfer in the gel.

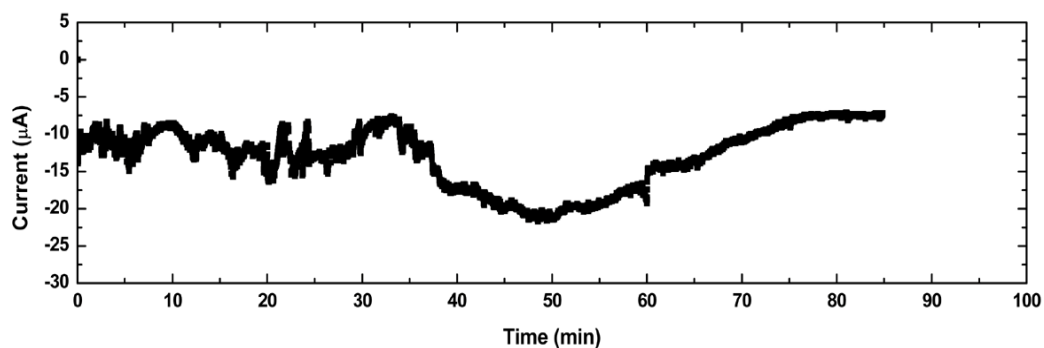


Figure 2.9. Forward current as a function of time from a typical SNAGI diode at a constant forward (-5V) bias. The current through the SiO₂ nanofilm/aqueous gel interface stabilized rapidly and then remained constant for our experimental duration (~ 90 min). The gel layer contains 2 wt. % of agarose.

2.4. Conclusions

In summary, we demonstrate an electrochemical diode by interfacing conducting Si, SiO₂ nanolayer and aqueous gel. The ionic currents were gated by the nonlinear ionic conductivity of the SiO₂ nanolayer. The gel layer not only contributed to the drastic improvement of the performance at the optimal agarose concentration but also brought long-term stability and enabled facile fabrication of the devices. Polyelectrolyte and salt can further improve the ion conductance of the gel and performance of the devices. A SNAGI diode with an exceptional rectification ratio of 3.8×10^4 were constructed by combined doping with polyelectrolyte and salt. These devices are easily encapsulated and demonstrate potential for long-term stability. Further research on the optimization and improvement of the devices could solve the problem of the release of gas at high current densities by e.g., deposition of catalyst or enzyme on the electrodes. Soft matter based diodes could find applications in bioelectronic circuits, liquid sensors, self-propelling “smart” particles,⁴⁷ artificial neural circuits and biomimetic fuel cells and photovoltaics.

2.5. Acknowledgements

This work was supported by grants from DOE (08NT0001925) and NSF-NIRT (CBET-0609087). We thank Dr. Jeong-Seok Na and Dr. Gregory Parsons for assistance with I-V measurements and Dr. Dimiter Petsev for helpful discussions.

2.6. References

1. Gouaux, E. & MacKinnon, R. Principles of selective ion transport in channels and pumps. *Science* **310**, 1461-1465, (2005).
2. Jiang, Y. *et al.* X-ray structure of a voltage-dependent K⁺ channel. *Nature* **423**, 33-41, (2003).
3. Bliznyuk, A. A., Rendell, A. P., Allen, T. W. & Chung, S.-H. The potassium ion channel: Comparison of linear scaling semiempirical and molecular mechanics representations of the electrostatic potential. *J. Phys. Chem. B* **105**, 12674-12679, (2001).
4. Läuger, P., Mechanisms of biological ion transport - Carriers, channels, and pumps in artificial lipid membranes. *Angew. Chem. Int. Ed.* **24**, 905-923, (1985).
5. Sakmann, B., Elementary steps in synaptic transmission revealed by currents through single ion channels (Nobel Lecture). *Angew. Chem. Int. Ed.* **31**, 830-841, (1992).
6. Yasutaka Tanaka, Y. K., Masahiro Sokabe, A non-peptidic ion channel with K⁺ selectivity. *Angew. Chem. Int. Ed.* **34**, 693-694, (1995).
7. Siwy, Z. *et al.* Protein biosensors based on biofunctionalized conical gold nanotubes. *J. Am. Chem. Soc.* **127**, 5000-5001, (2005).
8. Vlassioux, I., Takmakov, P. & Smirnov, S. Sensing DNA hybridization via ionic conductance through a nanoporous electrode. *Langmuir* **21**, 4776-4778, (2005).
9. Kasianowicz, J. J., Brandin, E., Branton, D. & Deamer, D. W. Characterization of individual polynucleotide molecules using a membrane channel. *Proc. Natl. Acad. Sci. U.S.A.* **93**, 13770-13773, (1996).
10. Garcia, A. L. *et al.* Electrokinetic molecular separation in nanoscale fluidic channels. *Lab Chip* **5**, 1271-1276, (2005).
11. Fan, R., Huh, S., Yan, R., Arnold, J. & Yang, P. D. Gated proton transport in aligned mesoporous silica films. *Nat. Mater.* **7**, 303-307, (2008).
12. Karnik, R. *et al.* Electrostatic control of ions and molecules in nanofluidic transistors. *Nano Lett.* **5**, 943-948, (2005).
13. Gracheva, M. E., Vidal, J. & Leburton, J.-P. p-n semiconductor membrane for electrically tunable ion current rectification and filtering. *Nano Lett.* **7**, 1717-1722, (2007).

14. Karnik, R., Duan, C., Castelino, K., Daiguji, H. & Majumdar, A. Rectification of ionic current in a nanofluidic diode. *Nano Lett.* **7**, 547-551, (2007).
15. Wei, C., Bard, A. J. & Feldberg, S. W. Current rectification at quartz nanopipet electrodes. *Anal. Chem.* **69**, 4627-4633, (1997).
16. Umehara, S. *et al.* Current rectification with poly-l-lysine-coated quartz nanopipettes. *Nano Lett.* **6**, 2486-2492, (2006).
17. Siwy, Z. S. Ion-current rectification in nanopores and nanotubes with broken symmetry. *Adv. Funct. Mater.* **16**, 735-746, (2006).
18. Harrell, C. C., Kohli, P., Siwy, Z. & Martin, C. R. DNA-nanotube artificial ion channels. *J. Am. Chem. Soc.* **126**, 15646-15647, (2004).
19. Siwy, Z., Heins, E., Harrell, C. C., Kohli, P. & Martin, C. R. Conical-nanotube ion-current rectifiers: The role of surface charge. *J. Am. Chem. Soc.* **126**, 10850-10851, (2004).
20. Davenport, M., Rodriguez, A., Shea, K. J. & Siwy, Z. S. Squeezing ionic liquids through nanopores. *Nano Lett.* **9**, 2125-2128, (2009).
21. Ali, M., Ramirez, P., Mafel, S., Neumann, R. & Ensinger, W. A pH-tunable nanofluidic diode with a broad range of rectifying properties. *ACS Nano* **3**, 603-608, (2009).
22. Lovrecek, B., Despic, A. & Bockris, J. O. M. Electrolytic junctions with rectifying properties. *J. Phys. Chem.* **63**, 750-751, (1959).
23. Lindner, J., Snita, D. & Marek, M. Modelling of ionic systems with a narrow acid-base boundary. *Phys. Chem. Chem. Phys.* **4**, 1348-1354, (2002).
24. Iván, K., Wittmann, M., Simon, P. L., Noszticzius, Z. & Vollmer, J. Electrolyte diodes and hydrogels: Determination of concentration and pK value of fixed acidic groups in a weakly charged hydrogel. *Phys. Rev. E* **70**, 061402, (2004).
25. Hegedüs, L., Kirschner, N., Wittmann, M. & Noszticzius, Z. Electrolyte transistors: Ionic reaction-diffusion systems with amplifying properties. *J. Phys. Chem. A* **102**, 6491-6497, (1998).
26. Hegedüs, L. *et al.* Nonlinear effects of electrolyte diodes and transistors in a polymer gel medium. *Chaos* **9**, 283-297, (1999).

27. Hegedüs, L., Wittmann, M., Kirschner, N. & Noszticzius, Z. Reaction, diffusion, electric conduction and determination of fixed ions in a hydrogel. *Prog. Colloid Polm. Sci.* **102**, 101-109 (1996).
28. Cayre, O. J., Chang, S. T. & Velev, O. D. Polyelectrolyte diode: Nonlinear current response of a junction between aqueous ionic gels. *J. Am. Chem. Soc.* **129**, 10801-10806, (2007).
29. Zhang, Y. *et al.* Electric field control and analyte transport in Si/SiO₂ fluidic nanochannels. *Lab Chip* **8**, 1671-1675, (2008).
30. Lenzlinger, M. & Snow, E. H. Fowler-Nordheim tunneling into thermally grown SiO₂. *J. Appl. Phys.* **40**, 278-283, (1969).
31. Ravindra, N. M. & Zhao, J. Fowler-Nordheim tunneling in thin SiO₂ films. *Smart Mater. Struct.* **1**, 197-201, (1992).
32. Cheng, L.-J. & Guo, L. J. Ionic current rectification, breakdown, and switching in heterogeneous oxide nanofluidic devices. *ACS Nano* **3**, 575-584, (2009).
33. Serwer, P. Agarose gels: Properties and use for electrophoresis. *Electrophoresis* **4**, 375-382, (1983).
34. Hanauer, M., Pierrat, S., Zins, I., Lotz, A. & Sonnichsen, C. Separation of nanoparticles by gel electrophoresis according to size-and shape. *Nano Lett.* **7**, 2881-2885, (2007).
35. Gu, W., Yao, H. & Vega, A. *IUTAM Symposium on Physicochemical and Electromechanical Interactions in Porous Media*, Springer, Dordrecht, The Netherlands, 193-199, 2005.
36. Hofstein, S. R. Proton and sodium transport in SiO₂ films. *IEEE Trans. Electron Devices* **ED14**, 749-759, (1967).
37. Snow, E. H., Grove, A. S., Deal, B. E. & Sah, C. T. Ion transport phenomena in insulating films. *J. Appl. Phys.* **36**, 1664-1673, (1965).
38. Devine, R. A. B. & Herrera, G. V. Electric-field-induced transport of protons in amorphous SiO₂. *Phys. Rev. B* **63**, (2001).
39. Vanheusden, K. *et al.* Non-volatile memory device based on mobile protons in SiO₂ thin films. *Nature* **386**, 587-589, (1997).
40. Jimenez-Angeles, F. & Lozada-Cassou, M. Simple model for semipermeable membrane: donnan equilibrium. *J. Phys. Chem. B* **108**, 1719-1730, (2004).

41. P. Prakash & SenGupta, A. K. Modeling Al_3^+/H^+ Ion transport in donnan membrane process for coagulant recovery. *AIChE J.* **51**, 333, (2005).
42. L. Weng, W. H. Van Riemsdijk & Temminghoff, E. J. M. Kinetic aspects of donnan membrane technique for measuring free trace cation concentration. *Anal. Chem.* **77**, 2852-2861, (2005).
43. Warren, P. Metrology: Electrifying effects in colloids. *Nature* **429**, 822-822, (2004).
44. Even though the standard electrode potentials of the reduction of Cl^- ($\text{Cl}_2(\text{g}) + 2\text{e}^- \rightleftharpoons 2\text{Cl}^-$, $E^0 = +1.36 \text{ V}$) are a little bit higher than that of the electrolysis of water ($\text{O}_2(\text{g}) + 4\text{H}^+ + 4\text{e}^- \rightleftharpoons 2\text{H}_2\text{O}$, $E^0 = +1.23 \text{ V}$), the predominant process is the reduction of Cl^- because of high overvoltage for oxidation of water. Gas bubbles were barely observed on the FTO electrode because Cl_2 gas dissolves in the water through the further reaction of $\text{Cl}_2 + \text{H}_2\text{O} \rightarrow 2\text{H}^+ + \text{Cl}^- + \text{OCl}^-$.
45. Cheng, C. H. W., Boettcher, S. W., Johnston, D. H. & Lonergan, M. C. Unidirectional current in a polyacetylene hetero-ionic junction. *J. Am. Chem. Soc.* **126**, 8666-8667, (2004).
46. Cheng, C. H. W. & Lonergan, M. C. A conjugated polymer pn junction. *J. Am. Chem. Soc.* **126**, 10536-10537, (2004).
47. Chang, S. T., Paunov V. N., Petsev D. N., Velev O. D. Remotely powered self-propelling particles and micropumps based on miniature diodes, *Nat. Mater.* **6**, 235-240, (2007).

Chapter 3

Ionic Current Rectification in Soft Matter Diodes with Liquid Metal Electrodes*

* Partially based on So, Koo, Dickey and Velev, *Adv. Funct. Mater.*, 2012, 22, 625

3.1. Introduction

There has been increasing interest in soft devices inspired by biological systems.¹⁻³ Various types of devices made of soft materials, such as polymers, gels and liquids, have been constructed including diodes,^{4, 5} transistors,⁶⁻¹⁰ antennas,¹¹⁻¹³ sensors,¹⁴ actuators,^{15, 16} batteries,^{17, 18} supercapacitors,^{19, 20} memristors,²¹ and solar cells.^{22, 23} Soft materials are appealing because they are often stretchable, flexible, and conformal. Due to their ease of physical deformation, devices made of soft materials could find potential applications that include portable or wearable electronics and bioprosthetic devices such as artificial organs,²⁴ muscle,²⁵ neural tissue or skin.^{14, 26, 27} We describe the operating principles of a new class of diodes constructed entirely from soft materials such as hydrogels infused with electrolytes and liquid metal electrodes.

Directional conduction of an ionic current is one of the key processes in many essential biological functions, such as adenosine triphosphate (ATP) synthesis and neural transmission. Our group reported previously ionic current diodes made of soft, aqueous gel operating on ionic current. One approach is based on an interface between two hydrogel layers doped with differently charged polyelectrolytes that is analogous to the p-n junction of a Si diode.⁴ A SiO₂ nanofilm/aqueous gel interface (SNAGI) shows ionic current rectification due to the electrostatic gating of the negatively charged SiO₂ nanolayer.⁵ In these gel-based diodes, a network of agarose polymer provides the physical matrix that allows the liquid media to be confined and shaped. Although the gel materials are soft and flexible, the rigid electrodes used in those devices, such as platinum, fluorine-doped tin oxide (FTO) glass and highly doped Si wafers make the overall device rigid. Replacement of the solid electrodes with soft metallic material is required for making a truly soft diode.

Eutectic gallium indium (EGaIn), an alloy of 75 % gallium and 25 % indium, could be an alternative to the rigid electrodes commonly used to interface gels since it is a low viscosity liquid at room temperature and has high electrical conductivity ($\sigma = 3.4 \times 10^4$ S/cm). Electronic devices such as stretchable antennas,¹¹⁻¹³ interconnects,²⁸⁻³⁰ electromagnets,³¹ microcomponents,³²⁻³⁵ and reconfigurable wires³⁶ have been fabricated utilizing the fluidic properties of low melting point metal alloys. The surface of EGaIn

spontaneously forms a thin, native skin of gallium oxide.³⁷ The oxide skin passivates the liquid metal and does not grow with time unless an external driving force is applied (e.g., temperature, electrical potential).³⁸ The oxide layer is less conductive than the metal (pure, crystalline gallium oxide is a wide band gap semiconductor), and can be formed or removed by the applied bias. This property makes it possible to construct resistive switching memory devices, in which the state of the resistance can be recorded in the form of the thickness of the oxide.²¹ We report here how the ability to control the thickness of the oxide layer on the liquid metal could be used to achieve electrical rectification in a novel class of soft matter diodes composed of liquid metal and hydrogel. Similarly, anodic oxide film of valve metals (e.g., Ta, Zr, Ti and Al) has been reported to show current rectification in dry (metal/oxide/metal) or wet (metal/oxide/electrolyte) conditions.³⁹ However, the typical valve metals are rigid and the current rectifying mechanism of the metal oxides is derived from their semiconducting characteristics rather than the varying thickness of the oxide films.

The new class of ionic current diodes is made entirely of soft matter by interfacing hydrogel with EGaIn electrodes. First, we investigate the rectification of ionic current at the interface of EGaIn/aqueous electrolyte solution/Pt as a model system. The thickness of the oxide skin at the EGaIn/aqueous electrolyte interface controls the resistance through the device. The ionic current flows in the direction of the bias reducing the oxide skin on EGaIn, while an oxidizing bias suppresses the current. We characterize the effect of the conductivity and pH of the electrolyte solutions on the rectification ratio of the devices. We then demonstrate that replacing the aqueous electrolyte solution with hydrogel (EGaIn/hydrogel/Pt) improves the rectification ratio and enables easy handling and thus practical fabrication of devices. Finally, we discuss the fabrication of diodes composed entirely of soft materials (EGaIn/ hydrogel 1/hydrogel 2/EGaIn) by stacking two polyelectrolyte gel layers with different pH to create the necessary asymmetry for rectification.

3.2. Experimental Section

3.2.1. Materials and Device Fabrication

The EGaIn electrodes in the device comprised of EGaIn/electrolyte/Pt, were prepared by injecting the liquid metal into a linear microfluidic channel. EGaIn protruding out of one end of the channel was interfacing electrolyte solutions or hydrogels. The stock phosphate buffer solution was made by mixing 0.2 M NaH_2PO_4 and 0.2 M Na_2HPO_4 aqueous solutions at a ratio of 4:6. The conductivity of the electrolyte solutions was varied by changing the concentration of the stock buffer solution. To investigate the effect of pH environment on the rectification performance of the diode, the PAA (M_w 100,000, Sigma-Aldrich) and PEI (M_w 750,000, Sigma-Aldrich) polyelectrolytes were added to water until the conductivity becomes comparable with that of the reference buffer solution with neutral pH ($\sim 810 \mu\text{S}/\text{cm}$).

The hydrogel was prepared by following the procedure reported previously.⁵ The stock phosphate buffer solution was used to prepare the gel with high conductivity. PAA (7.2 wt. %) and PEI (5.7 wt. %) were added as dopants of polyelectrolyte gels to form the asymmetric junction of all soft matter based diodes. The detailed fabrication procedure of the device is described in our previous report.²¹

3.2.2. I-V Measurement

The I–V characteristic curves were obtained by using a computer controlled source meter (Keithley 2400, Keithley Instruments Inc.). The time dependent current behavior under repetitive and continuous biases was measured by using DC regulated power supply (Extech Instruments) and a digital multimeter. The transient responses of the prototype of all soft matter diodes to AC bias were measured using a function generator and computer-controlled digital oscilloscope (22120A, 34405A, and DSO3202A, respectively, all products of Agilent Technologies). A square-wave AC signal with a frequency of 0.5 Hz and amplitude of ± 3 V was applied to the device connected in a series with a 100 k Ω resistor when measuring the AC voltage across the device.

3.3. Results and Discussion

3.3.1 Ionic current rectification at the interface of EGaIn/electrolyte/Pt

We first investigated a simple model system consisting of EGaIn/electrolyte solution/Pt. A representative current-voltage (I-V) trace of the system and the experimental setup are shown in Figure 3.1. We define forward and backward biases as the negative and positive biases applied to the EGaIn electrode, respectively. The current is suppressed between 0 to -3 V, but increases rapidly at potentials more negative than -3 V. In contrast, positive biases show a continuous and gentle increase in the magnitude of the current. The absolute value of the current at -5 V is ten times higher than that at $+5$ V. Such diode-like characteristics of the system result from the formation or removal of the insulating oxide film at the interface between the EGaIn electrode and the electrolyte solution.²¹ Negative bias applied to the EGaIn electrode reduces the resistive oxide on the surface of the EGaIn electrode, and thus renders the EGaIn/electrolyte solution interface more conductive. The formation and removal of the oxide skin is apparent to the naked eye. In the absence of the resistive oxide skin (i.e., at potentials more negative than -3 V), the current increases noticeably and bubbles form on the EGaIn surface, presumably due to the electrolysis of water. Since the standard reduction potential of the oxide film is about -1.0 V vs. SHE (standard hydrogen electrode),⁴⁰ the hydrogen generation is supposed to occur prior to the reduction of the oxide during the negative bias sweep. However, the oxide film passivates the EGaIn electrode, thereby hindering the supply of protons to the electrode for the hydrogen generation reaction. The current at positive potentials is likely due to the thickening (i.e., anodizing) of the oxide layer. The oxide layer acts as an insulating barrier, retarding electrochemical reactions such as water electrolysis and further growth of the oxide layer. The inert Pt electrode on the other side does not form any oxide film on its surface and hence stays conductive in this bias range from -5 V to $+5$ V. Thus, the asymmetric configuration of the reversibly anodizable EGaIn electrode and inert Pt electrodes provide ionic current rectification.

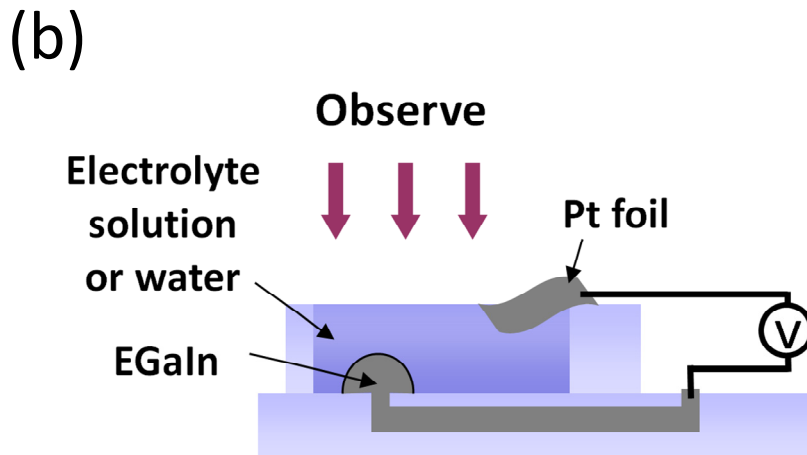
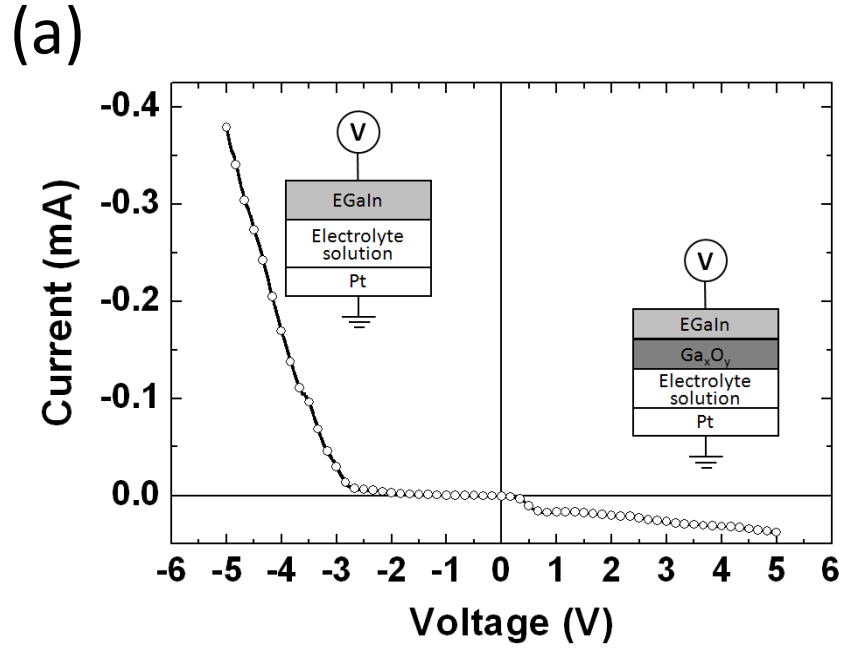


Figure 3.1. (a) Current rectification of an EGaIn/electrolyte solution (aq)/Pt diode. The negative (forward) bias reduces the insulating oxide layer at the interface of the liquid metal. The positive (backward) bias oxidizes the liquid metal resulting in a resistive barrier for electrical current. The electrolyte is NaH_2PO_4/Na_2HPO_4 buffer solution with a conductivity of 3.2 mS/cm. (b) Schematics of the experimental setup of EGaIn/electrolyte solution or water/Pt diode. The surface of the EGaIn electrode was observed under an optical microscope to obtain the images shown in Figure 3.2.

To elucidate the effect of the electric potential on the formation/reduction of the oxide film on the EGaIn electrode, we observed the surface of an EGaIn electrode in water while changing the applied bias (Figure 3.2) relative to a grounded Pt electrode. We used deionized water as medium to understand the general behavior of the diode in aqueous systems excluding the effect of different types and concentration of electrolyte ions. The surface of the electrode looks slightly hazy before applying bias because of the spontaneous formation of a native oxide skin. Applying a positive bias of + 5 V to the EGaIn electrode causes haziness and crumbling on the surface due to the oxide film thickening. After applying the positive bias for a couple of seconds, however, we observe no further changes in the morphology of the oxide layer, which is consistent with our hypothesis of the self-limiting oxide growth for the backward current in Figure 3.1(a). Applying a negative bias to the electrode causes it to become shiny and reflective, which suggests the metal surface is nearly free of the oxide film. The negative bias first reduces the oxide skin, and then generates bubbles presumably due to the electrolysis of water. The observations in Figure 3.2 confirm the hypothesis that the formation/reduction of the insulating oxide skin on the EGaIn electrode depends on the direction of the electric bias, thereby leading to the unidirectional ionic current characteristics of the EGaIn/electrolyte solution/Pt diode shown in Figure 3.1(a).

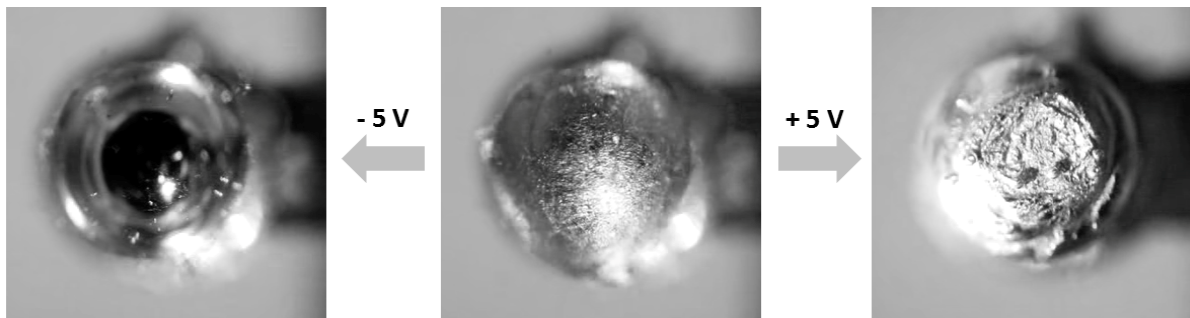


Figure 3.2. Top-down optical microscope images of an EGaIn liquid metal electrode of a diode comprised of EGaIn/H₂O/Pt before (middle) and after (left and right) applying biases. The surface of the liquid metal is oxidized or reduced by applying + 5 V or - 5 V, respectively. The schematic of the experimental setup is shown in Figure 3.1(b).

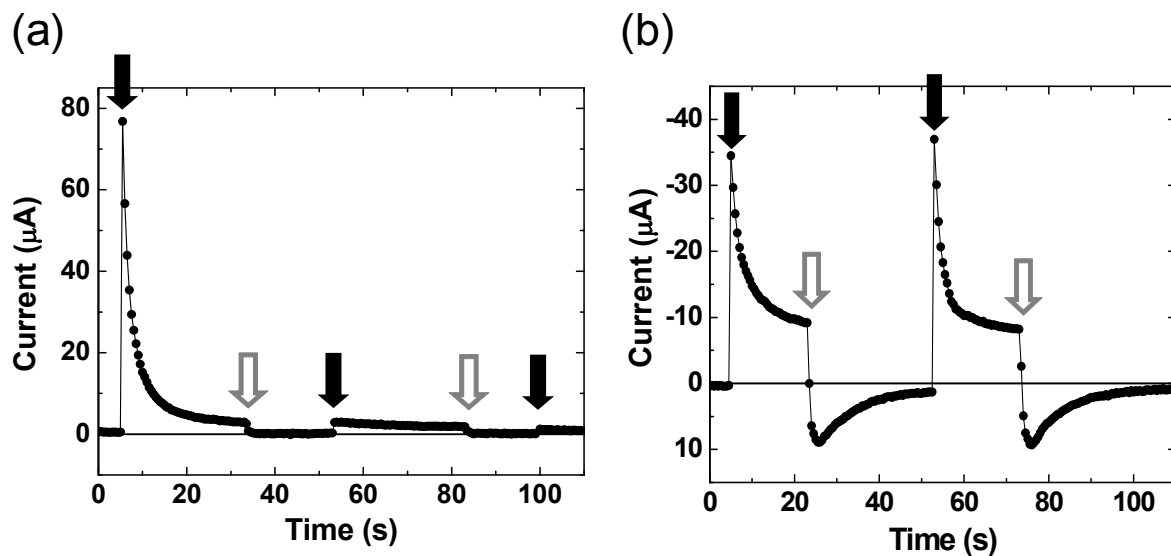


Figure 3.3. Current of an EGaIn/H₂O/Pt diode under repetitive (a) oxidative (+ 3 V) and (b) reductive (- 3 V) biases with time. The filled and empty arrows indicate the time when the bias was turned on and off, respectively.

The time-dependent current response of the EGaIn/H₂O/Pt diode under repetitive application of a positive or negative bias shows clearly the electrochemical characteristics of the oxide film on EGaIn under the backward and the forward bias (Figure 3.3). Application of a positive (backward) bias to the EGaIn electrode immediately generates large current resulting from the formation of the oxide film (Figure 3.3(a)). However, since this oxide film retards the ion transport for further oxide buildup, the current decreases by more than an order of magnitude within ten seconds. After a short period (~ 20 sec) with no applied bias, the current remains suppressed upon reapplying the bias, which indicates that the thickened oxide film is maintained even upon removal of the bias. Application of a negative bias to the EGaIn electrode reduces the oxide film and water electrolysis occurs at the interface, which results in a higher current relative to the positive bias (Figure 3.3(b)). Under a continuous bias, the forward current is sustained ~ 10 times higher than the backward current (Figure 3.4). Turning off the negative bias creates a pulse of positive current, presumably due to the regeneration of the native oxide skin. The current from spontaneous oxidation decays by about an order of magnitude after ~ 30 sec. Based on the derivative of the current with time, the rate of the spontaneous formation of the oxide film on the pristine EGaIn electrode

is ~ 40 times slower than that of the forced oxidation with + 3 V bias as shown in the first cycle of Figure 3.3(a). Moreover, the integrated current from the generation of native oxide is smaller than the integrated current from the growth of oxide with applied bias, which suggests that the native oxide without electric bias is thin relative to the oxide grown by positive bias. We observed visually the spontaneous formation of the oxide skin after turning off the negative bias (c.f., Figure 3.2). Thus, the oxide formation on the EGaIn electrode is a spontaneous and self-limiting reaction and the positive bias oxidizes the EGaIn electrode further, thereby forming a thicker oxide film.

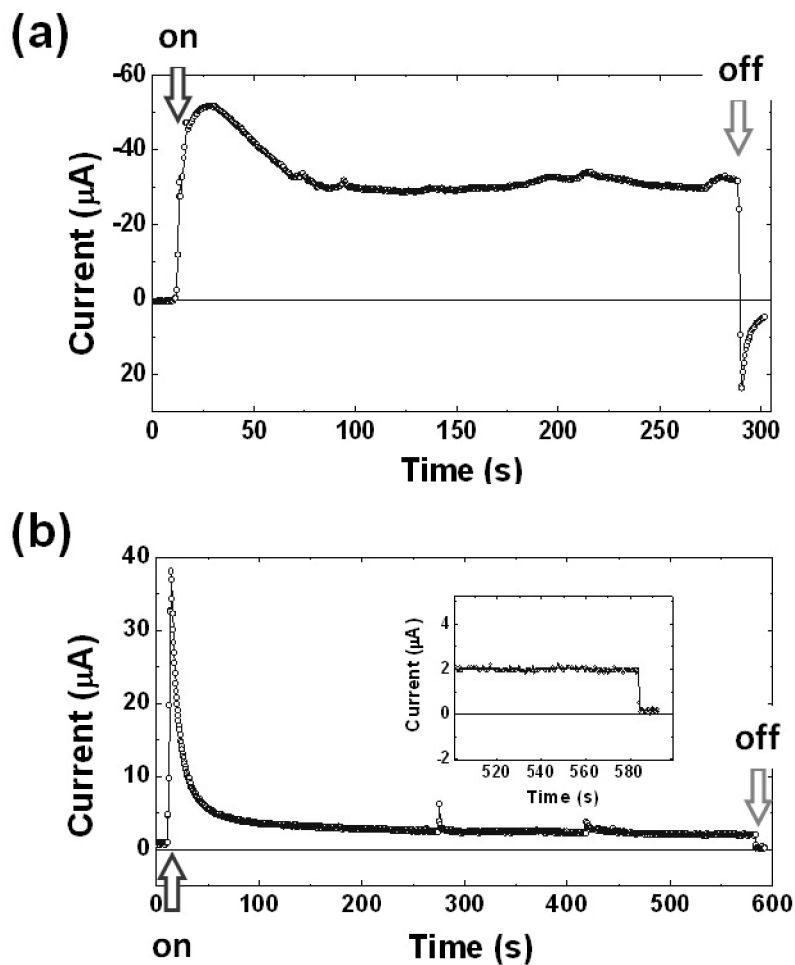


Figure 3.4. Current vs. time under continuous (a) reductive (- 5 V) or (b) oxidative (+ 5 V) bias. Inset in (b) is the magnified plot of (b) after 500 seconds.

3.3.2 Effect of the conductivity and pH of the electrolyte solutions on the rectification at the interface of EGaIn/electrolyte/Pt

The forward current of the device with EGaIn/electrolyte/Pt interface originates mostly from the electrolysis of water or electrolyte. The rate of electrolysis should depend on the ionic conductivity of the electrolyte between the two electrodes. To investigate the effect of the conductivity of the electrolyte on the device performance, we prepared four different concentrations of sodium phosphate buffer solution with neutral pH. The conductivity of these electrolyte solutions varies from 0.093 mS/cm to 31 mS/cm, which is more than 300× higher than the lowest conductivity. The effect of the conductivity of the electrolyte on the forward/backward current of the device is shown in Figure 3.5. The forward current increases in proportion to the conductivity of the electrolyte, while the backward current is not affected as much as the forward current. The backward current is limited by the oxide layer rather than the conductivity of the electrolyte media. Due to the dominant dependence of the forward current on the electrolyte concentration, the rectification ratio of the device increases with the conductivity of the electrolyte (Figure 3.5 (c)), which can be fitted with a power law dependence with an exponent ~ 0.6 . This dependence reflects the complex difference in the device conductivity on the forward and the backward ion currents. Contrary to polyelectrolyte gel diodes that we reported previously (which rectify at the gel/gel interface),⁴ the diodes based on oxide films, such as SNAGI diodes⁵ and EGaIn/electrolyte/Pt diodes, show higher rectification performance at higher ionic conductivity, resulting from the efficient suppression of the backward current by the oxide barrier.

The pH of the electrolyte solutions could affect the rectification of the diodes since strong acids or bases etch the oxide layer.⁴⁰ The formation of the insulating oxide film during the positive sweep is a key mechanism for suppression of the backward current. We studied the effect of the electrolyte medium pH on the rectification by using solutions of polyacrylic acid (PAA), polyethylene imine (PEI) and sodium phosphate buffer (**Figure 3.6**). The pH values of the PAA, sodium phosphate buffer and PEI electrolyte solutions are ~ 3 , ~ 7 and ~ 11 , respectively. We adjusted the conductivity of the solutions to the same value

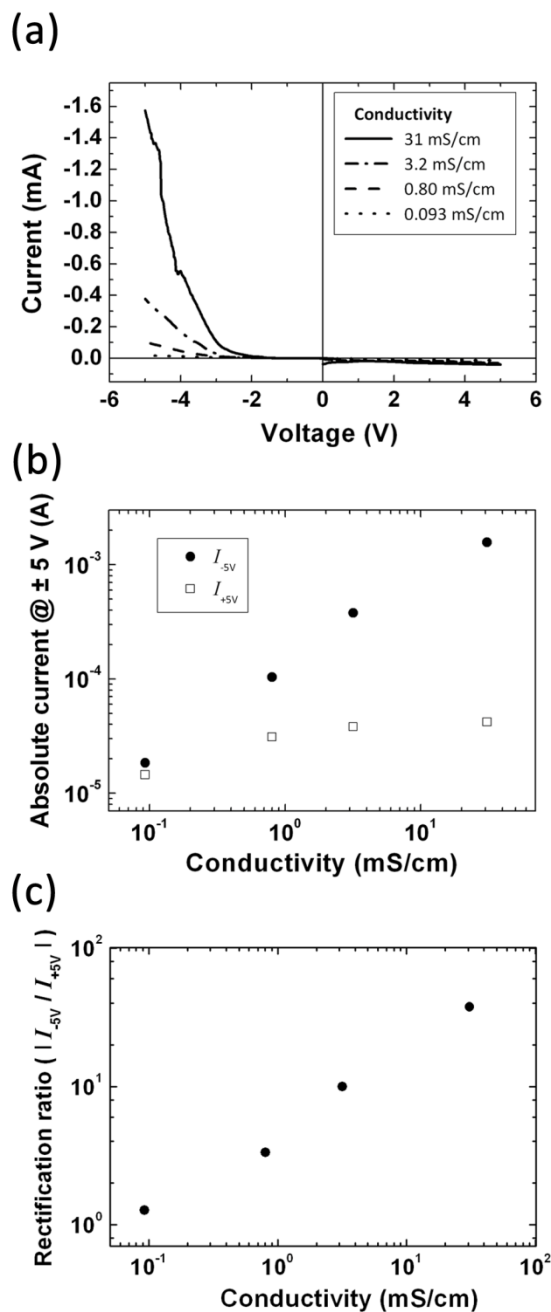


Figure 3.5. Effect of the conductivity of the electrolyte on the rectification behavior. (a) Current as a function of applied voltage of the devices with different conductivity of the electrolyte. (b) Current values and (c) rectification ratios at ± 5 V in terms of the conductivity of the electrolyte. The conductivity of the electrolyte varies by the phosphate buffer concentration. The rectification ratios were calculated from the current at ± 5 V bias. The pH of the electrolyte buffer solutions is ~ 7 .

(~ 810 S/cm) by controlling the concentrations of the electrolytes to avoid the effects of conductivity, discussed earlier. The negative sweep of the I-V traces shows no significant dependence of the forward current on the pH of the electrolytes. The positive sweep, however, suppresses the current at pH 3 (PAA solution) and 7 (neutral buffer solution), whereas large backward current is measured at pH 11 (PEI solution) resulting from the poor stability of the oxide film.⁴⁰ The current peak observed at ~ 3 V is likely associated with electrochemical

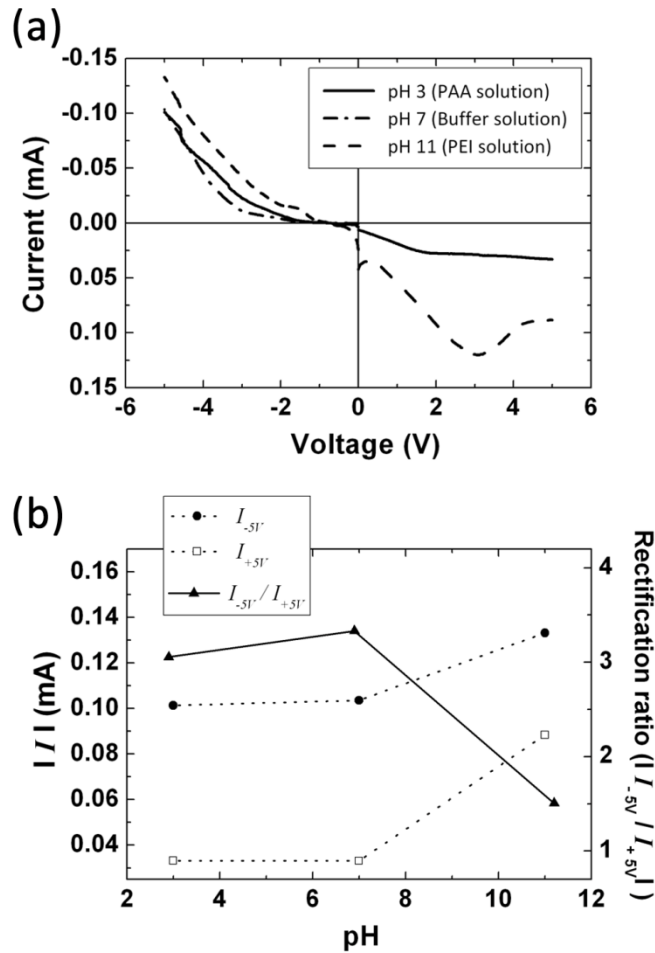


Figure 3.6. Effect of pH of the electrolyte interfacing the liquid metal electrode on the rectification behavior. (a) Current as a function of voltage of the device with electrolytes of different pH values. (b) Current values at ± 5 V bias and rectification ratios in terms of pH of the electrolytes. The conductivity of the electrolyte solutions are ~ 810 μ S/cm

events that only occur in the absence of the passivating skin. We observed a similarly shaped I-V trace in devices featuring a NaOH solution with the same pH as the PEI solution. The characteristic shape of the I-V trace at basic pH values may be explained by the competition of the oxidation reaction due to the bias and the removal of the oxide by base or, alternatively, the mass-transfer limited reaction typically shown in potential sweep methods.⁴¹ Based on the current at ± 5 V, the device showed the highest rectification ratio with the neutral pH electrolyte and the lowest rectification ratio with the basic pH electrolyte due to the inefficient suppression of the backward current (Figure 3.6 (b)).

3.3.3 Ionic current rectification at the interface of EGaIn/hydrogel/Pt

The use of liquid electrolyte solution in the EGaIn/electrolyte solution/Pt diode could limit the usability of practical devices due to leakage of the liquid medium. Hydrogel infused with the electrolyte could replace the liquid medium for better encapsulation and ease of handling. Moreover, charged groups along the polymer backbone of the gel can improve the ionic conductivity,⁵ thereby increasing the forward current and the rectification performance. The

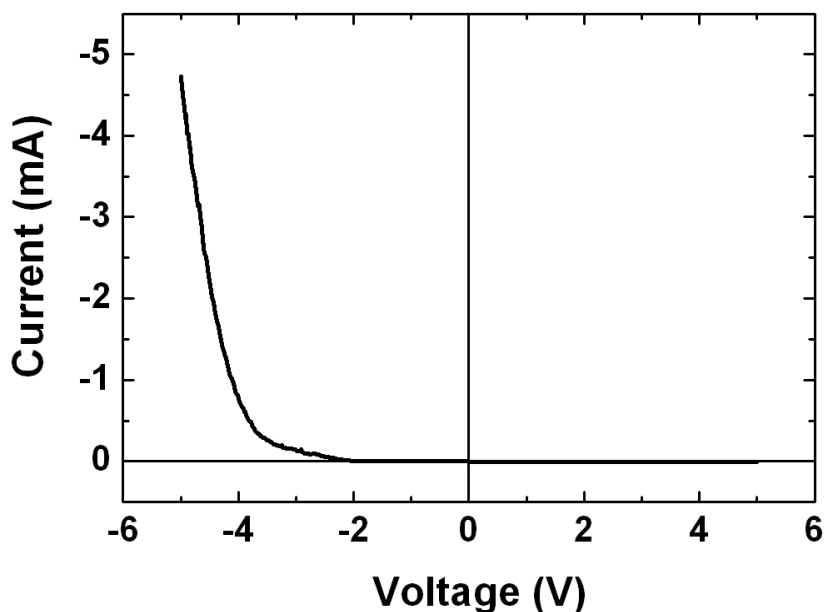


Figure 3.7. Representative I-V trace of a diode comprised of EGaIn/hydrogel/Pt. The hydrogel is made of an aqueous sodium phosphate buffer solution with a conductivity of 31 mS/cm.

I-V traces of such a device with EGaIn/hydrogel/Pt interface are shown in Figure 3.7. The hydrogel contains 98 wt. % of the sodium phosphate buffer solution with a conductivity of ~ 31 mS/cm and 2 wt. % of agarose. Due to the increased ionic conductivity by the gel, the forward current at -5 V increased by a factor of ~ 3 compared to devices containing the same concentration of sodium phosphate buffer dissolved in water (solid line in Figure 3.5(a)). It should be noted that the backward current is also efficiently suppressed to ~ 10 μ A in the device with the gel. The diode exhibits a rectification ratio as high as ~ 450 at ± 5 V. Thus, replacing the electrolyte solution with hydrogel creates an ionic charge transport diode with improved rectification performance.

3.3.4 All soft matter diodes formed using asymmetric polyelectrolyte gels with different pH

The previously described devices have rigid Pt electrodes. To fabricate diodes composed entirely of flexible soft materials, we replaced the Pt electrode with a second EGaIn electrode and fabricated diodes comprised of EGaIn/hydrogel 1/hydrogel 2/EGaIn. Asymmetry is required for diode rectification. In the diodes containing Pt, the asymmetry arises from the fact that EGaIn can form an insulating oxide skin but Pt does not. To achieve asymmetry in the EGaIn/hydrogel 1/hydrogel 2/EGaIn structure, we stacked two gel layers each doped with different polyelectrolytes to control the local pH values as shown in Figure 3.8(a). The I-V trace in Figure 3.8(b) demonstrates that the current increases with negative bias and suppresses in the positive bias to achieve a rectification ratio of ~ 14 . We investigated the transient response of the soft matter device under alternating electric field with a frequency of 0.5 Hz (Figure 3.8(c)). We connected the diode in series with a 100 k Ω resistor and measured the voltage differential across the electrodes, which is proportional to the diode resistance. The graph clearly shows rectification due to asymmetric conductance. In the high resistance state (high output voltage periods), the voltage gradually increases with time, possibly because of the delayed charging process limited by the diffusion of ions after sudden change of the voltage.

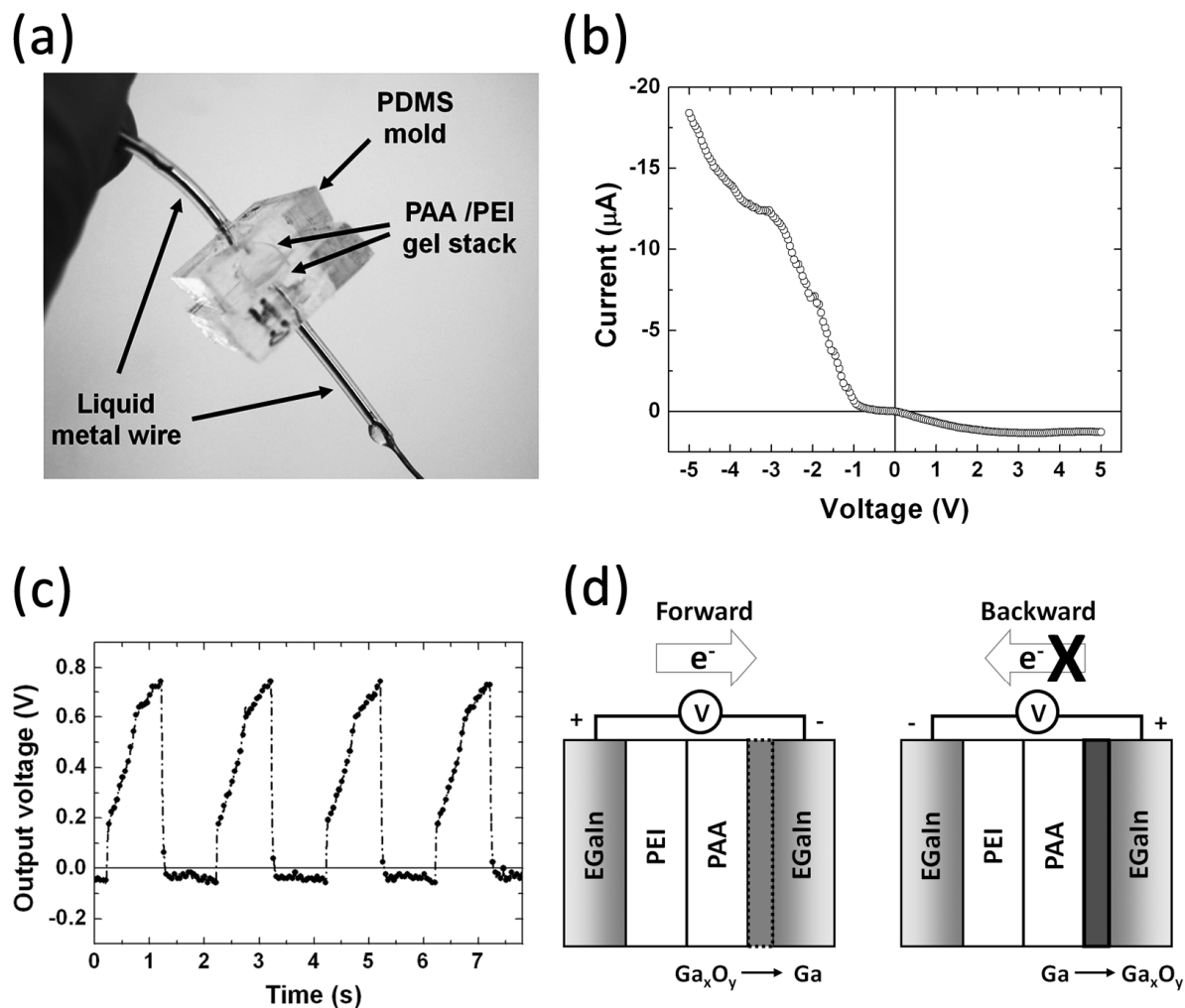


Figure 3.8. (a) Photograph of a prototype diode composed entirely of soft matter. (b) Current as a function of applied voltage and (c) transient voltage response of the soft matter diode under AC signal. The EGaIn interfacing the PEI gel is grounded. The output voltage is the voltage applied to the diode under AC bias with amplitude of ± 3 V. (d) A schematic depiction of the soft matter diode with asymmetrically configured polyelectrolyte gels under forward and backward biases.

The structure and the operating mechanism of these all-soft matter based diodes are shown in Figure 3.8(d). Two EGaIn electrodes sandwich the two gel layers doped with PAA and PEI (i.e., EGaIn/PEI gel/PAA gel/EGaIn). In the absence of electric bias, the PEI polyelectrolyte gel is basic enough to remove the oxide skin on the EGaIn electrode, and thus, the oxide film forms only at the interface between the PAA polyelectrolyte gel and the

EGaIn electrode. Applying a positive bias (backward bias) to the EGaIn/PAA gel leads to formation of a thick oxide film at the interface of EGaIn/PAA and suppresses the current through the device. However, applying a negative bias (forward bias) to the EGaIn/PAA gel reduces the oxide skin at the interface of EGaIn/PAA and renders the diode conductive since the interface of the EGaIn/PEI electrode remains relatively free of oxide due to the local pH.

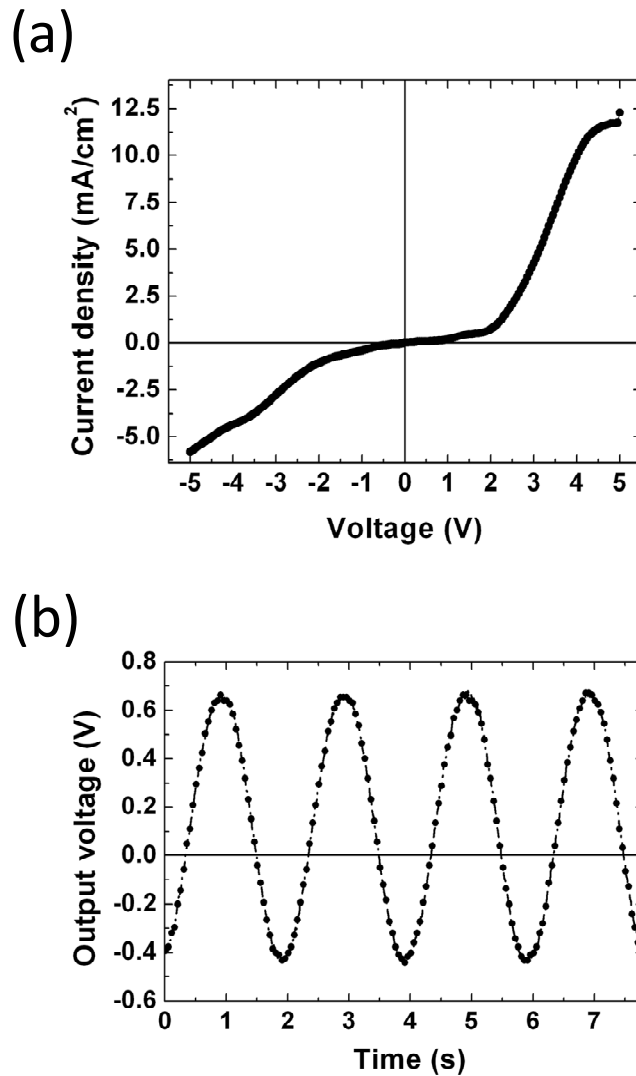


Figure 3.9. (a) Current as a function of applied voltage and (b) transient voltage response under wave AC field of the Pt/PEI gel/PAA gel/Pt device. The slight asymmetry of the output signals may result from the interface between two different polyelectrolyte gels.

Rectification behavior is not observed in devices featuring two Pt electrodes (Figure 3.9), which confirms that the asymmetric interfaces of the polyelectrolyte gel/EGaIn electrodes (EGaIn/PAA gel and EGaIn/PEI gel) rather than the junction of the two polyelectrolyte gels (PEI gel/PAA gel) play an important role in the diode characteristic of the all soft matter device. The same configuration can achieve memristor-like behavior (i.e., resistive switching) depending on the history of the applied bias, which has been reported elsewhere.²¹ Thus, we demonstrate a prototype diode composed entirely of soft matter based on interfacing EGaIn electrodes with hydrogels doped with different polyelectrolytes. Under alternating electric field with high frequency, the slow ion mobility could be a limitation in such devices operated by ionic current.⁵ Scaling down of the device dimensions can allow the operation of the device at faster bias change rates. Further experiments are under way to establish the effect of the device dimensions on the operation frequency range of these diodes.

3.4. Conclusions

We demonstrate ionic current rectification in a system composed of EGaIn liquid metal/electrolyte solution/Pt. Rectification is achieved by the formation and reduction of the insulating oxide film on the EGaIn electrode. The asymmetric configuration of the electrodes (i.e., electrochemically active EGaIn and inert Pt) enables the current to flow unidirectionally. The forward current is limited by ion transport and depends on the conductivity of the electrolyte solution. The backward current is suppressed by the formation of the oxide film on the EGaIn and is affected by the pH of the electrolyte solution, which changes the stability of the oxide layer on EGaIn. Replacing the electrolyte solution with hydrogel provides better encapsulation of the electrolyte solution and improves rectification performance as high as ~ 450 by increasing the conductivity. Finally, we constructed a prototype of a diode composed entirely of soft matter by interfacing EGaIn electrodes and polyelectrolyte gels with different local pH. The materials used in these devices are flexible, moldable, and soft, and their fabrication process is simple. As the soft matter diodes operate based on ionic current and reactions of EGaIn electrodes with aqueous electrolytes, they are compatible with water-based or high humidity systems. Since biological systems generally

have soft, curved, and in some cases moving surfaces and tend to be operated by ionic current rather than electronic current, such a soft, ionic current diode could find potential applications in neuromorphic systems, bio-embeddable smart particles and biomimetic devices.

3.5. Acknowledgements

This study was supported by grants from the US National Science Foundation (CMMI-0954321 & CBET-0828900) and US Department of Energy (08NT0001925).

3.6. References

1. Osada, Y. & Gong, J.-P. Soft and wet Materials: Polymer gels. *Adv. Mater.* **10**, 827-837, (1998).
2. Quake, S. R. & Scherer, A. From micro- to nanofabrication with soft materials. *Science* **290**, 1536-1540, (2000).
3. Hamley, I. W. Nanotechnology with soft materials. *Angew. Chem. Int. Ed.* **42**, 1692-1712, (2003).
4. Cayre, O. J., Chang, S. T. & Velev, O. D. Polyelectrolyte diode: Nonlinear current response of a junction between aqueous ionic gels. *J. Am. Chem. Soc.* **129**, 10801-10806, (2007).
5. Koo, H.-J., Chang, S. T. & Velev, O. D. Ion-current diode with aqueous gel/SiO₂ nanofilm interfaces. *Small* **6**, 1393-1397, (2010).
6. Hegedus, L., Kirschner, N., Wittmann, M. & Noszticzius, Z. Electrolyte transistors: Ionic reaction-diffusion systems with amplifying properties. *J. Phys. Chem. A* **102**, 6491-6497, (1998).
7. Menard, E., Nuzzo, R. G. & Rogers, J. A. Bendable single crystal silicon thin film transistors formed by printing on plastic substrates. *Appl. Phys. Lett.* **86**, 093507, (2005).
8. Karnik, R. *et al.* Electrostatic control of ions and molecules in nanofluidic transistors. *Nano Lett.* **5**, 943-948, (2005).
9. Lee, J., Panzer, M. J., He, Y., Lodge, T. P. & Frisbie, C. D. Ion gel gated polymer thin-film transistors. *J. Am. Chem. Soc.* **129**, 4532-4533, (2007).

10. Kalman, E. B., Vlassiuk, I. & Siwy, Z. S. Nanofluidic bipolar transistors. *Adv. Mater.* **20**, 293-297, (2008).
11. So, J.-H. *et al.* Reversibly Deformable and mechanically tunable fluidic antennas. *Adv. Funct. Mater.* **19**, 3632-3637, (2009).
12. Kubo, M. *et al.* Stretchable microfluidic radiofrequency antennas. *Adv. Mater.* **22**, 2749-2752, (2010).
13. S. Cheng, A. Rydberg, K. Hjort, Z. Wu, Liquid metal stretchable unbalanced loop antenna. *Appl. Phys. Lett.* **94**, 144103 (2009).
13. Mannsfeld, S. C. B. *et al.* Highly sensitive flexible pressure sensors with microstructured rubber dielectric layers. *Nat. Mater.* **9**, 859-864, (2010).
14. Pelrine, R., Kornbluh, R., Pei, Q. & Joseph, J. High-speed electrically actuated elastomers with strain greater than 100%. *Science* **287**, 836-839, (2000).
15. Ilievski, F., Mazzeo, A. D., Shepherd, R. F., Chen, X. & Whitesides, G. M. Soft robotics for chemists. *Angew. Chem. Int. Ed.* **50**, 1890-1895, (2011).
16. Nishide, H. & Oyaizu, K. Toward flexible batteries. *Science* **319**, 737-738, (2008).
17. Kaltenbrunner, M., Kettlgruber, G., Siket, C., Schwödiauer, R. & Bauer, S. Arrays of ultracompliant electrochemical dry gel cells for stretchable electronics. *Adv. Mater.* **22**, 2065-2067, (2010).
18. Yu, C., Masarapu, C., Rong, J., Wei, B. & Jiang, H. Stretchable supercapacitors based on buckled single-walled carbon-nanotube macrofilms. *Adv. Mater.* **21**, 4793-4797, (2009).
19. Hu, L. *et al.* Stretchable, porous, and conductive energy textiles. *Nano Lett.* **10**, 708-714, (2010).
20. Koo, H.-J., So, J.-H., Dickey, M. D. & Velev, O. D. Towards all-soft matter circuits: Prototypes of quasi-liquid devices with memristor characteristics. *Adv. Mater.* **23**, 3559-3564 (2011).
21. Koo, H.-J., Chang, S. T., Slocik, J. M., Naik, R. R. & Velev, O. D. Aqueous soft matter based photovoltaic devices. *J. Mater. Chem.* **21**, 72-79, (2011).
22. Lipomi, D. J., Tee, B. C. K., Vosgueritchian, M. & Bao, Z. Stretchable organic solar cells. *Adv. Mater.* **23**, 1771-1775, (2011).
23. Kawakami, H. Polymeric membrane materials for artificial organs. *J. Artif. Organs* **11**, 177-181-181, (2008).

24. Baughman, R. H. Playing nature's game with artificial muscles. *Science* **308**, 63-65, (2005).
25. Simon, D. T. *et al.* Organic electronics for precise delivery of neurotransmitters to modulate mammalian sensory function. *Nat. Mater.* **8**, 742-746, (2009).
26. Ghezzi, D. *et al.* A hybrid bioorganic interface for neuronal photoactivation. *Nat. Commun.* **2**, 166, (2011).
27. Du, K. *et al.* Self-assembled electrical contact to nanoparticles using metallic droplets. *Small* **5**, 1974-1977, (2009).
29. H.-J. Kim, C. Son, B. Ziaie, A multiaxial stretchable interconnect using liquid-alloy-filled elastomeric microchannels. *Appl. Phys. Lett.* **92**, 011904, (2008).
30. Kim, H.-J., Maleki, T., Wei, P., Ziaie, B. A biaxial stretchable interconnect with liquid-alloy-covered joints on elastomeric substrate. *J. Microelectromech. Syst.* **18**, 138, (2009).
31. Siegel, A. C., Shevkoplyas, S. S., Weibel, D. B., Bruzewicz, D. A., Martinez, A. W., Whitesides, G. M. Cofabrication of Electromagnets and Microfluidic Systems in Poly(dimethylsiloxane). *Angew. Chem. Int. Ed.* **45**, 6877, (2006).
32. Siegel, A. C., Bruzewicz, D. A., Weibel, D. B. & Whitesides, G. M. Microsolidics: Fabrication of three-dimensional metallic microstructures in poly(dimethylsiloxane). *Adv. Mater.* **19**, 727-733, (2007).
33. So, J.-H. & Dickey, M. D. Inherently aligned microfluidic electrodes composed of liquid metal. *Lab Chip* **11**, 905-911, (2011).
34. Siegel, A. C., Tang, S. K. Y., Nijhuis, C. A., Hashimoto, M., Phillips, S. T., Dickey, M. D., Whitesides, G. M. Cofabrication: A Strategy for building multicomponent microsystems. *Acc. Chem. Res.* **43**, 518, (2010).
35. Chiechi, R. C., Weiss, E. A., Dickey, M. D., Whitesides, G. M. Eutectic gallium-indium (EGaIn): A moldable liquid metal for electrical characterization of self-assembled monolayers (SAMs). *Angew. Chem. Int. Ed.* **47**, 142 (2008).
36. Khan, M. R., Hayes, G. J., So, J.-H., Lazzi, G., Dickey, M. D. A frequency shifting liquid metal antenna with pressure responsiveness. *Appl. Phys. Lett.* **99**, 013501, (2011).
37. Dickey, M. D., Chiechi, R. C., Larsen, R. J., Weiss, E. A., Weitz, D. A., Whitesides, G. M. Eutectic gallium-indium (EGaIn): A liquid metal alloy for the formation of stable structures in microchannels at room temperature. *Adv. Funct. Mater.* **208**, 18, 1097, (2008).

38. Regan, M. J., Tostmann, H., Pershan, P. S., Magnussen, O. M., DiMasi, E., Ocko, B. M., Deutsch, M. X-ray study of the oxidation of liquid-gallium surfaces. *Phys. Rev. B : Condens. Matter* **55**, 10786 (1997).
39. L. Young, *Anodic Oxide Films*, Academic Press, New York, **1961**.
40. Pourbaix, M. *Atlas of Electrochemical Equilibria in Aqueous Solutions - Gallium*. Vol. 16.1, National Association of Corrosion Engineers, 1974.
41. Bard, A. & Faulkner, L. *Electrochemical Methods: Fundamentals and Applications*. John Wiley & Sons, Inc., 2001.

Chapter 4

Aqueous soft matter based photovoltaic devices*

* Partially based on Koo, Chang, Slocik, Naik and Velev, *J. Mater. Chem.*, 2011, 21, 72

4.1. Introduction

Photovoltaic cells attract considerable attention as one of the promising solutions to energy generation with minimized environmental pollution. The conventional types of photovoltaic cells are classified into three groups: inorganic solar cells,^{1,2} organic photovoltaics (OPVs)³⁻⁵ and dye sensitized solar cells (DSSCs).⁶⁻⁸ In addition to the research improving the performance of these conventional types of solar cells, new photovoltaic systems are being actively developed. Biomimetic or biocompatible solar cells, inspired by “artificial leaves”, are one example of such new classes of photovoltaics. Photoactive bio-complexes, e.g., Chlorophyll and photosynthetic reaction center (Photosystem I and II), have been used for photosensitization of biomimetic solar cells prototypes. Lai *et al.* showed photocurrent generation by using Chlorophyll adsorbed on Au nanoparticle loaded photoelectrodes.⁹ Terasaki *et al.* and Ciesielski *et al.* reported a photoactive Au electrode functionalized with Photosystem I, a supramolecular enzyme involved in photosynthesis.^{10,11} The Photosystem I molecules have been immobilized by chemical or physical linker molecules and the photo-excited electrons in Photosystem I are transferred to the electrode via the molecular linker. Biocompatible materials, such as water,¹²⁻¹⁴ agarose gel¹⁵ or lipid membranes,¹⁶ have also been used as media for photovoltaic systems. For example, Murakami *et al.* reported water-based DSSCs with relatively high conversion efficiency by improving wettability of TiO₂ photoelectrode.¹³ Water could be a good alternative to the organic solvents used in photoelectrochemical cells that tend to be volatile and environmentally problematic. These new concepts of biomimetic photovoltaics could lower production cost and decrease their environmental footprint.

Another class of new systems is based on ionic photovoltaics. Most of the conventional photovoltaic systems operate on electronic current rather than ionic current. Even though much effort has been invested into the study on ionic currents, especially in electrochemical cells,^{8,17-19} there has been little research on photovoltaics operating on photosensitive ions. This is because photosensitive ions mobile in the bulk are less efficient in electron transfer to electrodes than ones chemically bound to electrode

surfaces. However, utilization of photosensitive ions in the bulk allows three-dimensional distribution of the photosensitizing sites, which are mostly limited to surfaces or interfaces in the conventional photovoltaic systems.²⁰ Moreover, the photosensitive ionic compounds might provide the electrolyte medium by self-dissociation. In a pioneering work, Malliaras and coworkers have reported photovoltaic response in ion rectifying junction.²¹ Two thin layers of oppositely charged photosensitive ions with mobile counter-ions are brought into contact. The diffusion of the counter-ions to the interface establishes built-in potential by which the HOMO-LUMO energy levels of two photosensitive ions are bent, leading to separation of the photogenerated electron-hole pairs and unidirectional current. This ionic junction device has established a new class of photovoltaic systems based on photosensitive ions in the bulk even if its photocurrent density has been low ($0.15 \mu\text{A}/\text{cm}^2$).

Here, we demonstrate soft matter photovoltaic cells on the basis of hydrogel infused with photosensitive ions. The hydrogel, which contains 98 wt. % of water, could serve as a biocompatible and environmentally benign matrix for the new photovoltaic system. The “quasi” liquid material provides a medium where the electrochemical reaction rate and the mobility of ions are similar to those in liquid. We proved the device-building capabilities of similar water based gels earlier by demonstrating new types of gel diodes operating on ionic conductance.^{22,23} In the present study, two photosensitive dye molecules, DAS⁻ and $[\text{Ru}(\text{bpy})_3]^{2+}$, were used as ionic dopants of the aqueous gel bulk media of photovoltaic cells. We investigated the provisional mechanism of operation of the photovoltaic system, which includes a synergistic action of two dye molecules in photocurrent generation. To make low-cost flexible devices, an ITO coated plastic substrate and Cu electrode were used as anode and cathode, respectively. The Cu electrode was coated with carbon nanotubes, graphite and carbon black, for improving output voltage and facilitating charge transfer. Finally, a biomimetic photovoltaic cell was demonstrated by using bio-derived photosensitive materials, e.g., Photosystem II and Chlorophyll, which are well compatible with the aqueous gel based devices.

4.2. Experimental Section

4.2.1. Materials and Device Fabrication

The structure of the hydrogel based photovoltaic cells (HGPV cells) is illustrated in Figure 4.1. The agarose gel matrix was prepared by the same process as in our previous publications.^{22,23} The gel contained 2 wt. % of agarose (biochemistry research grade, Acros Organics). Two ionic dyes were used as the photosensitive materials: 9,10-Dimethoxy-2-anthracenesulfonic acid sodium salt ($\text{DAS}^- \text{Na}^+$) and Tris(2,2'-bipyridine) dichlororuthenium(II) hexahydate ($[\text{Ru}(\text{bpy})_3]^{2+} (\text{Cl}^-)_2$) (Sigma Aldrich). Both dyes were dissolved in ethanol at a concentration of 5 mM. The solutions of the dyes were infused into the agarose gel layers followed by evaporation of the ethanol. The amounts of dyes were 2.5×10^{-8} mol (5 μL dye solution) per 0.009 cm^3 gel layer in each of the experiments unless mentioned otherwise. The active area of the dye-infused hydrogel is $\sim 0.2 \text{ cm}^2$ and the thickness of each gel layer is $\sim 450 \mu\text{m}$ in all devices measured. The dye-infused gel layers were sandwiched between the two electrodes. A fluorine-doped tin oxide glass (FTO glass, Pilkington) was used as the top transparent working electrode. The FTO glass was replaced with an indium tin oxide (ITO) coated (poly(ethylene terephthalate)) substrate (60 ohm/sq., Sheldahl) as a working electrode of a flexible device. A platinum electrode (Pt foil, Alfa Aesar) was used as a counter electrode in most of the experiments, but for low-cost devices, inexpensive Cu metal foil (3M) was used as counter electrode instead of Pt foil.

We tested multi-walled carbon nanotubes, carbon black (Cabot Corp.) and graphite (TIMCAL Ltd.) as modifiers of the Cu electrodes. The multi-walled carbon nanotubes were synthesized by a common chemical vapor deposition technique.²⁴ All of the carbon materials were dispersed in ethanol by sonication for 90 min and coated on the Cu electrode by drop-casting. The bio-derived photosensitive materials, Chlorophyll (A type) and Photosystem II, were extracted and provided by Air Force Research Laboratory. Photosystem II was extracted and isolated from fresh spinach using a modified protocol.²⁵ Deveined spinach was ground and washed twice in cold pH 7.4 buffer (50 mM potassium phosphate, 100 mM sucrose, and 200 mM sodium chloride).

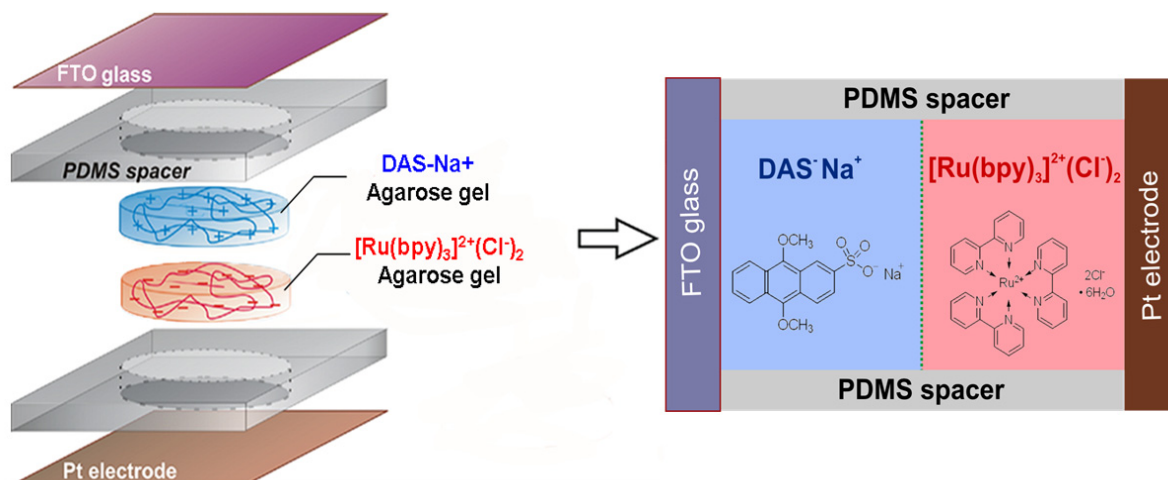


Figure 4.1. Schematic of the hydrogel photovoltaic cells (HGPVs). The dyes were originally infused into two different agarose gel layers as shown here, but over time the dyes became redistributed because of diffusion in the aqueous gel.

The extracted suspension was filtered and centrifuged at 12,300g for 25 min at 4°C. The pellet was gently resuspended in cold pH 7.4 buffer. The suspension was centrifuged again and the pellet was suspended in a pH 6.9 buffer (50 mM potassium phosphate, 300 mM sucrose, and 50 mM sodium chloride). While on ice, 20% (w/v) Triton X-100 was slowly added to the suspension with gentle stirring in the dark. Photosystem II was then purified on a sucrose gradient following the procedure of Kiley *et al.*²⁶ The separated Photosystem II was passed down a desalting column (Bio-rad Econo-Pac 10DG disposable column) to remove sucrose and concentrated using a microcon spin filter (Millipore, Ultracel YM-3). Chlorophyll was extracted by cold methanol from deveined freshly ground spinach leaves. The leaves were soaked in methanol for 1 hr in the dark and then separated from the insoluble material by filtering with #3 Whatman filter paper. The concentration of Chlorophyll was determined by measuring the absorbance at 663 nm. The prepared Photosystem II and Chlorophyll were dissolved in water and methanol, respectively. The concentration of Chlorophyll solution was 76.44 μM and that of Photosystem II was 367.6 μM . Both were infused into the agarose gel by the same method as the dyes. The infused volume of the solution was 10 μL (7.6×10^{-10} mol of

Chlorophyll and 3.6×10^{-9} mol of Photosystem II). The standard DSSC cells used for comparison in the mechanism studies were fabricated by following the process in the literature.²⁷ The photoelectrode consisted of bi-layers of synthesized anatase TiO₂ nanoparticles and large scattering particles. Ru[LL'-(NCS)₂](N-719, L = 2,2'-bipyridyl-4,4'-dicarboxylic acid, L' = 2,2'-bipyridyl-4,4'-ditetrabutylammoniumcarboxylate) was used as a dye.

4.2.2. Measurement of Photovoltaic Properties

The photocurrent response data as a function of time or bias voltage were collected by using a computer-controlled source meter (Keithley 2602, Keithley Instruments Inc.) under dark and illuminated conditions at room temperature. We used two different light sources: a fiber optic illuminator (~ 180 mW/cm², Fiber-Lite[®] High Intensity Illuminator series 180, Dolan-Jenner Industries, Inc.) for photocurrent measurement during bias sweep and a solar simulator with 300 W Xenon lamp (~ 88 mW/cm², Newport) for measurement of the photocurrent or photovoltage response as a function of time. The total intensities of the light sources were quantified using an optical power meter (model 1916-C, Newport) with thermophile detector (818P-001-12, Newport). The spectral intensity of the white light fiber optic illuminator was not verified.

4.3. Results and Discussion

4.3.1. Initial Evaluation of the Photovoltaic Properties

Typical current density-voltage (*J-V*) curves obtained from a prototype HGPV cell under dark and illuminated condition are shown in Figure 4.2(a). The device illuminated for 12 min exhibits short circuit current density $J_{sc} = 4.7$ μ A/cm², open circuit voltage $V_{oc} = 0.41$ V and fill factor $FF = 0.37$. The photovoltaic yield gradually increases with time. This delayed response is probably associated with the contribution of the dye ions in the bulk of the gel to the photocurrent generation. The ionic charge transport and the steady state current and voltage of photovoltaic HGPV cells are discussed in a later section. Even though the photocurrent generated by the HGPV cells is not comparable with that of the

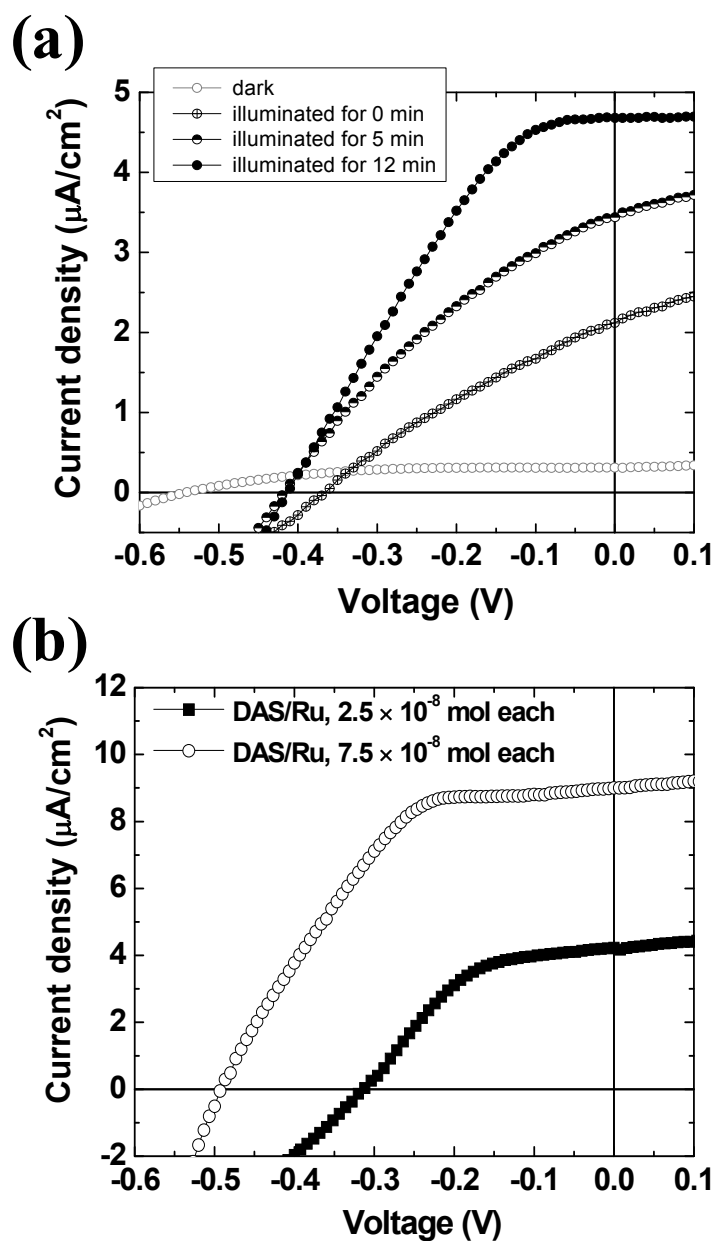


Figure 4.2. (a) Typical $J-V$ curves of gel photovoltaic cell prototypes under dark conditions and after illumination for increasing times. The bias was swept from -0.9 V to 0.1V at a rate of 14 mV/s. The light source was a fiber optic illuminator. (b) The effect of dye concentration on photovoltaic performance. When the dye concentration was increased 3 times (7.5×10^{-8} mol in each gel layer) than that of the prototype device (2.5×10^{-8} mol in each gel layer), both photovoltaic parameters, J_{sc} and V_{oc} , were improved by 125% and 67%, respectively. The bias was swept from -0.6 V to 0.1 V at a sweep rate of ~ 9.5 mV/s.

commercial Si-solar cells, the value is similar to or higher than those of other biomimetic or ionic photovoltaic systems reported recently.^{11,15,16,21} Moreover, the photovoltaic yield could be improved by increasing the dye concentration in the gel layers (Figure 4.2(b)). Our experiments indicate that the photovoltaic output is gradually saturated at dye amounts higher than 7.5×10^{-8} mol, which is presumably because above this concentration the ion transport through the gel and/or electrochemical reaction rate for dye regeneration are not rapid enough to utilize all dye molecules in the gel.

4.3.2. Provisional Mechanism of Photocurrent Generation of HGPVs

Two dye ions, DAS^- or $[\text{Ru}(\text{bpy})_3]^{2+}$, may generate photocurrent by providing photoinduced electrons or holes to either FTO or Pt electrode. We investigated the effect of the dye location in the gels as a means of elucidating the mechanism by which the photosensitive materials generate current in the HGPVs. The initial location of each dye can be confined by inserting a thin film of concentrated DAS^- or $[\text{Ru}(\text{bpy})_3]^{2+}$ at either FTO/undyed-gel or undyed-gel/Pt interface of the HGPV device. The thin films containing concentrated dyes were prepared by drying the water and trace solvents from dye-infused gel layers overnight under ambient conditions. When these dried films situated between the undyed-gel and the electrode are rehydrated, we obtain devices where the photosensitive molecules are (initially) present in a thin gel layer near the surface of either electrode, FTO or Pt. Their photocurrent responses in terms of the position of dyes are shown in Figure 4.3. Since the dyes slowly diffuse out of the concentrated subsurface layer facing the FTO or Pt into the bulk, the photocurrent at the early time stages results from the photosensitization of the dyes at the surface. Both dyes show higher photocurrent response on FTO/gel interface than on gel/Pt side, which means the dye molecules predominantly exchange ionic current at the FTO surface.²⁰ Another interesting result is the different trend of the photocurrent response of the dyes at late time stages. The photocurrent at the late stages represents the contribution of the dyes in the bulk of the gel because of the redistribution from dye diffusion. When the dry

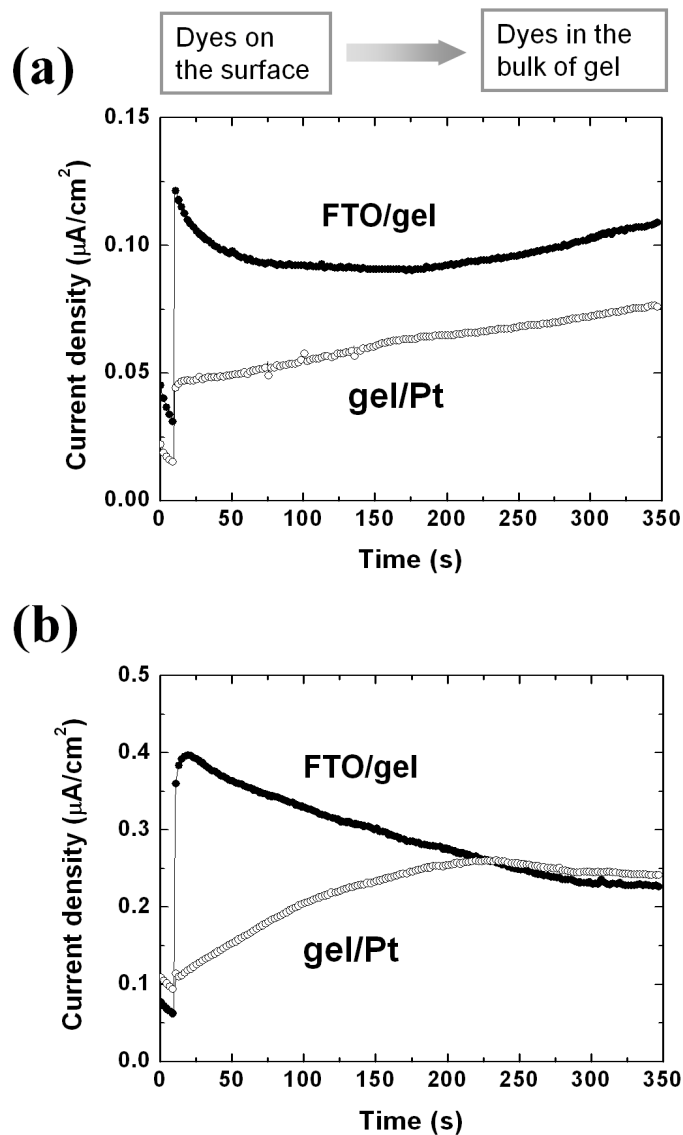


Figure 4.3. The photocurrent responses in terms of the original position of the dyes: (a) DAS^- and (b) $[\text{Ru}(\text{bpy})_3]^{2+}$. The light was turned on at time = 10 s. The currents level off as the diffusing dyes redistribute through the hydrogel.

gels containing either of the dyes are inserted at the FTO/gel interface, the photocurrent of the $[\text{Ru}(\text{bpy})_3]^{2+}$ dye continuously decreases, whereas that of the DAS^- dye gradually increases after 150 seconds (Figure 4.3). Our first hypothesis related to this result is that the DAS^- dye contributes to the photocurrent generation even when situated in the bulk. The excited DAS^- dye may have a long enough lifetime to diffuse to the electrode and

provide the electrons.²⁰ Another explanation for the late increase of the photocurrent by the DAS⁻ dye may be that the DAS⁻ dye plays an additional role in the photoharvesting process such as a reducing agent for the regeneration of the oxidized dyes.

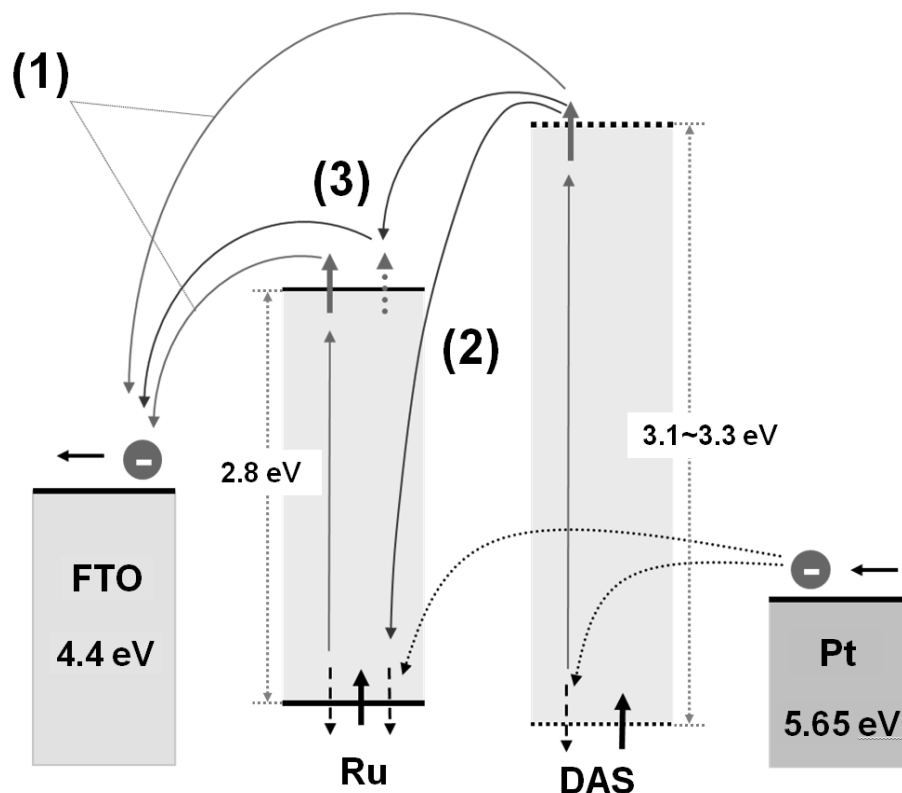


Figure 4.4. Provisional mechanism for the operation of the hydrogel based photovoltaic devices.

Based on the photocurrent responses in terms of the position of dyes, we formulated a provisional mechanism of device operation, which is presented in Figure 4.4. The relative energy levels of the two dyes are estimated based on the UV-vis absorption spectra (Figure 4.5). DAS⁻ has two absorption peaks at 380 nm (~3.3 eV) and 400 nm (~3.1 eV) and [Ru(bpy)₃]²⁺ has a peak at 450 nm (~2.8 eV). These data for the energy levels of [Ru(bpy)₃]²⁺ dye are similar to the ones reported in the literature.^{21,28} Little research has been conducted on the energy levels of the DAS⁻ dye. Even though the absolute energy levels of the DAS⁻ dye are not firmly established yet, it is expected that the energy gap between the HOMO and LUMO of the DAS⁻ is larger than that of the

$[\text{Ru}(\text{bpy})_3]^{2+}$ because of its shorter absorption wavelength. In the experiment on the effect of dye location, the dyes showed much higher photocurrent density at the FTO surface than the Pt surface. Both DAS^- and $[\text{Ru}(\text{bpy})_3]^{2+}$ dyes would generate photocurrent by absorbing light and directly injecting the excited electrons at the FTO surface (indicated by path (1) in Figure 4.4). Moreover, the DAS^- dye in the bulk of the gel probably contributes to the regeneration of the oxidized dye molecules by providing excited electrons (path (2) in Figure 4.4). The excited DAS^- dyes or the dye radicals may have relatively long lifetime, which enables the self-regeneration by the DAS^- dyes in the bulk.²⁰ The lower LUMO level of the $[\text{Ru}(\text{bpy})_3]^{2+}$ dye than the DAS^- dye might also facilitate the electron injection from the DAS^- dye at the FTO electrode surface (path (3) in Figure 4.4). The provisional mechanism suggests that the photosensitive ions work synergistically. Indeed, the HGPV devices with both DAS^- and $[\text{Ru}(\text{bpy})_3]^{2+}$ dyes showed photocurrent density nearly five times higher than those with either of the dyes alone (Figure 4.6). Studies on spectral responses of HGPV cells and HOMO-LUMO energy levels of a DAS^- dye are currently underway to verify the proposed provisional mechanism.

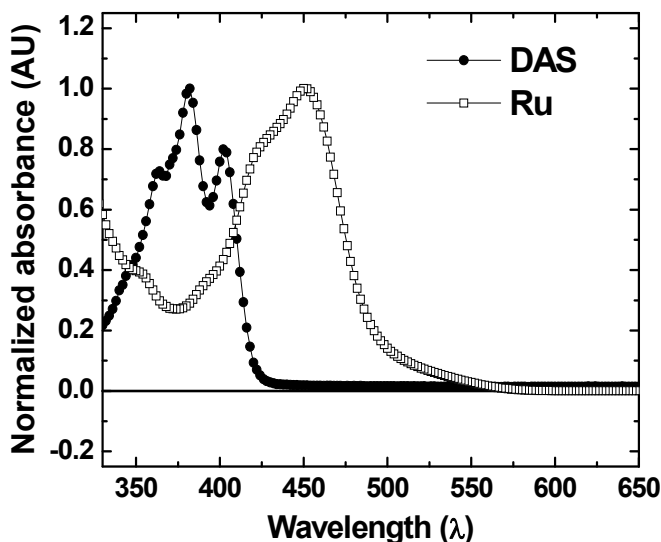


Figure 4.5. UV-Vis absorption spectra of DAS^- and $[\text{Ru}(\text{bpy})_3]^{2+}$ dyes. The energy gaps between the HOMO and LUMO of the DAS^- and the $[\text{Ru}(\text{bpy})_3]^{2+}$ dyes for the provisional mechanism were estimated from the wavelength values at the maximum peak position.

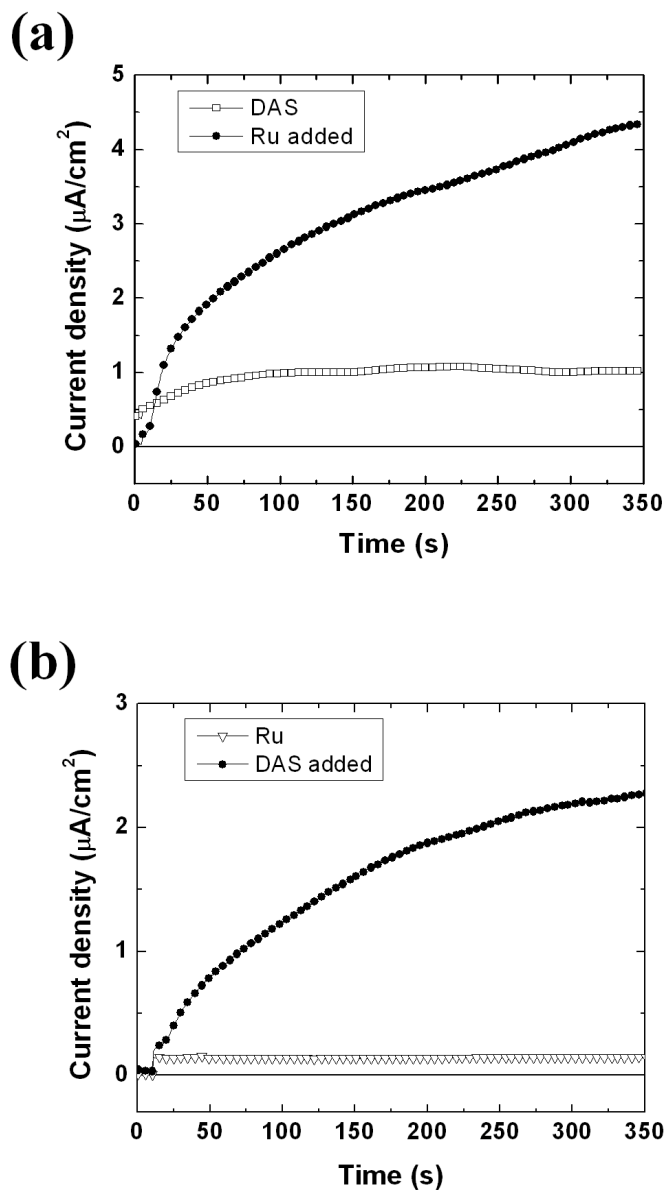


Figure 4.6. Photocurrent densities as a function of time and original dye location. (a) DAS⁻ was added to the device first, followed by [Ru(bpy)₃]²⁺ addition. (b) [Ru(bpy)₃]²⁺ was added to the device first, followed by DAS⁻. Both results show large increase of photocurrent densities when the other dye was introduced. The light was turned on at 10 seconds.

4.3.3. Ionic mechanism of HGPV operation

The principle difference in the mechanism of operation of the HGPV cells as compared to e.g., dye-sensitized solar cells (DSSCs) is revealed by the transient current response to

illumination. The slow current relaxation after external stimuli, such as bias or light, is a characteristic feature of devices operating on ionic transport in gels.^{22, 23} To investigate the transient HGPVs response, we compared the photocurrent responses of HGPV cells with responses of standard DSSC cells (Figure 4.7). All of the dye molecules in the DSSCs are adsorbed on the electrode surface, and not present in the bulk. When the light is turned on, the DSSC current immediately rises in response to the light, while the photocurrent in the HGPV cells gradually increases after an initial current jump over periods as long as minutes. The same difference in the transient features of the two systems is also exhibited after the light is turned off. The delayed current response of the HGPV cells presumably results from the low mobility of the DAS⁻ ions in the bulk. It takes time for the excited DAS⁻ ions in the bulk to affect the photovoltaic properties by performing either or both functions of “photocurrent generating” and “photoreducing” agent expected in our mechanism. The delayed saturation of the photocurrent response of the DAS⁻ dye is also observed in Figure 5 (a).

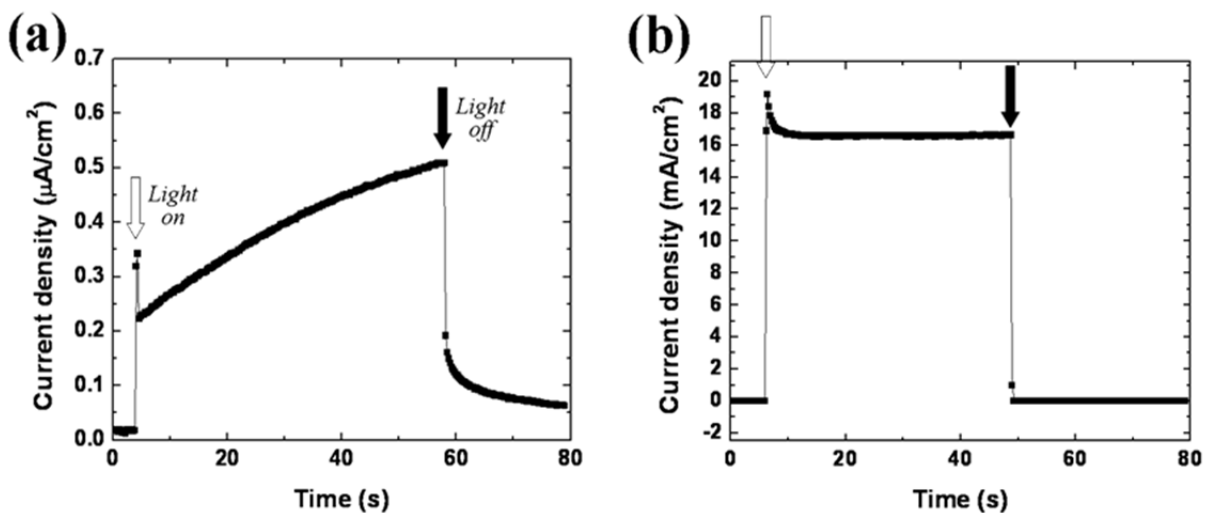


Figure 4.7. Photocurrent responses of (a) HGPVs and (b) DSSCs under dark and illumination conditions. White and black arrows represent the times when the light was turned on and off, respectively.

The bias sweep method, which is widely used for measurement of photovoltaic efficiency, might be imprecise in the new ion-based systems because the ionic equilibria are established slowly and the current could be affected by the rate of bias change during the measurement. To avoid the electrophoretic redistribution of the dye ions by the bias, photocurrent density and photovoltage of HGPVs were measured without application of external bias (short circuit) or external current (open circuit), respectively. Since the photovoltaic properties in HGPVs gradually increase, the current density and the voltage responses were recorded under continuous illumination until the values are saturated. As shown in Figure 4.8, J_{sc} and V_{oc} stabilized at $5.6 \mu\text{A}/\text{cm}^2$ and 0.4 V after 300~400 seconds. Such current relaxation times are comparable to the characteristic diffusion times of ionic species through gel layers of similar thickness. Compared to the saturated J_{sc} and V_{oc} values in Figure 4.8, the result obtained by the bias sweep method in Figure 4.2(a) ($J_{sc}= 4.7 \mu\text{A}/\text{cm}^2$ and $V_{oc}= 0.41 \text{ V}$) seems reasonable even though the current was underestimated by $\sim 20\%$. Thus, the bias sweep method may not be highly precise, but could be still used to evaluate the photovoltaic efficiency of our HGPV cells.

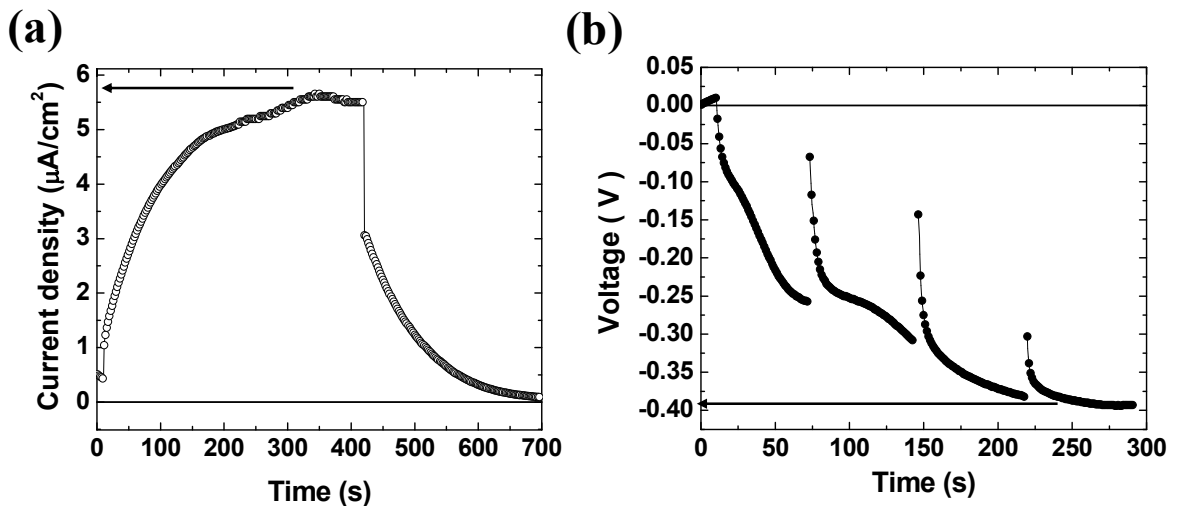


Figure 4.8. Examples of the transient characteristics of the photovoltaic properties of HGPVs: (a) photocurrent density at $V = 0 \text{ V}$ and (b) photovoltage at zero current. The arrows indicate the saturated values of J_{sc} and V_{oc} . The light intensity was $\sim 88 \text{ mW}/\text{cm}^2$. The photovoltage was recorded from four subsequent measurements under continuous illumination. The three spikes in (b) result from restarting the source meter and illustrate the slow establishment of the open circuit voltage. The light was turned on at 10 seconds for both measurement and was turned off at ~ 400 seconds for J_{sc} measurement.

4.3.4. Low-cost flexible HGPV devices with carbon coated copper counter electrode

The photoinduced voltage of our system depends on the energy gap between the Fermi level of the FTO glass and the work function of the counter electrode. The platinum work function of 5.65 eV is higher compared to other metals such as Ag (~4.6 eV), Al (~4.2 eV), Au (~5.3 eV), Cu (~4.7 eV). Due to its high work function, Pt turns out to be a suitable metal for the counter electrode of the HGPVs for generation of high output voltage. However, the high cost of the platinum (counter)electrodes would be a practical obstacle for the fabrication of low cost gel photovoltaic devices. To reduce the production cost, the platinum should be replaced with an inexpensive metal such as copper. This came out to be a nontrivial task. The photovoltaic performance of a device with pure copper counter electrode is compared to that with a platinum electrode in Figure 4.9(a). The V_{oc} of the device decreased by about 0.1 V and the current density decreased more than 2× when the platinum was replaced by a copper electrode presumably because of the low work function of copper. Another disadvantage of the copper is the instability of the metal surface. The oxide layer forming on the surface of copper could increase interfacial resistance between the gel and electrode surface. The reason that J_{sc} of the device with the copper counter electrode is lower than that of the device with the platinum one is probably associated with higher surface resistance of the copper metal.

We found an efficient solution overcoming the Cu metal electrode drawbacks by coating the copper surface with a layer of carbon material, such as carbon nanotubes, carbon black or graphite. The coating of carbon (work function: ~5 eV) may not only modify the work function of the copper counter electrode^{29, 30} but may also play the role of catalyst assisting the redox reaction between the dye molecules and the counter electrode.³¹ The catalytic effect of the carbon could decrease the interfacial resistance by assisting the redox reaction and facilitating charge transfer at the interface. The effect of coating of multi-walled carbon nanotubes on the gel photovoltaic device characteristics is shown in Figure 4.9(a). The device with the carbon nanotube coated copper counter electrode (J_{sc} = 3.6 $\mu\text{A}/\text{cm}^2$, V_{oc} = 0.49 V) exhibited better performance than that with the

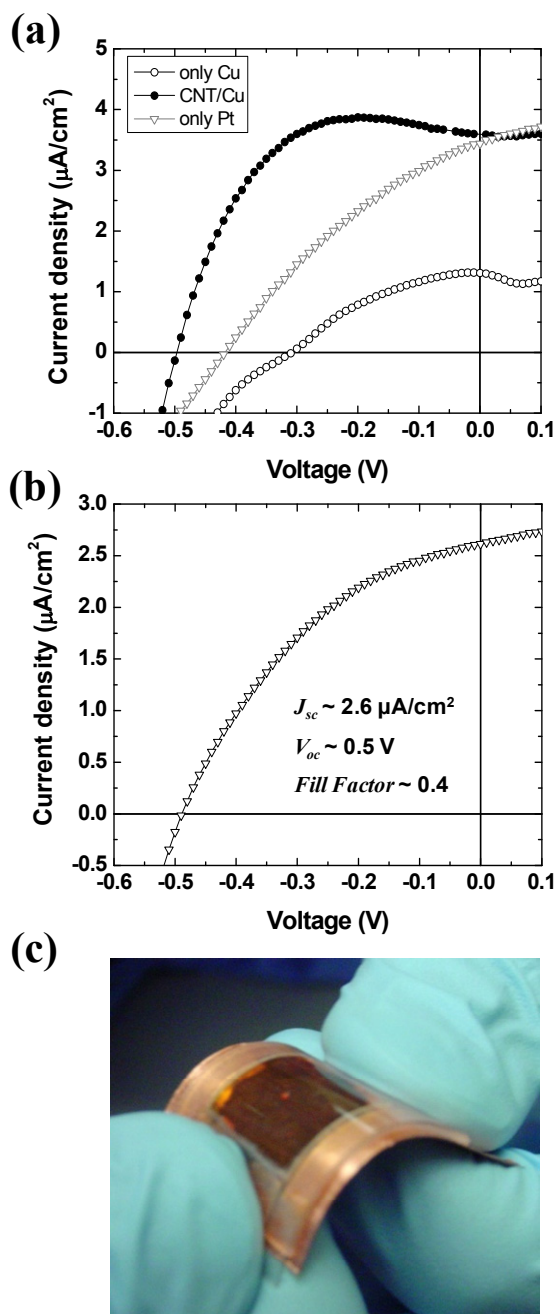


Figure 4.9. (a) Data comparison illustrating the effect of carbon nanotube coating on the photovoltaic performance compared to the one of uncoated Pt and Cu electrodes. The amount of the carbon nanotube coated on the Cu electrode was $\sim 0.03 \text{ mg}/\text{cm}^2$. (b) J - V characteristics of a prototype flexible HGPV cell, where the Cu foil coated with graphite/carbon black mixture was used as a counter electrode. (c) Photograph of the real prototype flexible device with an active area $\sim 125 \text{ mm}^2$. The light intensity was $\sim 180 \text{ mW}/\text{cm}^2$. All of the samples were characterized after illumination for 5 min.

naked copper electrode ($J_{sc}= 1.2 \mu\text{A}/\text{cm}^2$, $V_{oc}= 0.35 \text{ V}$). The photovoltage was improved by the modulation of the work function of copper by carbon coating. The increase of the photocurrent probably results from the catalytic effect of the carbon. The catalytic effect of the carbon could also contribute to the improvement of the photovoltage. The decrease of the charge-transfer resistance of the carbon-coated electrode could decrease the overvoltage loss on the counter electrode.³² The V_{oc} of the device with the carbon-coated copper electrode was higher even than that with normal platinum electrode that has higher work function than the carbon. This may be explained by the additional catalytic effect of the carbon. Even though carbon nanotubes were used in the experiment, it was later confirmed that other carbon materials, including carbon black and graphite, also showed effects similar to the carbon nanotubes. Thus, carbon coatings over Cu foil electrodes could reduce the production cost without loss of the photovoltaic efficiency.

The replacement of Pt with carbon-coated copper allowed making prototypes of a new generation of inexpensive, flexible solar cells. The bulk of these HGPV devices is aqueous soft matter, agarose gel, which is mechanically flexible. The FTO glass used in the early prototypes could be easily replaced with a conductive plastic substrate. We constructed a prototype of flexible and inexpensive photovoltaic cells by using an ITO coated poly(ethylene terephthalate) substrate and a Cu/Carbon (carbon black and graphite 1:1 mixture) counter electrode (Figure 4.9(b), (c)). These devices are made by a robust benchtop process, which involves mostly preparation of water-based agarose gels and is much simpler compared to the oxygen-less, ultra-clean environment that is needed to fabricate polymer solar cells. As described in the following section we could also replace the synthetic photosensitizers with biologically derived photoactive molecules.

4.3.5. Biomimetic photovoltaics with biologically derived dyes

The final goal of our work was to replace the artificial photosensitive molecules with light harvesting complexes of biological origin. The bio-complexes that we tested, such as Chlorophyll, Photosystem I and Photosystem II, are involved in photosynthesis, a

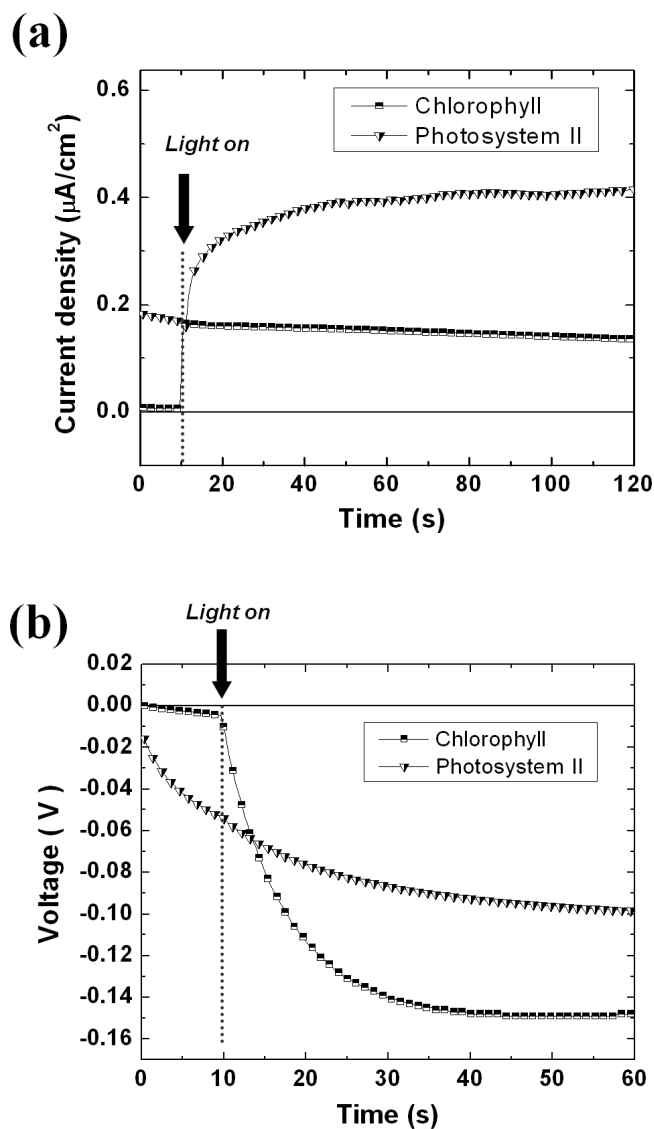


Figure 4.10. (a) Photocurrent densities and (b) photovoltage of gel-based cells operating on biological photosynthesizing complexes. The red arrows indicate the time when the light turned on.

“natural” solar energy conversion process. These bio-complexes are abundant in Nature, inexpensive and environmentally benign. Furthermore, the photoinduced charge separation in the bio-complexes is rapid and may exhibit high quantum efficiency.³³ The water-based hydrogel of the HGPVs offers a media that might be uniquely suitable as a host of these bio-complexes. We tested Chlorophyll and Photosystem II to prove that

water gel photovoltaic devices can be constructed on the basis of such biological photoactive molecules, which operate in an aqueous environment. Both bio-complexes generated comparable photocurrents of $0.2 \mu\text{A}/\text{cm}^2$, while the voltage developed by the Chlorophyll (0.16 V) was higher than the one of Photosystem II (0.07 V) (Figure 4.10). Even though the photovoltaic performance of these prototype devices was not high, the yield could be improved easily in the future as the amount of the biomolecules we used was very small (7.6×10^{-10} mol of Chlorophyll and 3.6×10^{-9} mol of Photosystem II) and the devices were only first prototypes without any optimization. Such bio-complexes could be key components in environmentally benign photovoltaics and the water based HGPVs could be a promising platform for new generations of biomolecule-based photovoltaic systems.

4.4. Conclusions

We present a new type of photovoltaic systems based on aqueous soft gel matrix. Two ionizable dyes, DAS⁻ and [Ru(bpy)₃]²⁺, were infused into the water-based gel as photosensitive materials. The photosensitive ions are mobile in the “quasi” liquid HGPVs media. The provisional mechanism of the operation of the HGPVs suggests that the dye ions cooperatively work and contribute to the photocurrent generating process both on the surface of the working electrode and in the bulk of the gel. The contribution of the mobile dye ions in the bulk of the gel to the photocurrent generation resulted in a long-term transient photocurrent response. The saturated J_{sc} and V_{oc} values were also measured without external bias or current to prevent the electrophoretic effect of the dye ions, confirming that the bias sweep method could be reasonably useful in such photovoltaic systems based on ionic currents. Overall, the photovoltaic performance of the HGPV prototypes was comparable to other biomimetic or ionic photovoltaic systems.

We demonstrated that carbon-coated Cu electrodes could replace the expensive Pt counter electrodes and reduce the production cost without loss of efficiency. Photocurrent was also present when biologically derived photoactive molecules, such as Chlorophyll and Photosystem II, were embedded in aqueous gel media. Even though the photocurrent

density of these devices is still low, there are many possible ways to improve the photocurrent generation. For example, working electrodes with rough surfaces provide larger area for the electron injection from the photosensitive ions.^{34, 35} Semiconducting materials³⁶⁻⁴¹ may be deposited on the electrode to improve the efficiency by radically decreasing the recombination at the photosensitive ions and the working electrode interfaces.²⁰ Another strategy for improvement of such water-based devices is the use of medium of higher ionic conductivity. This can be achieved by using polyelectrolyte-doped gels as we recently demonstrated in diodes interfacing such gels and silica nanofilms.²³ Further investigation of the precise operating mechanism of HGPV cells and improvement of performance of the biomimetic photovoltaic cells based on aqueous gel are in progress. Overall, solar cells based on such principles have the potential to be inexpensive, flexible, scalable and environmentally friendly.

4.5. Acknowledgements

This work was supported by grants from the Air Force Research Laboratory (F33615-03-D-5421, D0004) and DOE (08NT0001925). We thank Gregory Parsons and Jesse Jur for the helpful discussions.

4.6. References

1. Chapin, D. M., Fuller, C. S. & Pearson, G. L. A new silicon p-n junction photocell for converting solar radiation into electrical power. *J. Appl. Phys.* **25**, 676-677, (1954).
2. Chopra, K. L., Paulson, P. D. & Dutta, V. Thin-film solar cells: An overview. *Prog. Photovoltaics Res. Appl.* **12**, 69-92, (2004).
3. Wohrle, D. & Meissner, D. Organic solar-cells. *Adv. Mater.* **3**, 129-138, (1991).
4. H. Hoppe, N. S. S. Organic solar cells: An overview. *J. Mater. Res.* **19**, 1924, (2004).
5. Brabec, C. J., Sariciftci, N. S. & Hummelen, J. C. Plastic solar cells. *Adv. Funct. Mater.* **11**, 15-26, (2001).
6. O'Regan, B. & Grätzel, M. A low-cost, high-efficiency solar cell based on dye-sensitized colloidal TiO₂ films. *Nature* **353**, 737-740, (1991).

7. Grätzel, M. Photoelectrochemical cells. *Nature* **414**, 338-344, (2001).
8. Grätzel, M. Recent advances in sensitized mesoscopic solar cells. *Acc. Chem. Res.* **42**, 1788-1798, (2009).
9. Lai, W. H., Su, Y. H., Teoh, L. G. & Hon, M. H. Commercial and natural dyes as photosensitizers for a water-based dye-sensitized solar cell loaded with gold nanoparticles. *J. Photochem. Photobiol. A* **195**, 307-313, (2008).
10. Terasaki, N. *et al.* Plugging a molecular wire into photosystem I: Reconstitution of the photoelectric conversion system on a gold electrode. *Angew. Chem. Int. Ed.* **48**, 1585-1587, (2009).
11. Ciesielski, P. N. *et al.* Functionalized nanoporous gold leaf electrode films for the immobilization of photosystem I. *ACS Nano* **2**, 2465-2472, (2008).
12. Liska, P., Vlachopoulos, N., Nazeeruddin, M. K., Comte, P. & Grätzel, M. cis-Diaquabis(2,2'-bipyridyl-4,4'-dicarboxylate)ruthenium(II) sensitizes wide band gap oxide semiconductors very efficiently over a broad spectral range in the visible. *J. Am. Chem. Soc.* **110**, 3686-3687, (1988).
13. Murakami, T. N., Saito, H., Uegusa, S., Kawashima, N. & Miyasaka, T. Water-based dye-sensitized solar cells: Interfacial activation of TiO₂ mesopores in contact with aqueous electrolyte for efficiency development. *Chem. Lett.* **32**, 1154-1155, (2003).
14. Mikoshiba, S., Murai, S., Sumino, H. & Hayase, S. Another role of LiI/tert-butylpyridine in room-temperature molten salt electrolytes containing water for dye-sensitized solar cell. *Chem. Lett.* **31**, 1156-1157, (2002).
15. Matsui, J., Abe, K., Mitsuishi, M., Aoki, A. & Miyashita, T. Quasi-solid-state optical logic devices based on redox polymer nanosheet assembly. *Langmuir* **25**, 11061-11066, (2009).
16. Jiang, K., Xie, H. & Zhan, W. Photocurrent generation from Ru(bpy)₃²⁺ immobilized on phospholipid/alkanethiol hybrid bilayers. *Langmuir* **25**, 11129-11136, (2009).
17. Wang, P., Zakeeruddin, S. M., Comte, P., Exnar, I. & Grätzel, M. Gelation of ionic liquid-based electrolytes with silica nanoparticles for quasi-solid-state dye-sensitized solar cells. *J. Am. Chem. Soc.* **125**, 1166-1167, (2003).
18. Wang, P., Zakeeruddin, S. M., Exnar, I. & Grätzel, M. High efficiency dye-sensitized nanocrystalline solar cells based on ionic liquid polymer gel electrolyte. *Chem. Commun.*, 2972-2973, (2002).

19. Hara, K., Horiguchi, T., Kinoshita, T., Sayama, K. & Arakawa, H. Influence of electrolytes on the photovoltaic performance of organic dye-sensitized nanocrystalline TiO₂ solar cells. *Sol. Energy Mater. Sol. Cells* **70**, 151-161, (2001).
20. Memming, R. Photochemical and electrochemical processes of excited dyes at semiconductor and metal electrodes. *Photochem. Photobiol.* **16**, 325-333, (1972).
21. Bernards, D. A., Flores-Torres, S., Abruna, H. D. & Malliaras, G. G. Observation of electroluminescence and photovoltaic response in ionic junctions. *Science* **313**, 1416-1419, (2006).
22. Cayre, O. J., Chang, S. T. & Velev, O. D. Polyelectrolyte diode: Nonlinear current response of a junction between aqueous ionic gels. *J. Am. Chem. Soc.* **129**, 10801-10806, (2007).
23. Koo, H.-J., Chang, S. T. and Velev, O. D. Ion-current diode with aqueous gel/SiO₂ nanofilm interfaces. *Small*, **6**, 1393-1397, (2010).
24. Andrews, R., Jacques, D., Qian, D. & Rantell, T. Multiwall carbon nanotubes: Synthesis and application. *Acc. Chem. Res.* **35**, 1008-1017, (2002).
25. M. Seibert, I. Yruela & Picorel, R. *Photosynthesis Research Protocols*. Vol. 274 55-56 Humana Press, 2004.
26. Kiley, P. *et al.* Self-assembling peptide detergents stabilize isolated photosystem ion a dry surface for an extended time. *PLoS Biol.* **3**, e230, (2005).
27. Koo, H.-J., Park, J., Yoo, B., Yoo, K., Kim, K., and Park, N.-G. Size-dependent scattering efficiency in dye-sensitized solar cell. *Inorg. Chim. Acta*, **2008**, 361, 677-683.
28. Fiaccabrino, G. C., Koudelka-Hep, M., Hsueh, Y.-T., Collins, S. D. & Smith, R. L. Electrochemiluminescence of tris(2,2'-bipyridine)ruthenium in water at carbon microelectrodes. *Anal. Chem.* **70**, 4157-4161, (1998).
29. Ago, H., Petritsch, K., Shaffer, M. S. P., Windle, A. H. & Friend, R. H. Composites of carbon nanotubes and conjugated polymers for photovoltaic devices. *Adv. Mater.* **11**, 1281-1285, (1999).
30. Geng, J. X. & Zeng, T. Y. Influence of single-walled carbon nanotubes induced crystallinity enhancement and morphology change on polymer photovoltaic devices. *J. Am. Chem. Soc.* **128**, 16827-16833, (2006).
31. Kay, A. & Grätzel, M. Low cost photovoltaic modules based on dye sensitized nanocrystalline titanium dioxide and carbon powder. *Sol. Energy Mater. Sol. Cells* **44**, 99-117, (1996).

32. Wang, G. Q., Xing, W. & Zhuo, S. P. Application of mesoporous carbon to counter electrode for dye-sensitized solar cells. *J. Power Sources* **194**, 568-573, (2009).
33. Lee, J. W., Collins, R. T. & Greenbaum, E. Molecular ionic probes: A new class of hill reagents and their potential for nanofabrication and biometallo catalysis. *J. Phys. Chem. B* **102**, 2095-2100, (1998).
34. Bera, D., Patil, S., Scammon, K. & Seal, S. Diffusion-limited growth of FTO-nanofilm-coated tin fractals. *Electrochem. Solid-State Lett.* **8**, D31-D34, (2005).
35. Masuda, Y., Ohji, T. & Kato, K. Room-temperature synthesis of tin oxide nano-electrodes in aqueous solutions. *Thin Solid Films* **518**, 850-852, (2009).
36. Kim, D., Ghicov, A., Albu, S. P. & Schmuki, P. Bamboo-type TiO₂ nanotubes: Improved conversion efficiency in dye-sensitized solar cells. *J. Am. Chem. Soc.* **130**, 16454-16455, (2008).
37. Zupalova, M. *et al.* Organized mesoporous TiO₂ films exhibiting greatly enhanced performance in dye-sensitized solar cells. *Nano Lett.* **5**, 1789-1792, (2005).
38. Liu, J. *et al.* Novel dye-sensitized solar cell architecture using TiO₂-coated vertically aligned carbon nanofiber arrays. *ACS Appl. Mater. Interfaces* **1**, 1645-1649, (2009).
39. Ravirajan, P. *et al.* Hybrid polymer/zinc oxide photovoltaic devices with vertically oriented ZnO nanorods and an amphiphilic molecular interface layer. *J. Phys. Chem. B* **110**, 7635-7639, (2006).
40. Xu, L., Chen, Q. & Xu, D. Hierarchical ZnO nanostructures obtained by electrodeposition. *J. Phys. Chem. C* **111**, 11560-11565, (2007).
41. Martinson, A. B. F., Elam, J. W., Hupp, J. T. & Pellin, M. J. ZnO nanotube based dye-sensitized solar cells. *Nano Lett.* **7**, 2183-2187, (2007).

Chapter 5

Photocatalytic Hydrogel Reactor with a Microfluidic Network Mimicking Plant Leaves*

* Partially based on Koo and Velev, submitted.

5.1. Introduction

Light-driven flow reactors with immobilized photocatalysts are promising for water disinfection and purification as well as solar fuel generation.¹⁻⁴ Systems where the catalytic particles are deposited on a reactor wall^{5,6} or a supporting substrate⁷ have advantages compared to reactors where the catalysts are suspended in the liquid medium because the separation of the catalyst after the water treatment is not required. The conversion efficiency of such reactors with immobilized catalysts could be improved by scaling down their dimensions, thereby increasing the ratio of the surface area of the catalyst film to the volume of reactant solutions. One way to achieve this is to use microfluidic reactor with planar films of TiO₂ particles on both sides of the wall.⁵ However, in a catalyst film based reactor, the mass transfer of reactants into the pores of the densely packed catalyst film becomes a major limiting step of the photocatalytic processing.

The biomimetic reactor reported here is broadly inspired by the materials composition and structure of natural leaves. A leaf is in effect a natural photoreactor with microfluidic channels. The water and minerals are uniformly distributed via its venation network. The leaf tissue is a porous hydrated soft matter where mesophyll cells, the photoreacting centers in a leaf, are distributed three-dimensionally, resulting in high surface area to volume ratio and low mass transfer resistance. Biomimetic devices inspired by the materials and the structure of natural leaves have been reported in fundamental microfluidics studies⁸⁻¹¹ and prototypes of energy harvesting systems.¹²⁻¹⁴ We introduce here a new class of biomimetic photocatalytic reactors with microfluidic network based on aqueous soft matter. The matrix of the devices is an agarose gel, which contains 98 wt.% of water and 2 wt.% of agarose, biopolymer derived from natural seaweed. TiO₂ particles are uniformly distributed throughout the gel matrix. Due to high porosity, the agarose gel medium allows for uniform permeation of the liquid and enhances the reagent mass transfer to the solid catalysts.¹⁵ Microfluidic channels forming a simple branched venation network are embossed in the gel. To demonstrate the photocatalytic activity of the gel-microfluidic reactor, we inject

solutions containing two different dyes into a prototype device, and then illuminate it with UV light. The dye distribution pattern in the devices is compared to the results of a comprehensive numerical simulation. Quantitative analysis of the quantum yield of the prototype device allows estimating the efficiency of these new microfluidic reactors.

5.2. Experimental Section

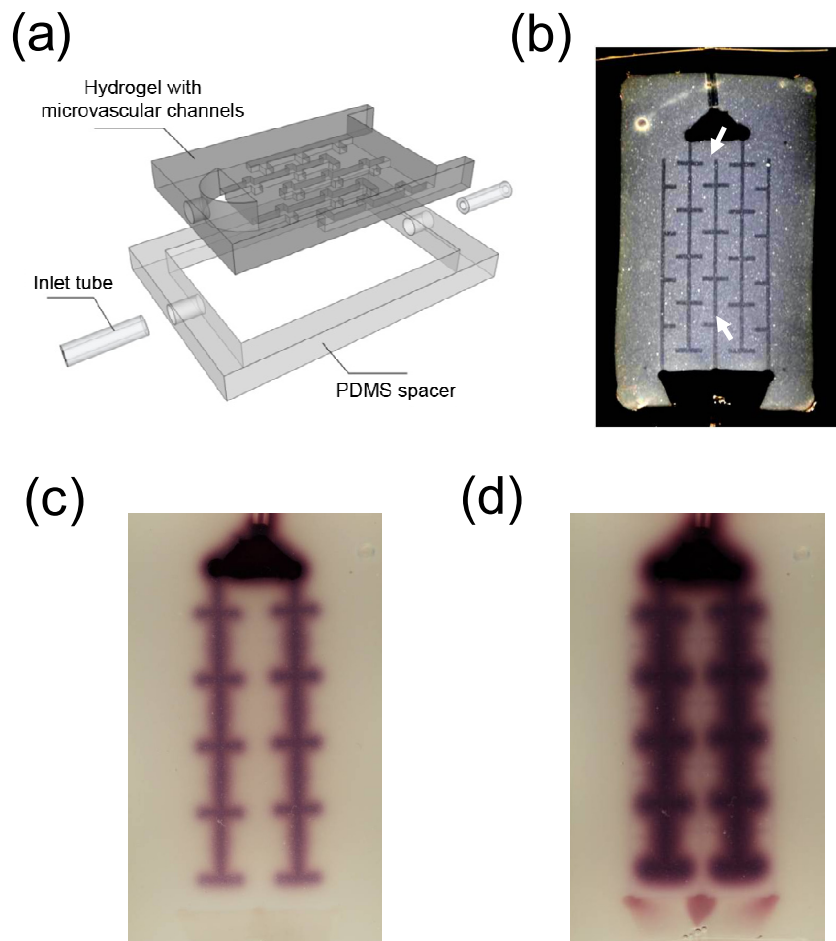


Figure 5.1. (a) Schematics of the light-driven microvascular gel reactor. The TiO₂-embedded hydrogel with the branched channel network was enclosed in a PDMS spacer and sandwiched by two glass substrates. Two pieces of Tygon tubing were inserted into the inlet and outlet of the device for supply of a reactant and drainage of the processed solution. (b) Photograph of the TiO₂-embedded gel with the microfluidic network. The white arrows point to examples of larger TiO₂ particle aggregates inside the hydrogel medium. The TiO₂ composition was lowered to 0.5 wt.% in this gel for clear observation of the particles. Top view images of the microfluidic gel reactor after the injection of a solution of 1 mM Allura Red and 1 mM Methylene Blue dyes for (c) 30 min and (d) 60 min.

The prototype photoreactor with a microfluidic channel network was fabricated as shown in Figure 5.1(a). Hydrogel with embedded TiO₂ (TiO₂-hydrogel) was prepared similarly to the heat-set agarose gel described previously.¹⁶ Aqueous suspension of TiO₂ particles was mixed into a solution of agarose (Acros Organics) and was heated in a microwave oven, followed by gelation by cooling. The concentrations of the TiO₂ particles and the agarose in the resulting gel were 1 wt.% and 2wt.%, respectively. Two interdigitated channel networks were formed in hydrogel by replica molding. The hot liquefied TiO₂-agarose mixture was poured on a patterned SU-8 mold and was cooled down to room temperature. The TiO₂-hydrogel with the channels in the resulting device is shown in Figure 5.1(b). The scanning electron microscope (SEM) images of dried TiO₂-hydrogel provided in Figure 5.2 show that the embedded TiO₂ aggregates are uniformly dispersed in the agarose matrix. We did not observe visible traces of TiO₂ particles in the outgoing flow during the injection of the reagent solution. The size of the TiO₂ particles was estimated by dynamic light scattering spectroscopy (Zetasizer Nano, Malvern Instruments Ltd). The average diameter of the TiO₂ aggregates was ~ 330 nm, which is probably large enough to keep them entrapped in the pores of the agarose gel of ~ 100 nm.¹⁷

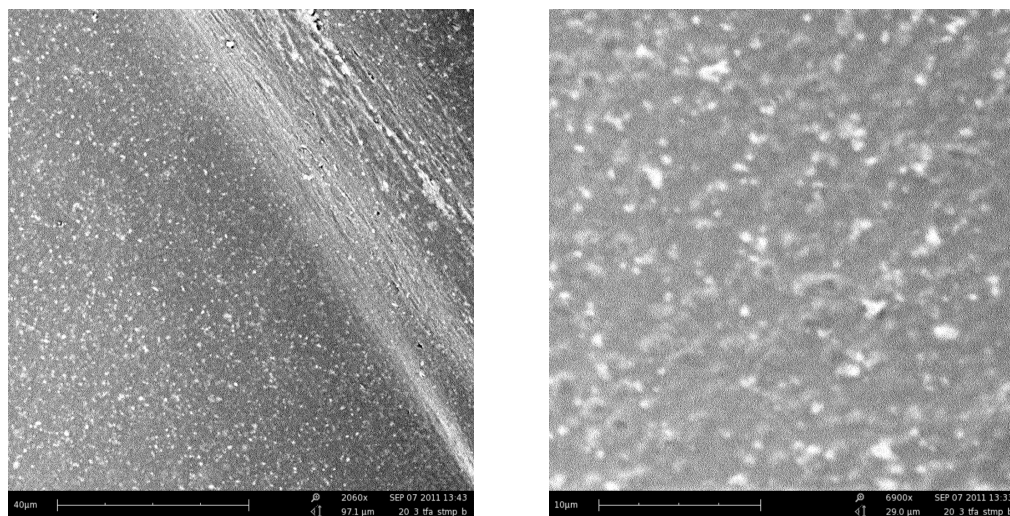


Figure 5.2. SEM images of the dried agarose gel with the embedded TiO₂ particles. Note that the sub-micron clusters of the TiO₂ catalyst are uniformly dispersed throughout the gel matrix.

5.3. Results and Discussion

5.3.1. Transport of Injected Dye in a Hydrogel Reactor with Embedded Microfluidic Channels

Since the hydrogel medium of the light-driven microfluidic reactor is highly fluid-permeable,¹⁷ the injected solution penetrates the gel through the porous walls of the microfluidic channels. This permeation is a characteristic feature of our microfluidic device made of hydrogel rather than the conventional, non-permeable materials such as silicon, glass and poly(dimethylsiloxane). The branched channel network is designed to broadly mimic the veins of plant leaves. By imaging the color intensity of the dyes injected into the microfluidic device, we visualize the flows along the branched channels, followed by permeation through the porous gel between the interdigitated channels (Figure 5.1(c), (d)).

5.3.2. Simulation for Solute Transport in Hydrogel Microfluidic Devices

To confirm the mechanism and quantify the complex flow of the dye in solution seeping through the channels and the gel, we also simulated the reagent transport through the devices using COMSOL Multiphysics package (COMSOL Inc., Burlington, MA). The computational model takes into account two transport phenomena: the fluid transport in the microfluidic channel network and the convective diffusion of the reagent through the porous hydrogel. The time-dependent distribution profiles of reagent concentration in the top-viewed device (2D geometry) were calculated by using the common equation.

$$\frac{\delta c}{\delta t} = -v\nabla c + D\nabla \bullet \nabla c$$

where c is the concentration of reagent, D is the diffusion coefficient of the reagent (1×10^{-10} m²/s, which of the order of magnitude of the values for large dye molecules in the literature¹⁸ and v is the velocity of fluid. The velocity of fluid through the porous media and in the nonporous media was obtained from the preceding simulation by using the Brinkman equation and the Navier-Stokes equations for incompressible fluid

$$\frac{\eta}{k} \vec{v} = \nabla \cdot \left\{ -\vec{p} + \frac{\eta}{\varepsilon_p} (\nabla \vec{v} + (\nabla \vec{v})^T) \right\} \quad (\text{in porous media})$$

$$\rho \vec{v} \cdot \nabla \vec{v} = \nabla \cdot \left\{ -\vec{p} + \eta (\nabla \vec{v} + (\nabla \vec{v})^T) \right\} \quad (\text{in nonporous media})$$

$$\nabla \cdot \vec{v} = 0 \quad (\text{in all media})$$

where η is the viscosity of the solutions (1×10^{-3} Pa·s), ρ is the density of the solvent (1×10^3 kg/m³ for water), k is the permeability of the agarose gel (5.93×10^{-16} m²)¹⁹ and ε_p is the porosity of the gel (0.98). The volume fraction of the agarose in the hydrated gel is almost the same as its mass fraction.²⁰ The inlet boundary conditions are a constant pressure of 2×10^3 Pa and a concentration of 0.4 mol/m³. The outlet boundary conditions are zero pressure and conserved convective flux.

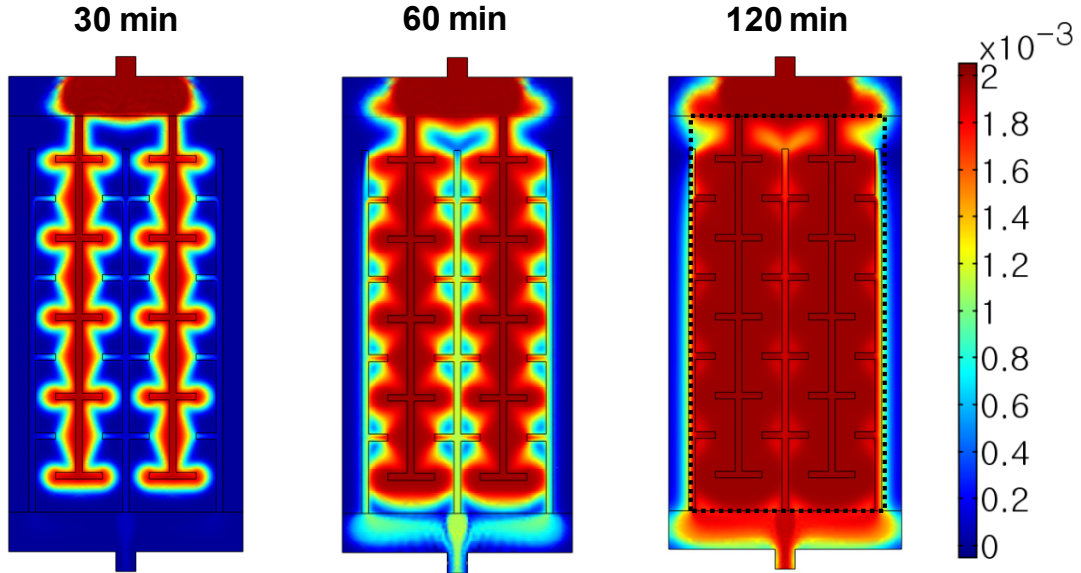


Figure 5.3. Simulation result for the dye penetration through the gel-microvascular network after dye injection for 30, 60 and 120 min. The rectangle with dotted lines in the image for 120 min indicates the “reaction area” through which most of the dye solution flows under illumination.

The simulations for the concentration distribution of the reagent show that the pattern of reagent solution permeation through the porous gel matrix after flowing along the branched channels (Figure 5.3). The simulation result was compared to the experimental dye

distribution at the same operating conditions to prove the validity of the model. The concentration profiles after the injection of the reagent solution for 30 min and 60 min obtained by experiment and simulation are in a good agreement (Figure 5.1(c), (d) and Figure 5.3). The results confirm the permeation mechanism by which the reagent solution can be uniformly supplied by the channels with the bio-inspired branched design and the porous matrix of the gel reactor. This experimentally and computationally confirmed uniform delivery of the reagent in the gel device should ensure that all TiO_2 particles in the hydrogel are active in the photocatalytic conversion. Moreover, the established simulation procedure can be used to design and optimize further generations of microfluidic photoreactors. Further numerical analysis of the reagent transport is now under way to optimize the channel design for more rapid and efficient supply of the reagent.

5.3.3. Photocatalytic Reaction of Injected Dyes in the Microfluidic Hydrogel Reactor

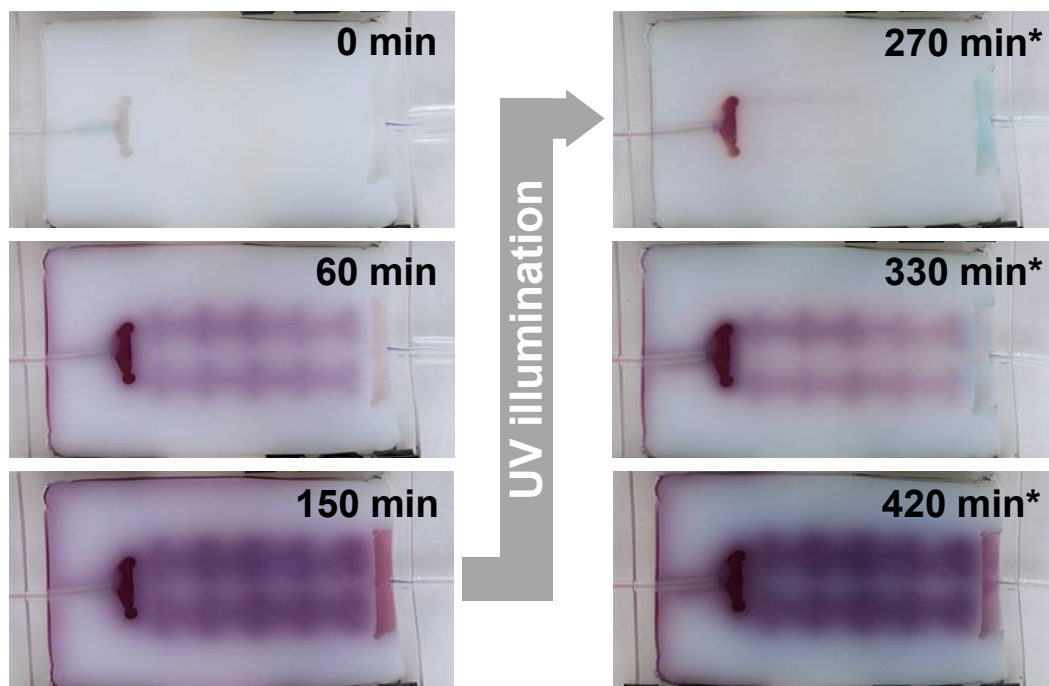


Figure 5.4. Temporal distribution of the dye mixture solution (0.2 mM Methylene Blue and 0.2 mM Allura Red) as a function of time. The UV illumination started 220 min after the dye injection and continued for 50 min. The flow pattern of the partially degraded dye under the UV light for 3 min is shown in Figure 5.5. Asterisks (*) denote images taken during the post-illumination recovery.

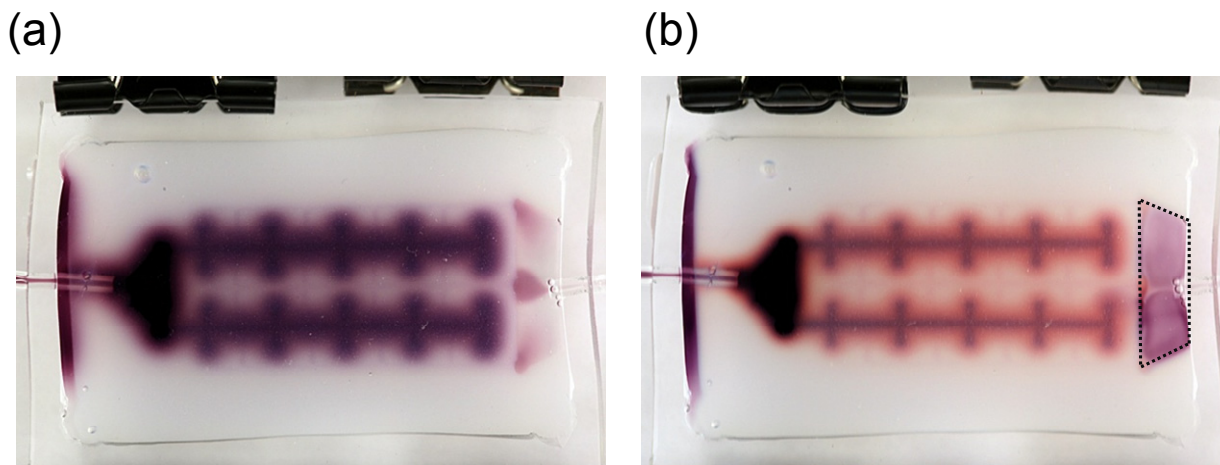


Figure 5.5. Partial degradation of the Methylene Blue and Allura Red dye in the light-driven gel reactor (a) before and (b) after UV illumination for 3 min. The dye solutions were continuously supplied during the UV illumination. The concentration of both dyes in the mixed solution is 1 mM. The area surrounded by the dotted line is a non-reactive region, where the photocatalytic reaction does not take place because of the absence of TiO₂ catalyst.

To characterize the operation of the light-driven microfluidic gel reactor, we injected a dye solution into a prototype device and applied UV light illumination after the hydrogel was infused with the reagents. Two different dyes, Methylene Blue and Allura Red, were used to confirm that the degradation reaction in the TiO₂-hydrogel reactor is not limited to a specific compound. Both dyes are photo-catalytically degradable in the presence of TiO₂ particles and UV light.^{21,22} The injection flow rate of the dye solution was 5 μ l/min. After solution injection for 220 min, the device was illuminated from the top with UV light (wavelength 320–390 nm, SunRay 400 SM, Uvitron International, Inc.) to trigger the photocatalytic reaction by the TiO₂ catalyst particles embedded in the hydrogel. The dye solution was continuously supplied at the same constant rate. The patterns of time-dependent infusion of the dye into the gel followed by optical imaging are shown in Figure 5.4. The dyes in the device became predominantly decolorized within 5 minutes of illumination and completely bleached within 40 min. The light-driven degradation stopped when the UV illumination was turned off and the colored flow pattern reappeared as the colorants supplied by the continuing flow permeated the devices. Since organic dyes are commonly light-sensitive, their degradation might occur even without the TiO₂ catalyst. To prove that the TiO₂ catalyst

particles are essential for the reaction, we compared the degradation rate of the dye solution with and without TiO_2 particles under UV illumination (Figure 5.6). The violet color of the dye solution with dispersed TiO_2 particles disappeared completely under UV illumination for 30 min, while that of the dye solution without TiO_2 barely changed. The UV-vis spectra at different UV illumination times show that the dye photodegradation in the cell is enabled only in the presence of TiO_2 catalyst.

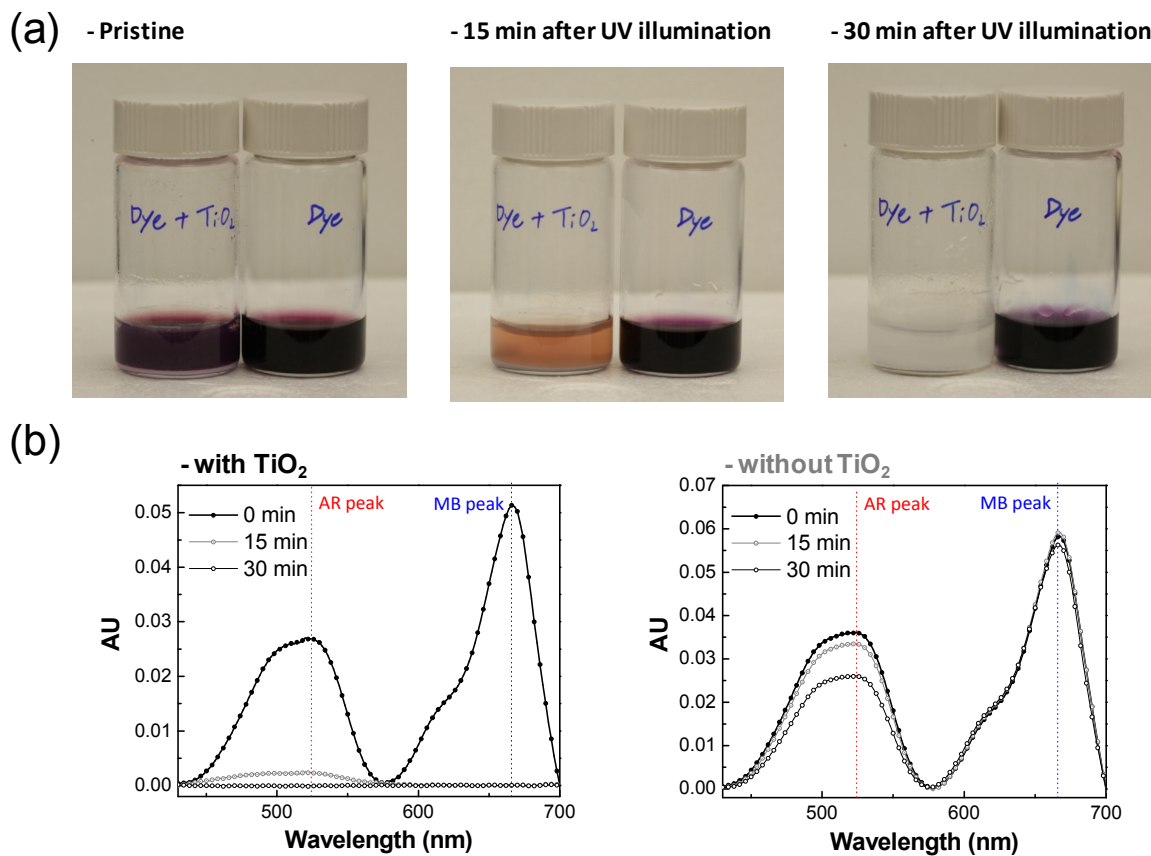


Figure 5.6. (a) Effect of the presence of TiO_2 particles on the color change of the solution of Allura Red and Methylene Blue dye mixture under UV illumination. (b) UV-vis absorption spectra of the dye solutions in (a). The absorbance of both dyes with TiO_2 catalysts drastically decreases under UV illumination. Thus, TiO_2 particles facilitate the degradation of the dyes even though a slight degradation of the Allura Red in the dye solution without TiO_2 catalyst was observed. The Allura Red dye may be more susceptible to UV degradation.

5.3.4. Quantitative Analysis of Infusion and Photocatalytic Degradation Rate

The quantitative analysis of the rate of infusion and photodegradation in the gel reactor, based on the concentration of dyes measured by UV-vis absorbance of the outflow solution exiting the device, is presented in Figure 5.7. The absorbance begins to increase at 50 min, corresponding to the time required for the injected dye to pass through the gel and to reach the outlet. This value is also in agreement with the simulation. The absorption peaks keep increasing with time due to the continuous dye influx until the UV light is turned on at 220 min. After the illumination commences, the UV-vis absorption of both dyes decreases

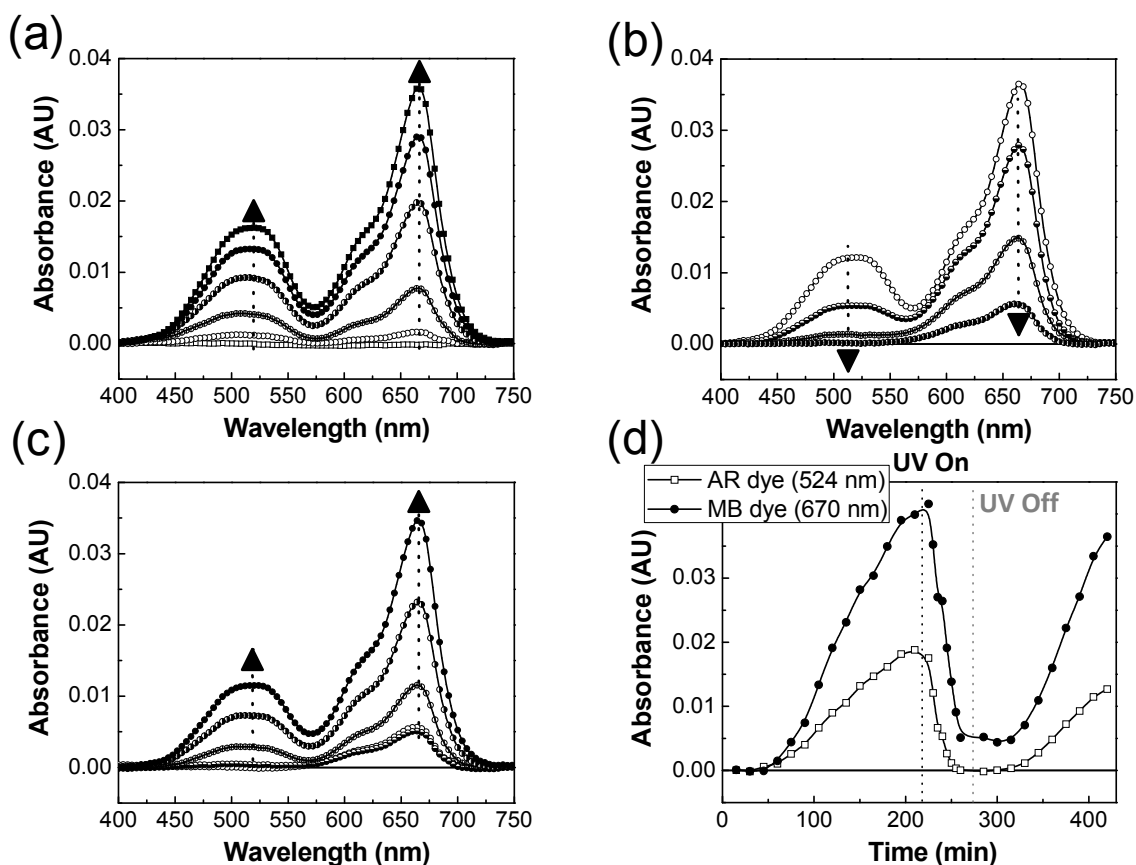


Figure 5.7. UV-vis absorption spectra of the dye solution exiting the light-driven gel reactor (a) before, (b) during and (c) after UV illumination. The time interval between the spectra collection is 30 min for (a) and (c) and 10 min for (b). (d) The absorbance peak intensity of the solution exiting the light-driven gel reactor as a function of time. The intensity was measured at 524 nm and 670 nm, which are the maximum absorption wavelengths of Allura Red and Methylene Blue in water, respectively.

because of the photocatalytic degradation. The peak intensity of the dye absorbance in Figure 5.7(d) began decreasing right after the start of UV illumination, indicating that the photocatalytic reaction was immediately triggered by the light. In ~ 35 min, the absorbance of the Methylene Blue at the exit decreased to less than 20% under the UV illumination. However, the photocatalytic reaction rate in the device is probably higher than the one measured by the decoloration, when we consider the non-reactive volume of the chamber in front of the outlet tube (Figure 5.5(b)), where the degraded dye solution is mixed with the pristine dye solution contained there before UV illumination. After the UV exposure is stopped at 270 min, the absorbance of the outflow solution increases in ~ 50 min, which is the same as the pass-through time lag when the dye was first injected before UV illumination.

5.3.5. Calculation of Quantum Efficiency

The reaction rate constant in a reactor with heterogeneous catalysts is limited by the mass transfer of reagents to the catalyst surfaces.⁷ Since the TiO_2 catalyst particles are three-dimensionally dispersed in the highly porous gel medium (porosity ≈ 0.98), the TiO_2 -hydrogel reactor could improve the mass transfer uniformity and maximize the fraction of reagents reaching the catalyst surface, thereby achieving higher conversion efficiency than the previous two-dimensional TiO_2 film based systems.^{5,6} To evaluate the quantum efficiency of our prototype photoreactor, we calculated the degradation rate of the dye molecules on the basis of the concentrations of the solutions exiting the reactor in dark and illuminated conditions. We injected a Methylene Blue dye solution (5 mM) into the gel reactor, which was illuminated with a solar simulator (100 mW/cm^2 , AM 1.5G, Newport 91160, 300 W Xenon lamp). The number of the degraded molecules was calculated from the difference of the UV-vis absorbance intensity of the solutions exiting the TiO_2 -hydrogel reactor between in dark and under illumination. We continuously injected a solution of 5 mM Methylene Blue dye into the gel reactor, which was illuminated with a solar simulator. The position of the absorbance peak intensity of the Methylene Blue coming out of the gel reactor is shown in Figure 5.8(a). The peak intensity decreases with the light illumination starting at 145 min due to photocatalytic degradation. The absorbance peak intensity is stabilized after 300 min,

when a “pseudo-steady state” is established. When the illumination stops at 330 min, the absorbance peak intensity increases again because of the termination of the photocatalytic reaction. The rate of the photocatalytic degradation of the dye molecules in the TiO₂-hydrogel reactor can be calculated by the expression

$$\text{Rate of the photocatalytic degradation of the dye} = \text{Rate of the supply of the dye} \times \frac{A_d}{A_0}$$

where A_0 is the UV-vis absorbance of the pristine stock dye solution and A_d is the difference between the absorbance of the UV-degraded dye solutions and the non-degraded dye solutions under pseudo-steady state, as shown in Figure 5.8(b). A_0 and A_d were 0.786 and 0.111, respectively. Since the rate of the supply of the Methylene Blue dye molecules at 10 $\mu\text{L}/\text{min}$ injection rate is 5.02×10^{14} molecules/s, the evaluated rate of the dye degradation in the gel reactor is 7.09×10^{13} molecules/s. Since the flux of the activating photons (with $\lambda \leq 387.5$ nm) in the incident light of the solar simulator can be estimated at 2.85×10^{16} photons/s,^{5,23} the apparent quantum efficiency of the device is $\sim 0.25\%$, which is comparable to the one of the recently reported alternative microfluidic reactor based on TiO₂ film.⁵ This quantum efficiency, however, is achieved with much smaller amount of the TiO₂ catalyst in the prototype hydrogel reactor. The amount of TiO₂ within the active volume of the hydrogel is 0.2 mg,²⁴ which is ~ 10 times less than that used in the earlier film microreactor.⁵ Thus, the gel reactor exhibits improved quantum efficiency per mass of catalyst due to the enhanced mass transfer of the dye reagents from the bulk fluid to the surface of the dispersed TiO₂ catalysts. Moreover, the efficiency achieved under a relatively slow flow rate of 10 $\mu\text{L}/\text{min}$ may, in principle, be enhanced in higher flow rate due to the decreased mass transfer resistance.⁵ The efficiency could be improved further by optimizing the amount of the catalyst, the uniformity of catalyst dispersion in the gel matrix and the flow rate of the reagent solution.

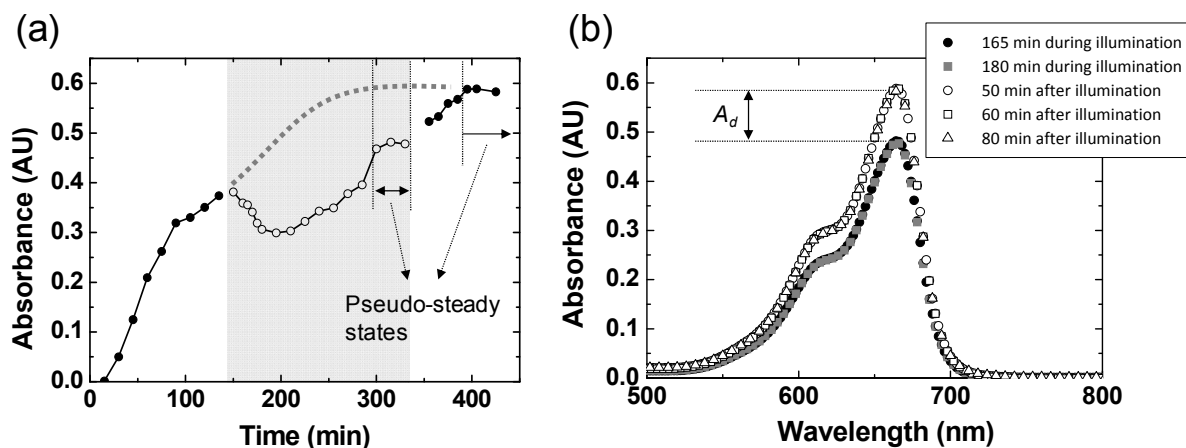


Figure 5.8. UV-vis absorbance of the solution exiting the TiO₂-hydrogel reactor as a function of (a) time and (b) UV-vis spectra at the “Pseudo-steady states”. The device was illuminated from 145 min to 330 min indicated by the red-colored box. The light was incident from the channel side of the microfluidic device. The collected solution was diluted before UV-vis absorption measurement at 640 nm. It was confirmed that the absorbance intensity is linearly proportional to the concentration of the dye solution in the concentration regime used for the measurement.

5.4. Conclusions

In summary, we present the principle of operation of a class of biomimetic photocatalytic reactors with microfluidic channel networks. The interdigitated channels with simple branched structure are embedded in a hydrogel, where photocatalytic TiO₂ particles are uniformly dispersed. The experiment and simulation of dye transport confirm that the microchannel-hosting gel enables uniform supply of the reagent throughout the matrix. Quantitative analysis of the photocatalytic degradation of the dye in the prototype device proves that the biomimetic gel reactor could have high quantum efficiency per unit catalyst mass. This efficient operation is facilitated by the uniform catalyst distribution and transfer of the reagents through the three dimensional gel matrix. The simplicity of the matrix and the design makes such gel reactors readily scalable in the form of inexpensive flexible sheets filled with aqueous soft matter, which is, in the broader perspective, what nature is using in the form of the ubiquitous plant leaves. Similar hydrogel based reactors with microfluidic channel network could be a promising platform for multiple biomimetic energy harvesting systems as well as photoreactors for water treatment. Two other potential applications of the

microfluidic hydrogel platform could include future self-regenerating gel photovoltaic cells,¹² or biocomposite solar fuel cells, where the channels provide the nutrients to live cells hosted in the gel.

5.5. Acknowledgements

The authors are grateful for the support of this work provided by grants from the US Department of Energy (08NT0001925) and by the US National Science Foundation through the Research Triangle MRSEC on Programmable Soft Matter (DMR-1121107). We thank D. H. Kim for collecting SEM images and the group of Gregory Parsons for providing access to the solar simulator and SEM.

5.6. References

1. Erickson, D., Sinton, D. & Psaltis, D. Optofluidics for energy applications. *Nat. Photonics* **5**, 583-590, (2011).
2. Zhang, D., Li, G. & Yu, J. C. Inorganic materials for photocatalytic water disinfection. *J. Mater. Chem.* **20**, 4529-4536, (2010).
3. Gill, L. W. & McLoughlin, O. A. Solar disinfection kinetic design parameters for continuous flow reactors. *J. Sol. Energy Eng.* **129**, 111-118, (2007).
4. Zhou, H., Fan, T. & Zhang, D. An insight into artificial leaves for sustainable energy inspired by natural photosynthesis. *ChemCatChem* **3**, 513-528, (2011).
5. Lei, L. *et al.* Optofluidic planar reactors for photocatalytic water treatment using solar energy. *Biomicrofluidics* **4**, 043004-043012, (2010).
6. Lindstrom, H., Wootton, R. & Iles, A. High surface area titania photocatalytic microfluidic reactors. *AIChE J.* **53**, 695-702, (2007).
7. Lin, H. & Valsaraj, K. Development of an optical fiber monolith reactor for photocatalytic wastewater Treatment. *J. Appl. Electrochem.* **35**, 699-708, (2005).
8. Wheeler, T. D. & Stroock, A. D. The transpiration of water at negative pressures in a synthetic tree. *Nature* **455**, 208-212, (2008).
9. Wu, W. *et al.* Direct-write assembly of biomimetic microvascular networks for efficient fluid transport. *Soft Matter* **6**, 739-742, (2010).

10. Emerson, D. R., Cieslicki, K., Gu, X. & Barber, R. W. Biomimetic design of microfluidic manifolds based on a generalised Murray's law. *Lab Chip* **6**, 447-454, (2006).
11. Noblin, X. *et al.* Optimal vein density in artificial and real leaves. *Proc. Natl. Acad. Sci. U.S.A.* **105**, 9140-9144, (2008).
12. Koo, H.-J., Chang, S. T., Slocik, J. M., Naik, R. R. & Velev, O. D. Aqueous soft matter based photovoltaic devices. *J. Mater. Chem.* **21**, 72-79, (2011).
13. Zhou, H. *et al.* Biomimetic photocatalyst system derived from the natural prototype in leaves for efficient visible-light-driven catalysis. *J. Mater. Chem.* **19**, 2695-2703, (2009).
14. Okeyoshi, K., Suzuki, D., Kishimura, A. & Yoshida, R. Photoinduced hydrogen-generating nanogel systems. *Small* **7**, 311-315, (2011).
15. Kjeang, E., Michel, R., Harrington, D. A., Djilali, N. & Sinton, D. A microfluidic fuel cell with flow-through porous electrodes. *J. Am. Chem. Soc.* **130**, 4000-4006, (2008).
16. Koo, H.-J., Chang, S. T. & Velev, O. D. Ion-current diode with aqueous gel/SiO₂ nanofilm interfaces. *Small* **6**, 1393-1397, (2010).
17. Jokerst, J. V. *et al.* Location of biomarkers and reagents within agarose beads of a programmable bio-nano-chip. *Small* **7**, 613-624, (2011).
18. Ho, H. L. T. & Dryfe, R. A. W. Transport of neutral and ionic solutes: The gel/electrode and gel/electrolyte interfaces. *Langmuir* **25**, 12757-12765, (2009).
19. Johnson, E. M. & Deen, W. M. Hydraulic permeability of agarose gels, *AIChE J.* **42**, 1220-1224, (1996).
20. Johnson, E. M., Berk, D. A., Jain, R. K. & Deen, W. M. Diffusion and partitioning of proteins in charged agarose gels. *Biophys. J.* **68**, 1561-1568, (1995).
21. Lakshmi, S., Renganathan, R. & Fujita, S. Study on TiO₂-mediated photocatalytic degradation of methylene blue. *J. Photochem. Photobiol. A* **88**, 163-167, (1995).
22. Epling, G. A. & Lin, C. Photoassisted bleaching of dyes utilizing TiO₂ and visible light. *Chemosphere* **46**, 561-570, (2002).
23. Bird, R. E., Hulstrom, R. L. & Lewis, L. J. Terrestrial solar spectral data sets. *Sol. Energy* **30**, 563-573, (1983).
24. The effective volume was calculated by multiplying the “reaction area”, as shows in Figure 5.3, with the height of the channel. The resulting dimension is 14.5 mm × 30 mm × 0.5 mm.

Chapter 6

Computational Modeling and Optimization of Solute Supply through Hydrogel Based Porous Microfluidic Devices

6.1. Introduction

Microfluidic systems embedded in porous media could be a promising platform for various applications, such as flow reactors, drug delivery and energy harvesting devices. The microfluidic systems containing porous channel walls or plugs have a few specific advantages compared to conventional ones made of non-permeable materials. First of all, the porous structure intrinsically provides a number of interconnected microchannels, which enable selective transport of gasses and liquids or enhanced mixing by splitting and recombining incoming flows.¹⁻³ Additionally, the high surface area of the porous media could be used for efficient reaction sites when the pore surfaces are functionalized or the porous network is made of a reactive material itself.^{3,4} The pore size can be tuned depending on the composition of the porous materials, the preparation process or the external stimuli.^{3,5,6} The porous section can act as a filter or a valve.

A hydrogel can serve as a novel porous medium due to its high porosity and biocompatibility. Stroock et al. have done pioneering work on hydrogel based microfluidic systems for tissue engineering.^{7,8} Solutes are supplied via rapid convective transport along the microfluidic channels embedded in hydrogels, whereas diffusion by the concentration gradient is a dominant driving force for the delivery of the solutes in the porous hydrogel. Recently, we reported a hydrogel based photoreactor with a microfluidic network.⁹ An interdigitated channel design was used, which is inspired by a leaf venation network and a blood vessel system. The pressure gradient between the interdigitated source and drain channels enables convective transport as well as diffusion of solutes in the gel media. The microfluidic photoreactor could process the reactant solutes rapidly and uniformly via two transport mechanisms in the porous hydrogel media. Numerical simulation, where both convection and diffusion in porous media are taken into account, could help us gain a better understanding of solute transport in the device and optimize the channel structure according to desired applications.

Here, we present an extensive study of the mechanisms and transport efficiency of solutes in the biomimetic devices with microfluidic channels embedded in hydrogel media. We investigate the effect of the length of basic linear channels on the solute supply.

Numerical parameters are defined to quantitatively evaluate how rapidly and efficiently with minimum loss the solutes are transported in the channel designs. We compare T-shaped and branched channels to the linear channels to examine the effect of secondary channels branching off the primary ones. The dimensions of the channel designs are further optimized for more rapid and efficient solute supply based on the evaluation parameters obtained from the simulations. Experimental results are compared with the simulation ones to prove the validity of the simulation procedure established in this report. The simulation procedure can be extended to the microfluidic systems based on other general porous media.

6.2. Designs of Microfluidic Channels Embedded in Hydrogel and Numerical Simulation

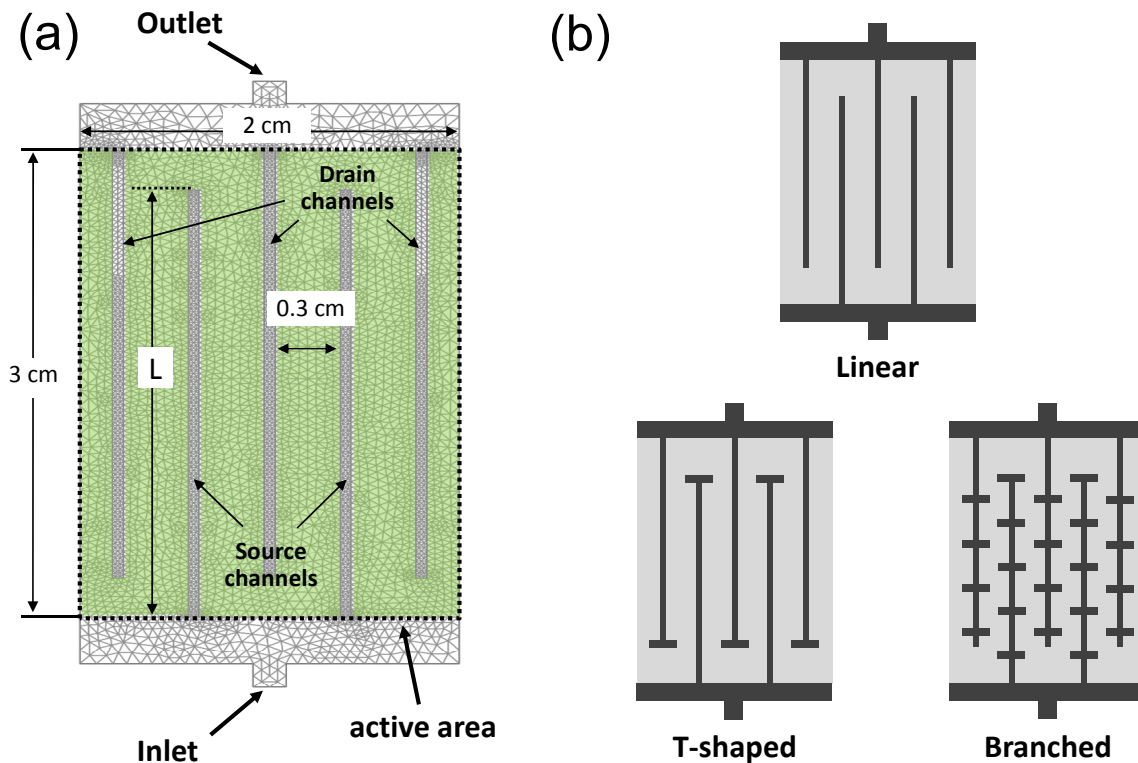


Figure 6.1. (a) A linear microfluidic design for finite element calculations. Light-green colored region is filled with porous hydrogel. The rectangle enclosed by the dotted lines indicates “active area” where solutes are supposed to be supplied. Solute concentration and efficiency of the device is calculated within this area. (b) Three representative designs of porous microfluidic channels compared in this study. Not to scale.

The numerical modeling of the solute distribution in porous gel devices with microfluidic channels was performed by using COMSOL multiphysics simulation package (COMSOL Inc., Burlington, MA). We designed 2-D interdigitated channel structure as shown in Figure 6.1(a), which includes two source channels and three drain channels. Such a channel structure is broadly similar to blood vessels. The source and drain channels and the microscopic open pores are analogous to arteries, veins and capillaries, respectively. We set the region covered with a porous gel as an “active area”. Solute coverage and efficiency are calculated within this area for parametric evaluation of the channel design efficiency. Its dimension is 2 cm × 3 cm. The channel width is 500 μm and the gap between the channels is fixed by 0.3 cm. The channel length, L , is varied between 1.5 cm and 2.95 cm. Solutions are injected from the inlet, flow through the channel-embedded porous gel and drain to the outlet, which is driven by pressure difference between the inlet and the outlet. The transport of the solute is governed by combined convection and diffusion, which is expressed by the following equation.

$$\frac{\delta c}{\delta t} = -\vec{v} \cdot \nabla c + D \nabla \cdot \nabla c$$

where c is the concentration of solute, D is the diffusion coefficient of the solute (3×10^{-10} m²/s, which is a same order of magnitude with the value of large dye molecules in the literatures)¹⁰ and \vec{v} is the velocity of fluid. The first and the second terms represent transports driven by convection and diffusion, respectively. To calculate the velocity of fluid determining the term for the transport by convection, we used two different equations; Brinkman equation for the porous gel region (green colored area in Figure 6.1(a)) and Navier-Stokes equation for non-porous region.

$$\frac{\eta}{k} \vec{v} = \nabla \cdot \left\{ -\vec{p} + \frac{\eta}{\varepsilon_p} (\nabla \vec{v} + (\nabla \vec{v})^T) \right\} \quad (\text{Brinkman equation in porous region})$$

$$\rho \vec{v} \cdot \nabla \vec{v} = \nabla \cdot \left\{ -\vec{p} + \eta (\nabla \vec{v} + (\nabla \vec{v})^T) \right\} \quad (\text{Navier-Stokes equation in nonporous region})$$

$$\nabla \cdot \vec{v} = 0 \quad (\text{in all media})$$

where η is the viscosity of the solution (1×10^{-3} Pa·s), ρ is its density (1×10^3 kg/m³), k is the permeability of porous hydrogel (5.4×10^{-16} m² for agarose hydrogel)¹¹ and ε_p is the gel porosity (0.98).¹² The inlet boundary conditions are a constant pressure of 7×10^3 Pa and the concentration of 5 mol/m³. The outlet boundary conditions are no pressure and the convection-dominant transport with negligible diffusion ($\vec{n} \cdot (-D\nabla c) = 0$). All equations were used as predefined in the COMSOL simulation package. To further optimize the channel structure for rapid and efficient supply of the solutes, we compared three different designs of channels; linear, T-shaped and branched (Figure 6.1(b)). We ran all the time-dependent simulations for the convection and diffusion of solute up to 7200 s.

6.3. Results and Discussion

6.3.1. Solute Transport in Porous Gels with Linear Channel Design and Numerical Parameters for Evaluation of Channel Designs

The simulation results of solute distribution in the linear-microfluidic gel devices with different channel lengths are shown in Figure 6.2. Qualitatively, the area infused with the solute at the same points in time increases as the length of the linear channels increases, which means a longer microfluidic channel exhibits a higher supply rate of the solute under an identical pressure. This result is associated with the different resistance to flow depending on the channel lengths. The resistance to flow is much higher in the porous media than in the non-porous channels. As the channel length increases, the solution can flow through more shorter pathways in the porous media, which reduces the flow resistance. When the channel length is too long, however, the supply of the solute could be less efficient because of the large loss of the supplied solute. For example, in a 2.95 cm channel design in Figure 6.2d, relatively large amount of the solute flows out of the device compared to the designs with shorter channel lengths.

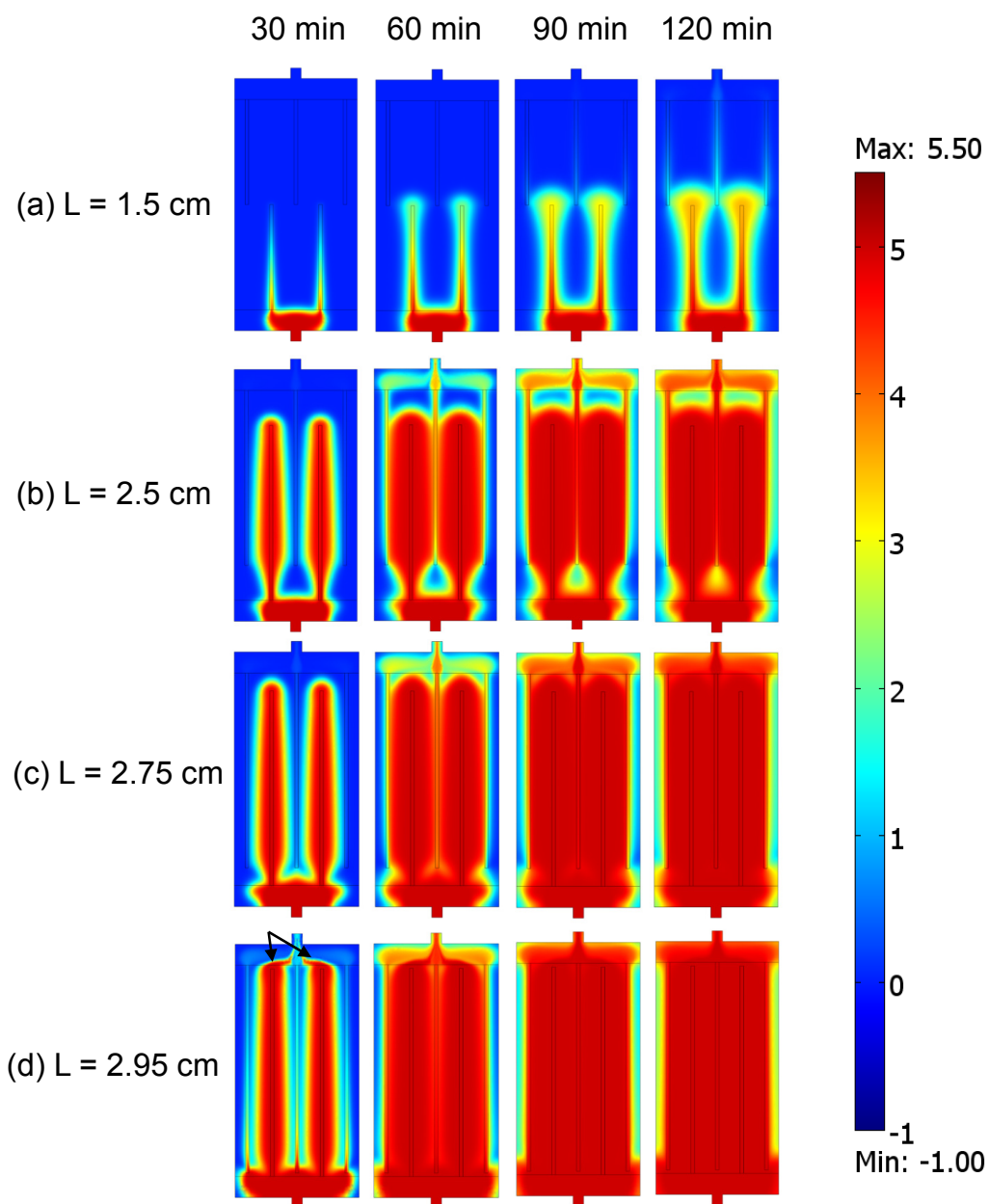


Figure 6.2. Simulation results for solute distribution at various points of time in linear-microfluidic gel devices with different channel length (L). The arrows in the device with 2.95 cm long channels indicate the direct drainage from the source channels to the outlet.

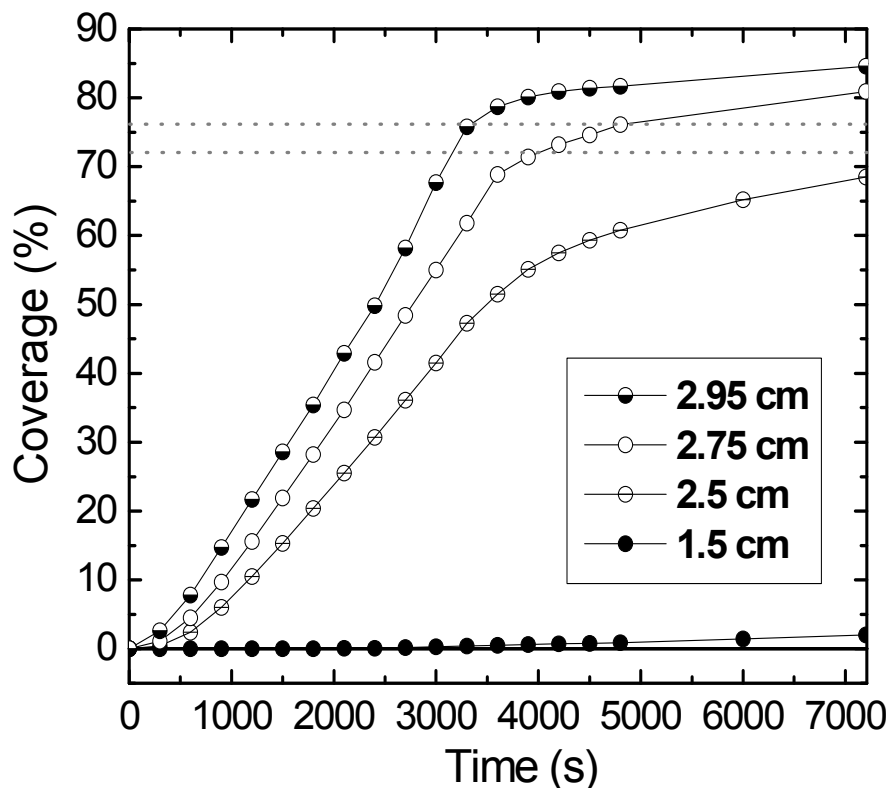


Figure 6.3. Degree of solute penetration of the linear-microfluidic gel devices with different channel lengths as a function of time. The area of solute coverage was obtained by using Photoshop. Two dotted lines represent 72% and 76% of coverage in the active area.

To quantitatively evaluate how rapid the solute is supplied in each channel structure, we compare $T_{a\%}$, the time required for a given coverage of the solute of $a\%$ in the active area. The solute coverage of the active area as a function of time is shown in Figure 6.3. The coverage is the ratio of the area with the solute concentration higher than 4 mol/m^3 to the total active area. It is confirmed that the coverage increases faster as the channel length increases. The device with 1.5 cm channel length shows negligible coverage within our maximum simulation time range of 7200 s. The slopes of other graphs decrease drastically around 3500 s, when the solute reaches the outlet and the solute loss begins to increase (Figure 6.4). We compared $T_{72\%}$ and $T_{76\%}$ of each channel length. The pseudo-full coverage, when the area between the two outermost drain channels is filled as at 120 min in Figure 6.2(d), is around 80%. The coverage of 72% and 76% is equivalent to 90% and 95%

when the coverage is adjusted based on the pseudo-full coverage of 80%. $T_{72\%}$ and $T_{76\%}$ of the linear channel-embedded gels with various channel lengths are summarized in Table 6.1. The devices with the channel lengths less than 2.5 cm do not achieve 72% solute coverage within 7200 s. The device with the 2.95 cm channels exhibits 20~30% shorter $T_{72\%}$ and $T_{76\%}$ than that with the 2.75 cm channels because of lower resistance to flow in the porous gel media as discussed. It is also confirmed that the molar rate of the solute increases as the channel length increases (Table 6.1). Thus, the longer microfluidic channel can supply faster the solute in the linear-channel structure.

Besides the rapid infusion with the solute, it is also important how efficiently the solute can be distributed to the active area with minimum solute loss through the outlet. We define the efficiency of a channel design as the ratio of the amount of the solute in the active area to the total amount of the solute injected until a certain time. The efficiencies of the linear channel-embedded hydrogels at $T_{72\%}$ and $T_{76\%}$ are compared in Table 6.1. Between two devices achieving more than 72% coverage within 7200 s, the device with the 2.75 cm channels has higher efficiency than that with the 2.95 cm channels for the 72% coverage, whereas, for the 76% coverage, the efficiency of the device with the 2.95 cm channels is slightly higher than that of the device with the 2.75 cm. The efficiencies are inversely proportional to the solute loss, C_{out} . The outflow of the solute starts at ~1000 s in the 2.95 cm channel design, which is much faster than ~2500 s in the 2.75 cm channel design (Figure 6.4(a)). Such an early solute loss in the 2.95 cm channel design results from the direct drainage from the source channels to the outlet before the lateral transport to the drain channels (See the result for solute distribution at 30 min in Figure 6.2(d)). However, the solute loss in the 2.75 cm channel design significantly increases from $T_{72\%}$ to $T_{76\%}$ and becomes larger than that in the 2.95 cm channel design at $T_{76\%}$. Thus, the efficiency of the solute supply can be different depending on a given coverage as well as channel designs. In this simulation study, we set the 76% coverage as an optimum coverage, where the 2.95 cm channel design shows the most efficient solute supply.

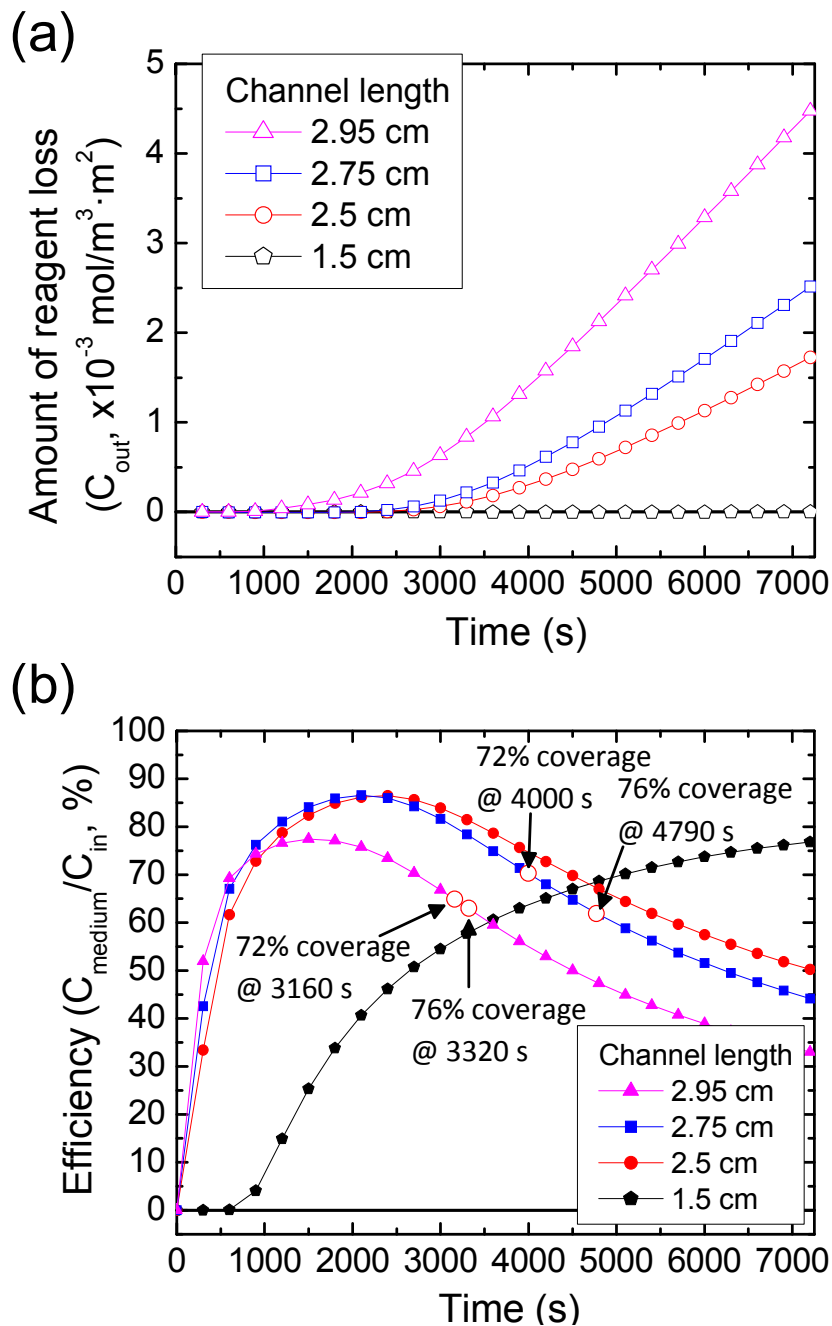


Figure 6.4. (a) The amount of the reagent loss and (b) the efficiency as a function of time in linear-microfluidic gel devices with different channel length.

Table 6.1. Numerical parameters for the evaluation of the rapidity and the efficiency of the linear channel-embedded hydrogels with different channel lengths: Molar rate, the required time (T), solute loss (C_{out}) and efficiency for 72% and 76% of coverage. The graphs of the efficiencies as a function of time are shown in Figure 6.4. C_{out} and efficiency were not obtained for the channel lengths of 1.5 cm and 2.5 cm where the 72% coverage was not achieved within 7200 s.

Channel Length	Molar rate ($\times 10^{-7}$ mol $m^{-1}s^{-1}$)	For 72% coverage (effective coverage: 90%)			For 76% coverage (effective coverage: 95%)		
		$T_{72\%}$	C_{out} ($\times 10^{-4}$ mol m^{-1})	Efficiency (%)	$T_{76\%}$	C_{out} ($\times 10^{-4}$ mol m^{-1})	Efficiency (%)
1.5 cm	1.0	>>7200	–	–	>>7200	–	–
2.5 cm	6.0	>>7200	–	–	>>7200	–	–
2.75 cm	7.5	4000	5.2	70	4790	9.5	62
2.95 cm	10.4	3160	7.4	65	3320	8.6	63

6.3.2. Effect of Secondary Branches on Rapid and Efficient Supply of Solutes

A vascular system in many natural leaves consists of a primary vein and secondary veins branching off the primary vein. (Evolution and Function of Leaf Venation Architecture: A Review) The hierarchical structure of the veins enables uniform and efficient supply of water and minerals. To mimic the structure of the vascular system of leaves, we designed T-shaped channels as a simple model, where one pair of the secondary branches was added at the end of the linear channels. We simulated the solute transport in the devices with the T-shaped channels while varying the length of the primary channels (Figure 6.5(a-c)). It should be noted that the solute coverage of the T-shaped channels at 2700 s is comparable to that of the linear channels at 3600 s (60 min) in Figure 6.2, which qualitatively confirms that the secondary branches of the T-shaped channels could allow the faster solute supply. The numerical parameters for the linear and the T-shaped channel designs as a function of the primary channel length are compared in Figure 6.6. The T-shaped design has higher molar rate and, therefore, shorter $T_{76\%}$ than the linear design in all channel length. The T-shaped design also has slightly higher efficiency at $T_{76\%}$ than the linear design in the 2.75 cm channel length. However, the efficiency of the T-shaped design at $T_{76\%}$ drastically decreases in the 2.95 cm channel length and is 15% lower than that of the linear design, which results

from the large loss of the solute as shown in Figure 6.5(c). Thus, the T-shaped channel enables faster supply of the solute than the linear channel design in the same channel length and has the optimum channel length of 2.75 cm for the efficient supply.

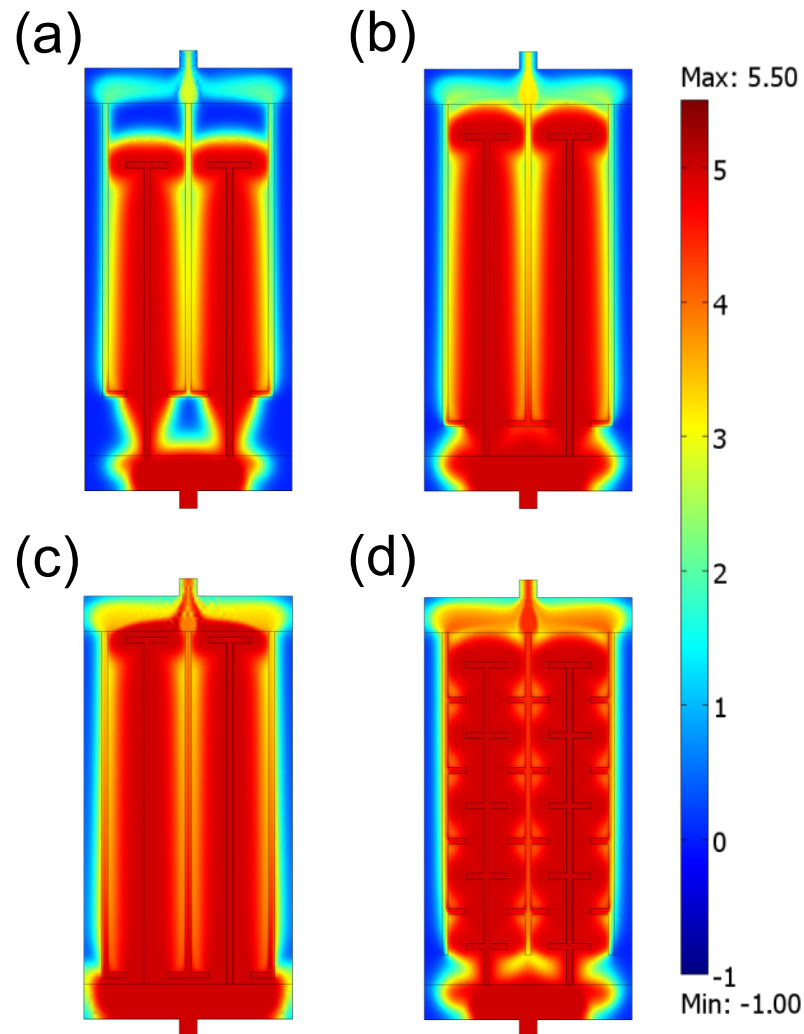


Figure 6.5. (a-c) Simulation results for solute distribution at 2700 s in T-shaped channel-embedded hydrogels with different channel lengths. (a) 2.5 cm, (b) 2.75 cm, (c) 2.95 cm. (d) Simulation results for solute distribution at 2700 s in branched channel-embedded gels. The channel length is 2.75 cm. The length of secondary branches from the primary channels is 1.5 mm in all designs.

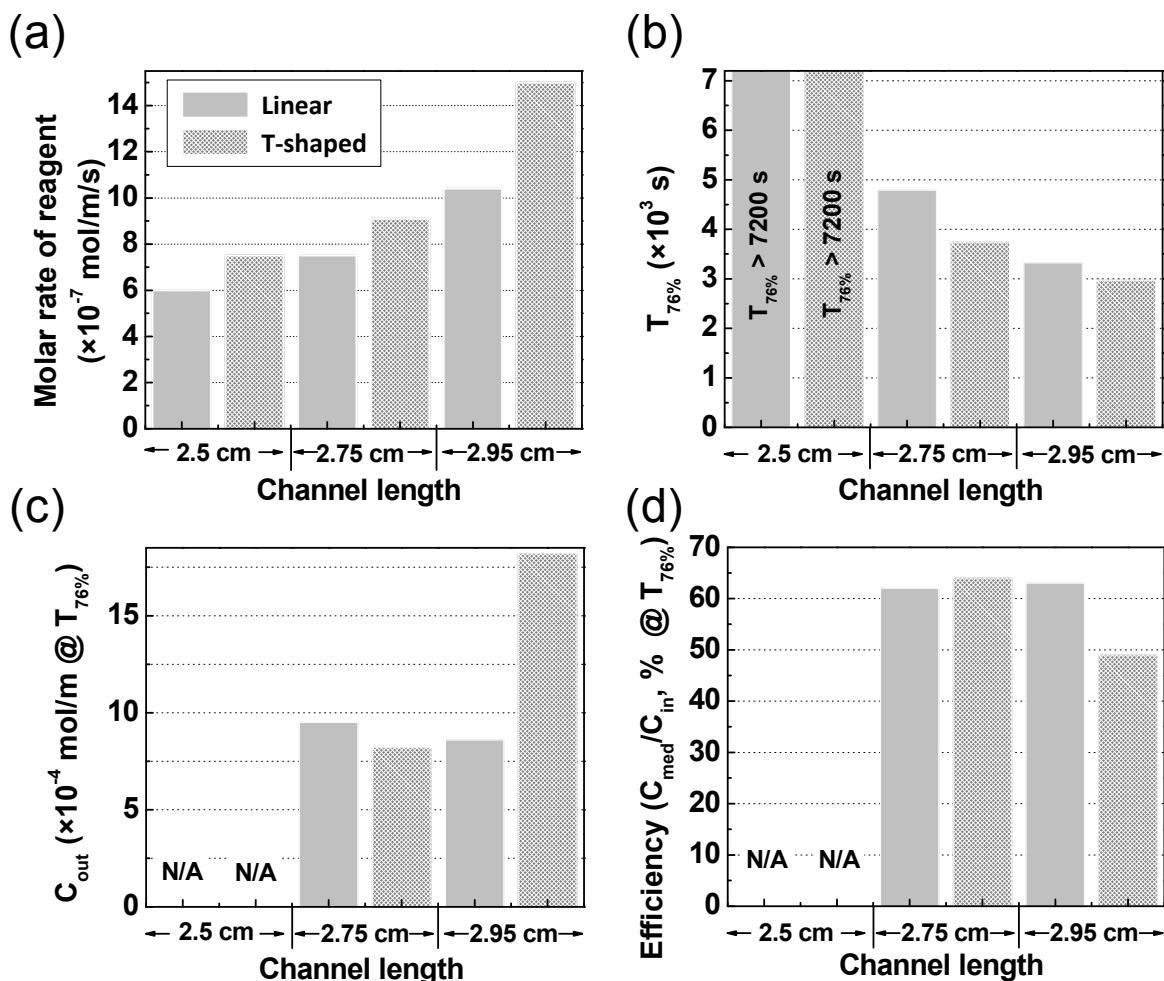


Figure 6.6. Comparison of the molar injection rate of solute, the time for 76% solute coverage, the solute loss and the efficiency at $T_{76\%}$ between linear and T-shaped channels with different lengths of the primary channels.

We also investigated the effect of the number of the secondary channels on the rapidity and the efficiency of the microfluidic hydrogel devices by comparing the branched design with the linear and the T-shaped ones. The branched design has five pairs of the secondary channels per source primary channel and four pairs of the secondary channels per drain primary channel. The channel length was fixed at 2.75 cm, where the T-shaped design shows the most efficient supply of the solute in Figure 6.6(d). Figure 6.5(d) shows the simulated concentration profile of the solute in the device with the branched channels at 2700 s, where the solute is distributed more uniformly than in those with the linear and the

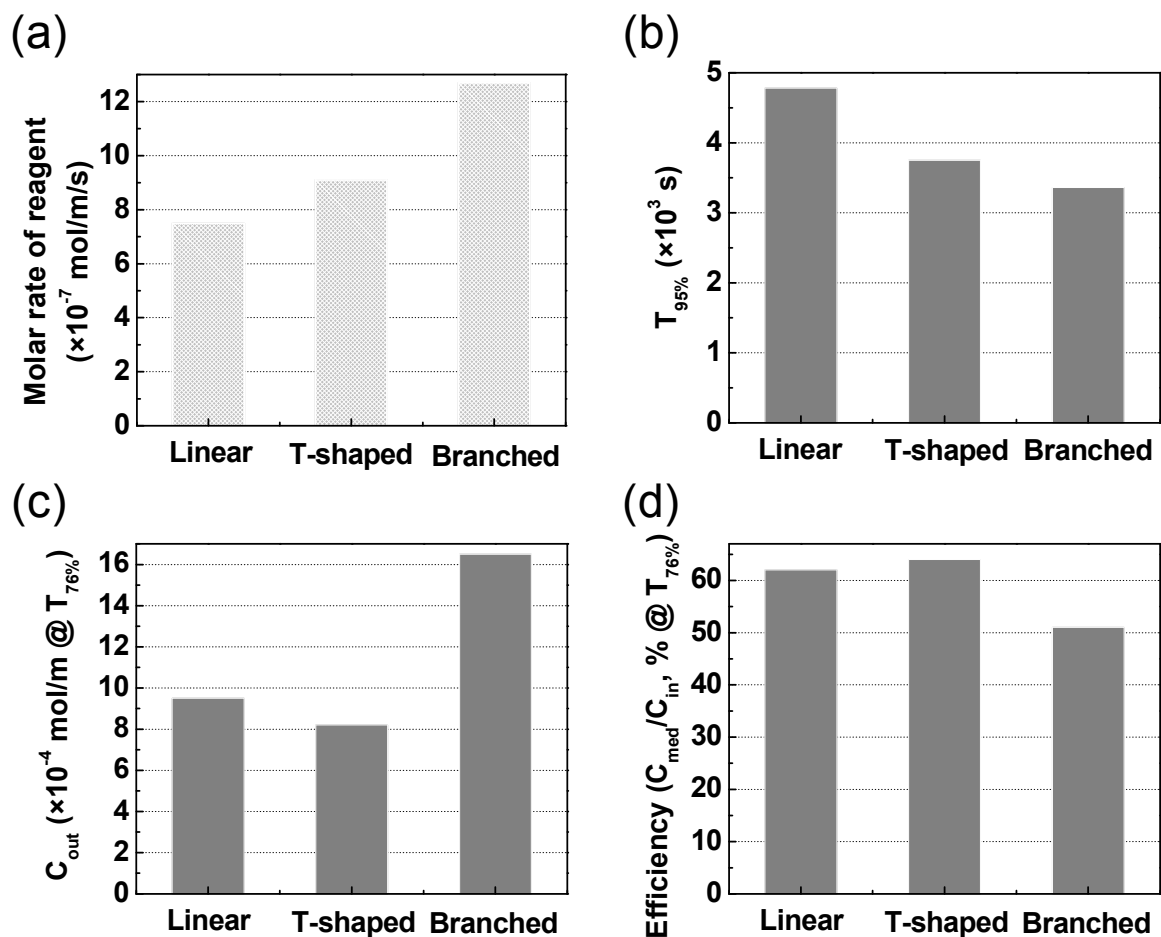


Figure 6.7. Comparison of the molar injection rate of solute, the time for 76% solute coverage, the solute loss and the efficiency at $T_{76\%}$ of microfluidic devices with linear, T-shaped and branched channels. The primary channel length is 2.75 cm in all devices.

T-shaped channels at the same point in time (Figure 6.2(c) and 6.5(b)). The numerical parameters of the three designs are compared in Figure 6.7. The branched design has the highest molar rate, thereby achieving the 76% coverage rapidest among the three designs. The efficiency of the branched design at $T_{76\%}$ is, however, more than 10% lower than those of the linear and the T-shaped design due to the significant loss of the solute. The T-shaped design, identified as the most efficient one, was further optimized by investigating the effect of the length of the secondary branches on the efficiency at $T_{76\%}$ (Figure 6.8 and 6.9). It turns

out that the optimized branch length of the T-shaped design is 1 mm where the solute could be supplied most efficiently with minimum loss at 76% coverage.

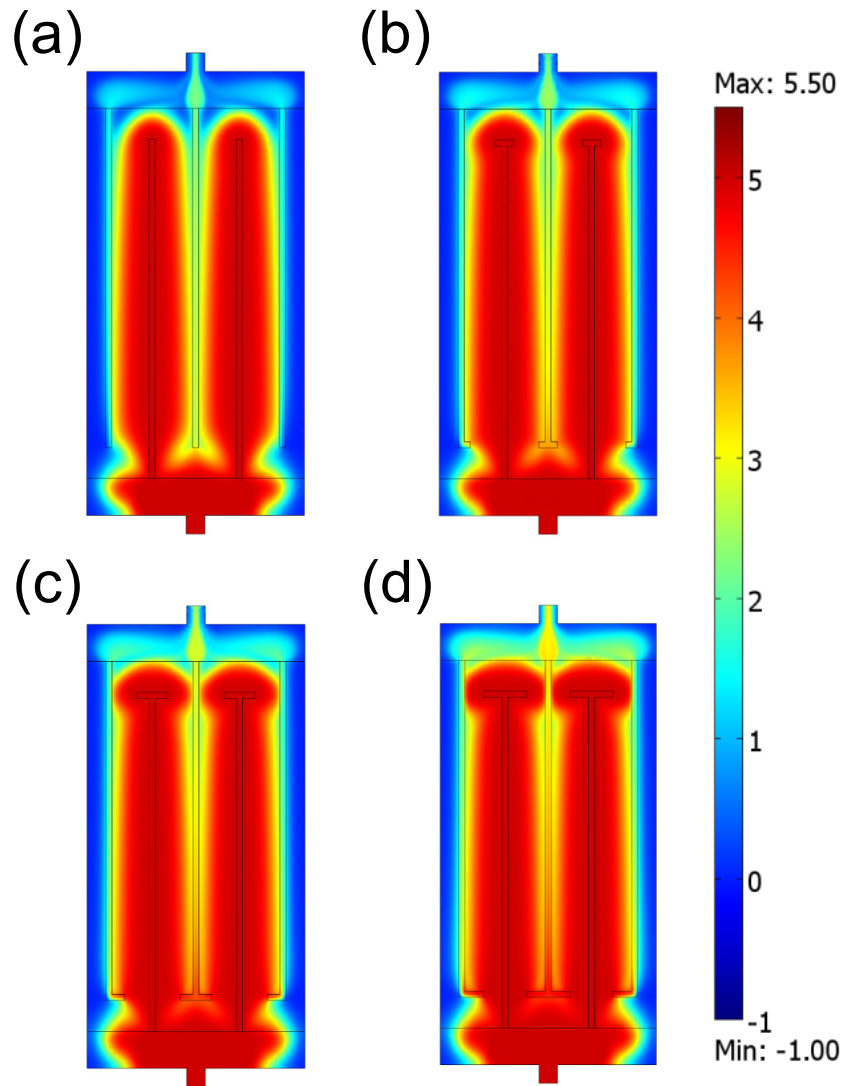


Figure 6.8. Simulation results for reagent distribution at 2700 s in T-shaped microfluidic devices with different branch length. (a) no tail (linear channels), (b) 0.5 cm, (c) 1.0 cm, (d) 1.5 cm.

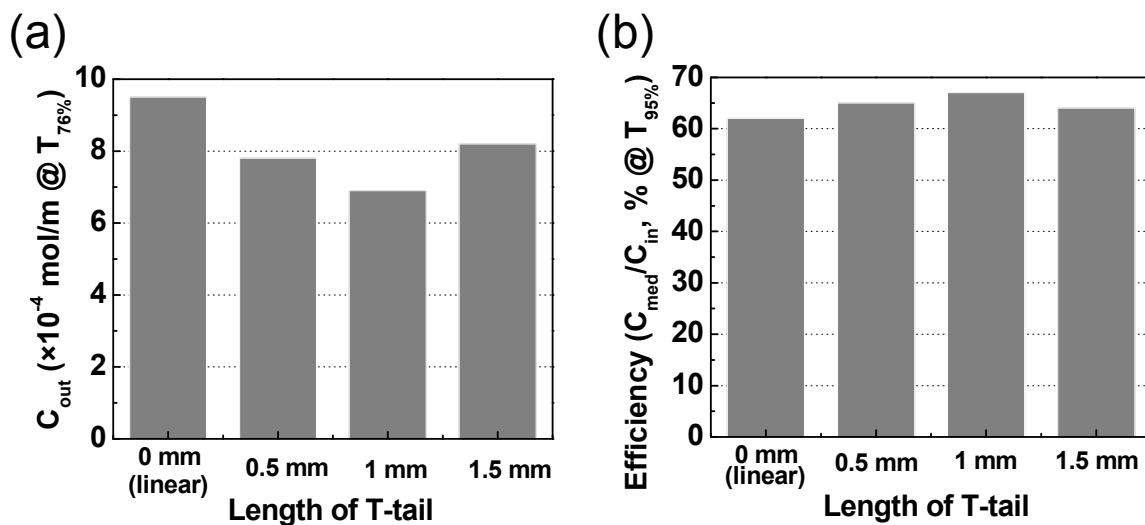


Figure 6.9. The effect of the length of the secondary branches in T-shaped design on (a) the solute loss and (b) the efficiency at $T_{76\%}$.

6.3.3. Comparison of Simulation and Experiment Results for Solute Transport in Microfluidic Hydrogels

To evaluate the validity of the simulation results, we have observed the dye transport in a prototype of the microfluidic device based on hydrogels. The device was fabricated by the same process as in our previous publication.⁹ Microfluidic channels with the branched design in Figure 6.5(d) were formed in the hydrogel by replica molding. The channel height was ~ 500 μm . Aqueous solution of 0.1 M Allura Red dye was injected at a constant flow rate of 10 $\mu\text{l}/\text{min}$ with a syringe pump. The estimated flow rate under the pressure of 7×10^3 Pa, which is the inlet boundary condition for the simulation, is ~ 8 $\mu\text{l}/\text{min}$. The penetration of the dye solution was followed by optical imaging. The dye distribution profiles at 5, 10, 20 and 30 minutes after the dye injection were compared with the simulation results in Figure 6.10. The temporal distribution of the dye of the experimental data is in excellent agreement with that of the simulation, which proves that the solute transport through the microvascular gels can be reasonably predicted by using the simulation procedure established in this study.

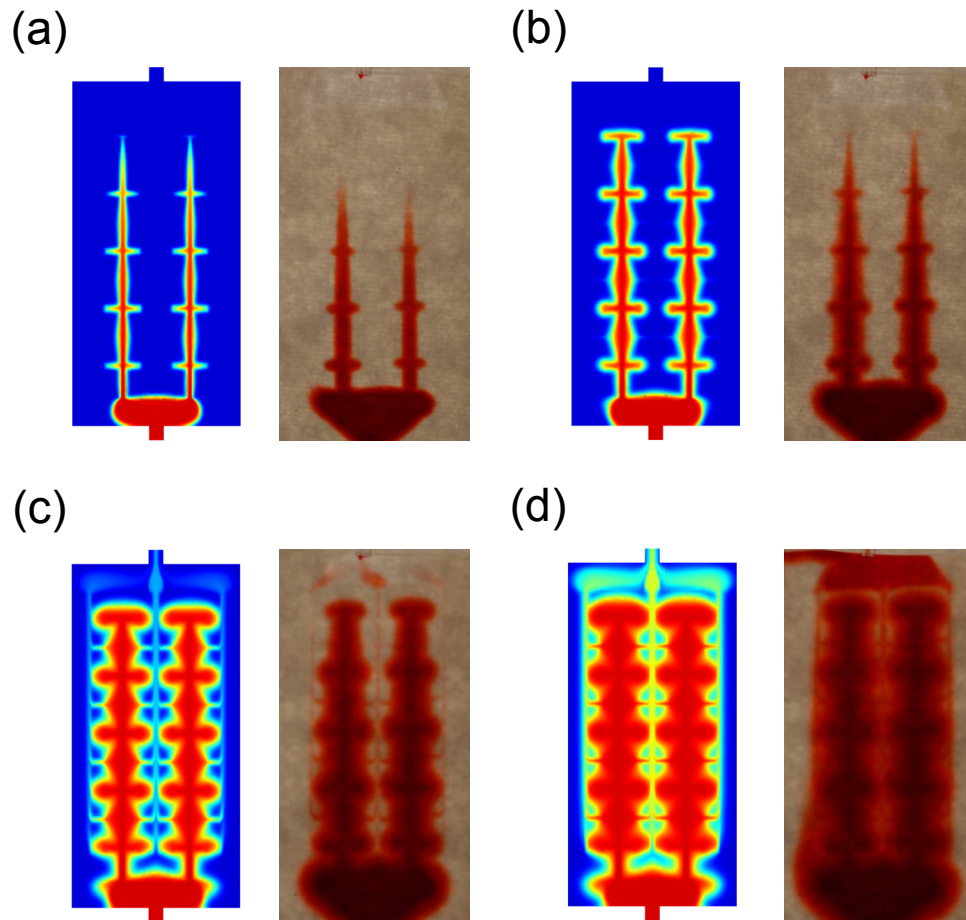


Figure 6.10. Comparison of simulation and experiment results for time-lapse dye transport in hydrogel microfluidic devices. (a) 5 min, (b) 10 min, (c) 20 min and (d) 30 min after injection of the dye solution.

6.4. Conclusions

In summary, we have performed a simulation study of the solute transport in a biomimetic hydrogel with microvascular network. The interdigitated channel design is inspired by a blood vessel system. The numerical parameters have been defined to quantitatively evaluate channel designs with different dimensions and structures. Comparative study between the linear and the T-shaped channels reveals that the secondary branches could enable rapid and more efficient supply of solutes at the optimized length of the primary channels. To investigate the effect of the number of the secondary branches, we have compared the

evaluation parameters of the branched channels with those of the linear and the T-shaped ones. It turns out that the branched channels enable the fastest, but most inefficient solute supply, resulting from the large loss of the solute. The T-shaped channels, the most efficient design, have been further optimized by varying the length of the secondary branches. The experimental data of the dye transport in a prototype device with a microfluidic gel accord well with the simulation results, which proves the validity of the simulation procedures we establish in this report. Since the Brinkman equation we use for the simulation study is a general expression that describes the fluid flow in porous media, the simulation procedure can be extended to microfluidic systems based on other porous materials. Such a simulation tool can be used to optimize the channel designs for rapid and efficient solute supply in a porous microfluidic media, which could be a potential platform for various applications, ranging from continuous reactor to solar- or fuel-cells and drug delivery systems.

6.5. References

1. Yuen, P. K. & DeRosa, M. E. Flexible microfluidic devices with three-dimensional interconnected microporous walls for gas and liquid applications. *Lab Chip* **11**, 3249-3255 (2011).
2. Yuen, P. K., Su, H., Goral, V. N. & Fink, K. A. Three-dimensional interconnected microporous poly(dimethylsiloxane) microfluidic devices. *Lab Chip* **11**, 1541-1544 (2011).
3. Simms, H. M. *et al.* *In situ* fabrication of macroporous polymer networks within microfluidic devices by living radical photopolymerization and leaching. *Lab Chip* **5**, 151-157 (2005).
4. Kjeang, E., Michel, R., Harrington, D. A., Djilali, N. & Sinton, D. A microfluidic fuel cell with flow-through porous electrodes. *J. Am. Chem. Soc.* **130**, 4000-4006 (2008).
5. Moorthy, J. & Beebe, D. J. *In situ* fabricated porous filters for microsystems. *Lab Chip* **3**, 62-66 (2003).
6. de Jong, J., Ankone, B., Lammertink, R. G. H. & Wessling, M. New replication technique for the fabrication of thin polymeric microfluidic devices with tunable porosity. *Lab Chip* **5**, 1240-1247 (2005).

7. Cabodi, M. *et al.* A microfluidic biomaterial. *J. Am. Chem. Soc.* **127**, 13788-13789 (2005).
8. Choi, N. W. *et al.* Microfluidic scaffolds for tissue engineering. *Nat. Mater.* **6**, 908-915 (2007).
9. Koo, H.-J. & Velev, O. D. Submitted.
10. Zanarini, S. *et al.* Ru(bpy)₃ covalently doped silica nanoparticles as multicenter tunable structures for electrochemiluminescence amplification. *J. Am. Chem. Soc.* **131**, 2260-2267 (2009).
11. Johnson, E. M. & Deen, W. M. Hydraulic permeability of agarose gels. *AIChE J.* **42**, 1220-1224 (1996).
12. Johnson, E. M., Berk, D. A., Jain, R. K. & Deen, W. M. Diffusion and partitioning of proteins in charged agarose gels. *Biophys. J.* **68**, 1561-1568 (1995).

Chapter 7

Microvascular Hydrogel Photovoltaics with Biomimetic Regeneration Functionality

7.1. Introduction

Inspired by the photosynthesis of a natural leaf, dye-based photovoltaic systems has been proposed and actively developed, including common dye-sensitized solar cells (DSSCs)^{1,2} and hydrogel-based photovoltaics (HGPVs) newly developed by us.³ The photoactive dye molecules absorb photons from the sun and convert them into electrical energy, analogous to the function of photosystems, which are photoactive protein complexes in a leaf involved in photosynthesis. Since the dyes are generally susceptible to light, high temperature and water, however, the degradation of photoactive molecules in the dye-based photovoltaic systems could be a critical problem, which leads to deterioration of the long-term performance of photovoltaic cells.⁴⁻¹¹

The light-induced damage of the photosystems also occurs in a natural leaf. When the photosystems are irreversibly damaged by light stress, a natural leaf disassembles the damaged components in the photosystems and replaces them with the fresh newly biosynthesized ones.¹² Such a self-regeneration process of a leaf could minimize the light-induced impairment of photosynthesis efficiency. Ham et al. have reported a pioneering work of synthesis of a photoelectrochemical complex composed of lipids, proteins, carbon nanotubes and photosynthetic reaction centre.¹³ The complex can be regenerated by assembly/disassembly controlled by presence or absence of surfactants. Here, we present a practical prototype of biomimetic photovoltaics structure realizing the regeneration functionality of a plant leaf. The device is based on an agarose gel, which is a naturally derived hydrogel, with embedded microfluidic channels inspired by hierarchical leaf venation network.¹⁴ The transport of the photoactive reagents, dye and electrolytes, supplied into the microfluidic hydrogels will be discussed. We propose a simple and reliable process for the regeneration of the microfluidic hydrogel solar cells by controlling the pH-dependent desorption/adsorption kinetics of the dye molecules on photoanodes. Finally, we demonstrate the photocurrent recovery of the biomimetic solar cells damaged by intense UV illumination.

7.2. Experimental Section

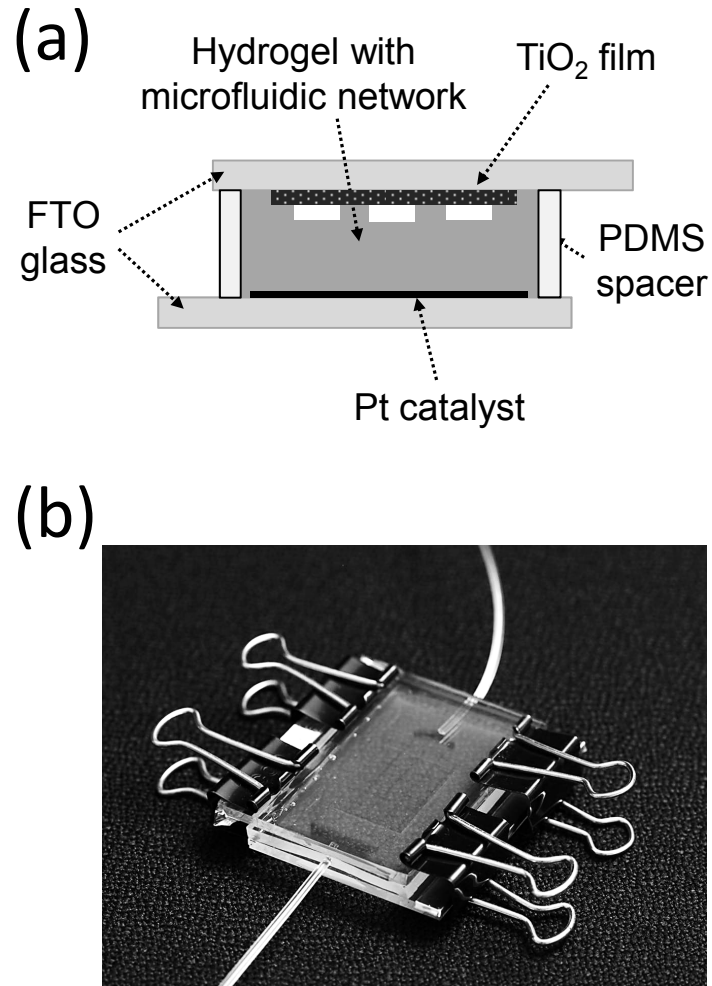


Figure 7.1. (a) A schematic cross-section view of the μ -FGPVs. (b) A photograph of the prototype device of the μ -FGPVs.

The structure of the biomimetic photovoltaics based on a hydrogel with embedded microfluidic network (μ -fluidic gel photovoltaics, μ -FGPVs) is shown in Figure 7.1. The device is designed on the basis of the structure of DSSCs which are solar harvesting systems emulating the primary steps of photosynthetic process in a natural leaf.¹⁵⁻¹⁷ A nanoporous TiO₂ thin film and platinum catalysts are formed on two fluorine-doped tin oxide (FTO) glass

substrates (TEC-8, 2.3 mm thick, Hartford), which are used as a photoanode and a counter electrode, respectively. The nanoporous TiO₂ film is prepared by doctor-blading of a screen printable TiO₂ paste (Ti-Nanoxide T20, Solaronix), followed by sintering at 500 °C for 90 min. The thickness and the area of the TiO₂ film are ~ 6 μm and 3 cm². The platinum catalysts are deposited by spin-coating of 0.7 mM H₂PtCl₆ solution, followed by heating at 400 °C for 20 min. The agarose gel layer with interdigitated microfluidic networks is prepared by replica molding as reported in the literature.¹⁸ We chose the interdigitated structure with “branched” channels for uniform and rapid reagent supply.¹⁴ The hydrogel layer with microfluidic channels is sandwiched between the photoanode and the counter electrode. Reagents for the photovoltaic operations, photosensitive dyes and electrolytes, could be provided, removed and replenished uniformly by a convective/diffusive transport mechanism in the hydrated porous gel media with the microfluidic network. The channels are facing the TiO₂ film to facilitate the adsorption and desorption of the dyes.

7.3. Results and Discussion

7.3.1. Supply of Photovoltaic Reagents into μ-FGPVs

The μ-FGPVs demonstrated in Figure 7.1 are able to utilize incident photons to convert into electrical energy when photosensitive dyes are introduced. The common dye Eosin Y could be an inexpensive and reasonably efficient photosensitive reagent in DSSCs.¹⁹⁻²¹ The aqueous solution containing 0.005 M Eosin Y, 0.6 M potassium iodide and 0.03 M iodine was injected into the prototype device assembled as in Figure 7.1. The infusion of the dye and electrolyte solution through the microfluidic hydrogel media is shown in Figure 7.2 (a). Since the resistance to flow of the solution is lower in the channel network than in the porous gel media, the solution first flows along the source channels, followed by penetrating through the gel to reach the drain channels. The dye and the electrolytes are predominantly delivered by convective transport along the channels, whereas the diffusion of the reagent molecules becomes more important in the penetration of those reagents through the gel. Computational simulation reveals that the Peclet number - a dimensionless number representing the ratio of the convection rate to the diffusion rate - in the gel is ~ 3 compared to 110 ~ 140 in the

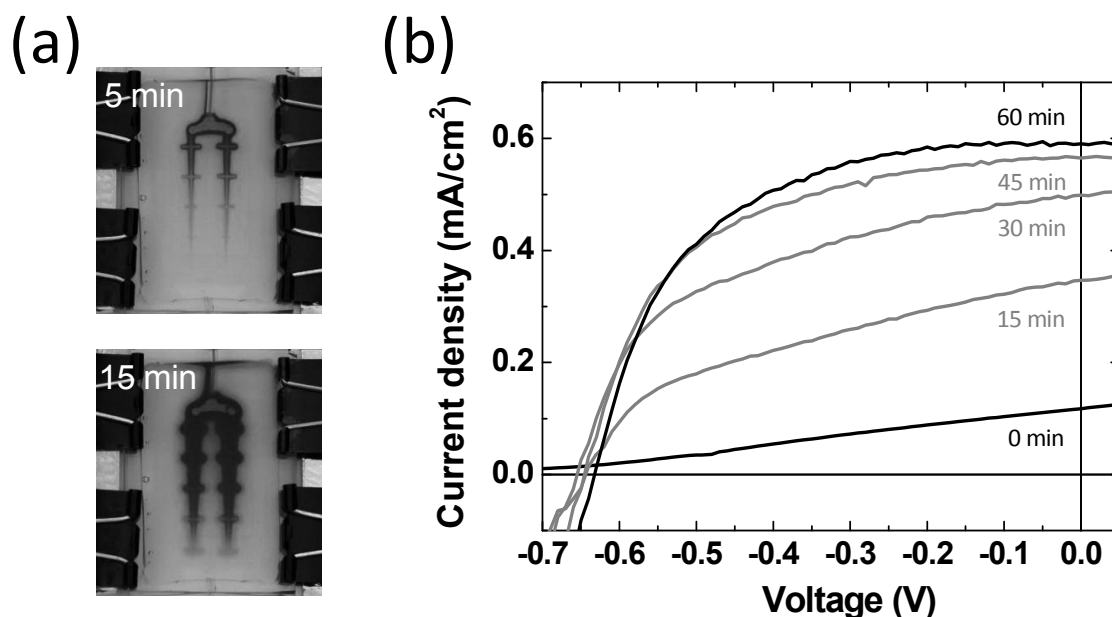


Figure 7.2. (a) Images illustrating the infusion of dye and electrolytes through the gel-vascular network at 5 and 15 min after injection of the solution. The injection rate is 10 $\mu\text{l}/\text{min}$. (b) I-V curves of the $\mu\text{-FGPVs}$ under illuminated condition after the injection of the aqueous solution of dye and electrolytes. The device is illuminated with a solar simulator with 300 W Xenon lamp ($100 \text{ mW}/\text{cm}^2$, New Port).

channels (Figure 7.3).¹⁴ Since the diffusion is driven by the concentration gradient, the enhanced diffusive transport in the porous gel media could intrinsically enable the uniform distribution of the reagent while the convection dominant transport in the channels allow the rapid supply.

To characterize the role of the introduced dye and electrolytes to the photovoltaic operation, we measured the current density of the $\mu\text{-FGPVs}$ as a function of the applied voltage under illumination during the supply of the reagents as shown in Figure 7.2 (b). The short-circuit current (J_{sc}) increases as more solution of dye and electrolytes is infused, however, the open-circuit voltage (V_{oc}) barely changes since the solution is introduced. The result is reasonable because J_{sc} mostly depends on the amount of the dye molecules adsorbed on the TiO_2 surface,²² while V_{oc} is determined by the energy difference between the Fermi-level of the TiO_2 electrode and the redox potential of the electrolytes.²³ The J_{sc} is saturated at

60 min after the injection when the dye and electrolytes appear to have reached adsorption equilibria with the TiO₂ photoanode. The resulting J_{sc} , V_{oc} , fill factor and efficiency are 0.59 mA/cm², 630 mV, 0.57 and 0.21%, respectively. Thus, the biomimetic hydrogel device is successfully operated as photovoltaic source with uniform supply of the dye and electrolytes via the microfluidic network mimicking leaf venation architecture.

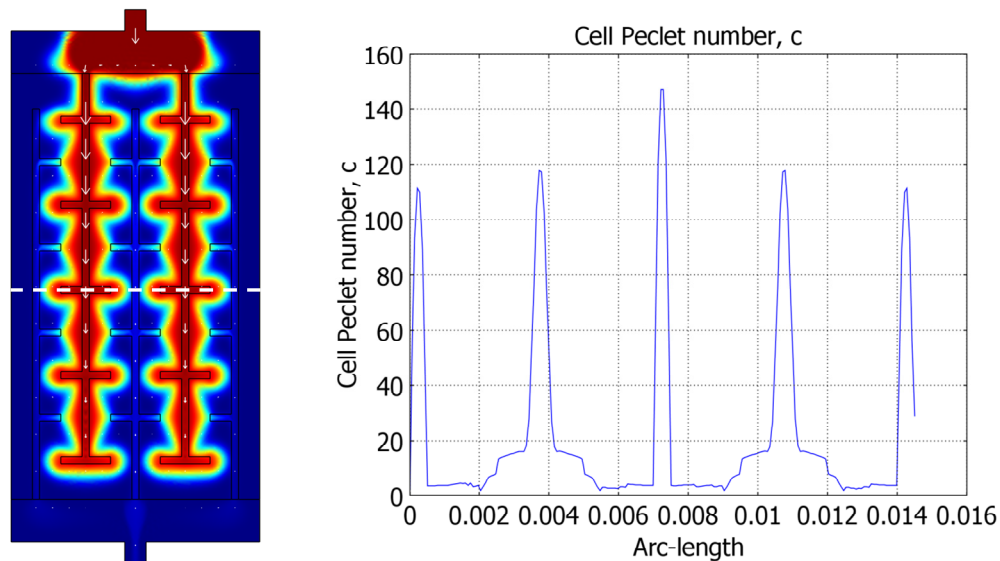


Figure 7.3. The distribution of Pelet number in the μ -FGPVs. The graph on the right shows the Pelet numbers along the dotted line on the left figure.

7.3.2. Development of Biomimetic Regeneration Process

A plant in nature maintains its photosynthetic activity by continually regenerating photoactive complexes in leaves. The light-degraded protein in photoactive complexes are disassembled and replaced by fresh protein by a biologically repair cycle.^{12,13} To adopt the regeneration functionality of a natural plant, we have established a regeneration process schematically described in Figure 7.4 (a), by which the dye and electrolytes provided can be removed and replenished on demand. When the dye solution is introduced to the pristine TiO₂ in Figure 7.2, the Eosin Y molecules are chemically adsorbed on the TiO₂ surface by dehydration reaction, which absorb the photons and inject the excited electrons to the

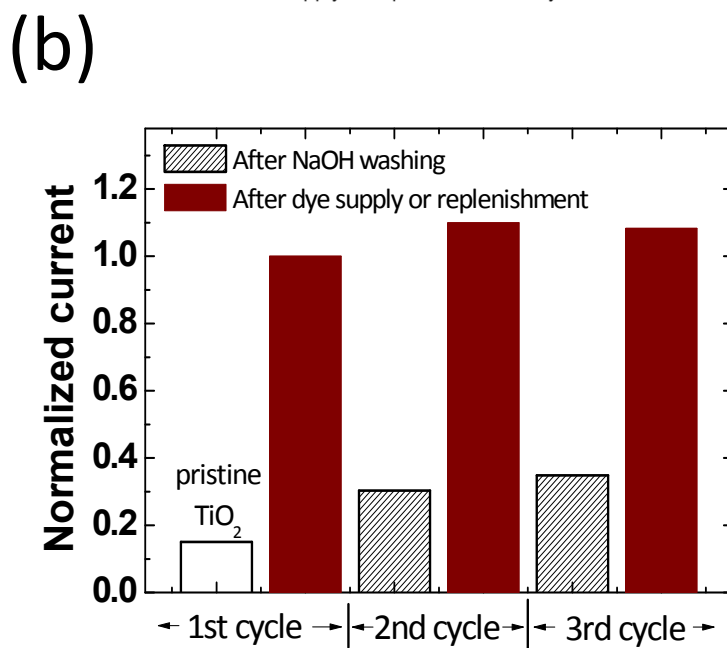
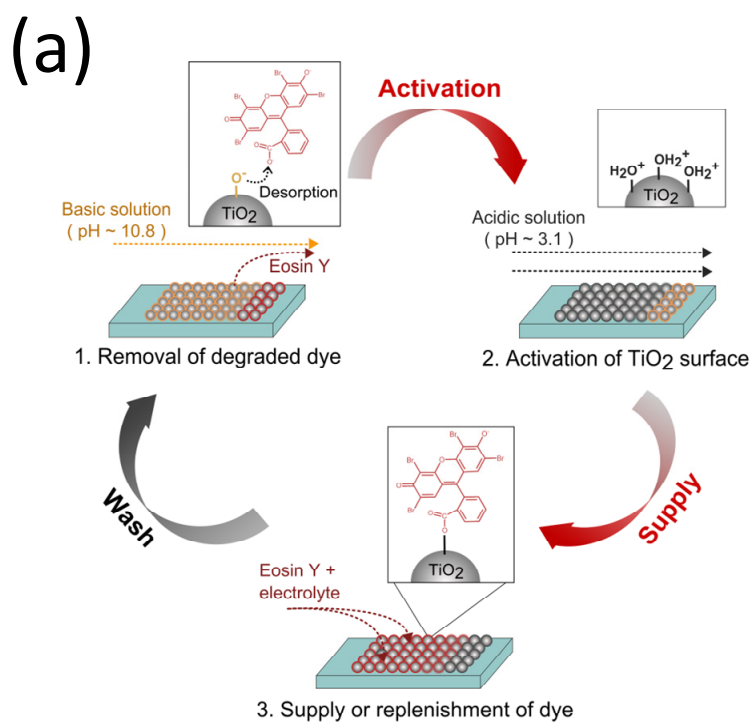


Figure 7.4. (a) The regeneration process of the μ -FGPVs. (b) Repetitive recovery of the photocurrent exhibited by the μ -FGPVs.

conduction band of the TiO_2 to generate electricity.²⁴ The adsorption/desorption kinetics of the photoactive dye molecules on TiO_2 surfaces depends on the pH of the environment, which thus becomes the key parameter to control the the regeneration process. The regeneration process begins with the step 1 of injection of basic aqueous NaOH solution with pH 10.8. Since the isoelectric point of TiO_2 is pH 6.2, the Eosin Y molecules on TiO_2 become ionized and are desorbed from the TiO_2 film under the basic pH environment.²⁴ The desorbed dye molecules and the electrolytes are washed out by the flowing basic solution. The TiO_2 treated with the basic solution acquires a negatively charged surface. This charge would hinder the re-adsorption of the fresh Eosin Y molecules, which are also negatively charged, because of electrostatic repulsion. To modify the surface charge of the TiO_2 , an acidic aqueous HCl solution with pH 3.1 is injected in the step 2 of an “activation” process. The activated TiO_2 film has a positively charged surface, where the negatively charged Eosin Y molecules readily adsorb when the solution of the fresh dye and electrolytes is replenished in step 3. The photocurrents from the μ -FGPVs during three operation cycles are shown in Figure 7.4 (b), where the J_{sc} is reliably recovered by the regeneration process. Thus, the μ -FGPVs can be regenerated by replacing the dye molecules with the process designed to be broadly similar to the regeneration functionality of a natural leaf.

We compared the recovery of the photocurrent generation of the μ -FGPVs with and without the acid treatment in Figure 7.5 (a) to prove the importance of the activation step. When the solution of dye and electrolytes is re-supplied after the regeneration process, the photocurrent is more than 100% recovered in the μ -FGPVs after both washing and activation processes, while little recovery of the photocurrent is observed in the cells without the activation processes. The $\approx 10\%$ increase of the photocurrent after the regeneration process is possibly a result from more favorable dye adsorption because of the surface charge modification. Note that the TiO_2 film was not treated with the acid solution to activate the surface before the first dye supply. We also investigated the effect of the duration of the activation step on the photocurrent recovery (Figure 7.5 (b)). The injection time of the aqueous acidic solution was varied from 1 to 5 hr at a rate of 10 $\mu\text{l}/\text{min}$. The photocurrent is

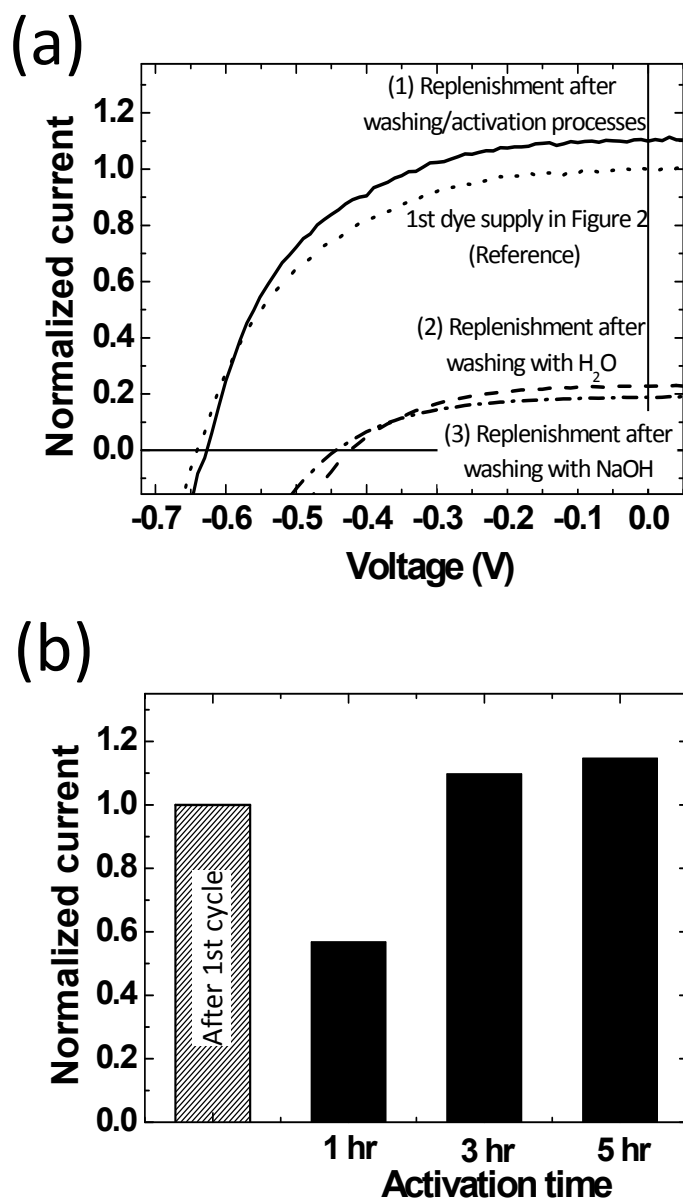


Figure 7.5. (a) I-V curves of the μ -FGPVs after different regeneration process, showing the importance of the activation step. The device (1) was washed with aqueous NaOH solution for 3 hrs, followed by treating with aqueous HCl solution for 3 hrs before the dye replenishment. The devices (2) and (3) were washed with H₂O or aqueous NaOH solution for 6 hrs, respectively, before the dye replenishment. All samples were measured after the 1hr dye-supply step. (b) Effect of the activation duration on the regeneration efficiency of the μ -FGPVs. The injection rate of all solutions is 10 μ l/min.

fully recovered when the TiO_2 is exposed to the acid solution for more than 3 hr. Less than 60% recovery of the photocurrent is recorded with the activation process lasting for 1 hr. Thus, an activation step longer than a minimum required time is essential for the reliable regeneration process. The minimum required time may depend on the injection flow rate. For example, higher injection rate of the acidic solution could shorten the minimum required time.

7.3.3. Demonstration of Regeneration of Photo-degraded μ -FGPVs

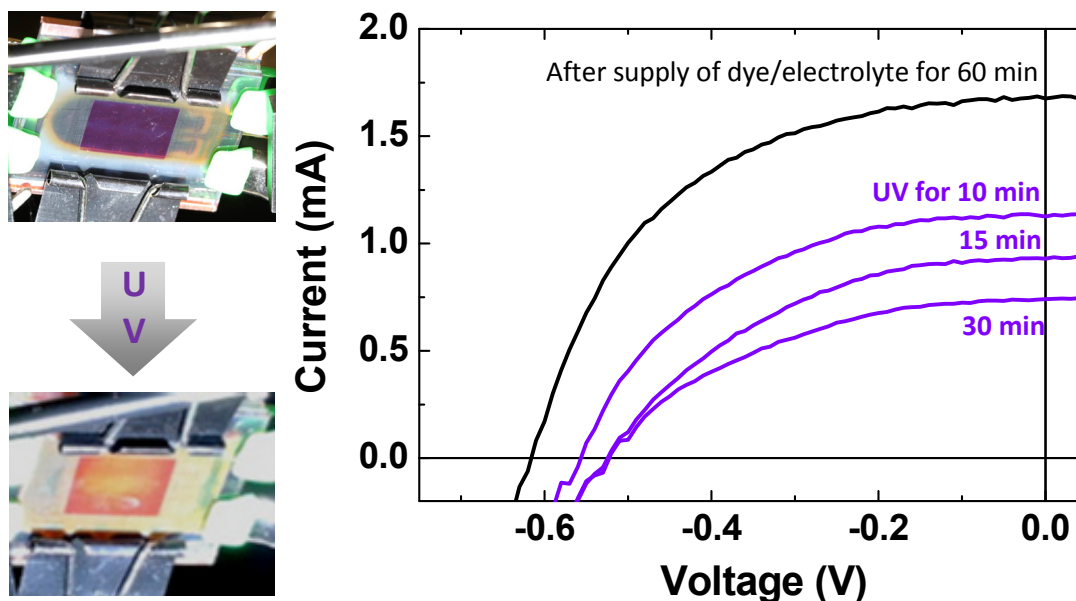


Figure 7.6. (Left) TiO_2 films before and after the intense UV illumination. The photographs were taken under illumination. (Right) The effect of UV illumination time on the photovoltaic performance of the μ -FGPVs.

We practically demonstrate the regeneration functionality of the μ -FGPVs by replacing the damaged photosensitive molecules with a stock of fresh ones. To accelerate the degradation process, the device was illuminated with highly intense UV light source (OmniCure S1000, High pressure 100 W Hg vapor short arc lamp, λ : 320 ~ 500 nm, Lumen Dynamics Inc.). The effect of UV illumination time on the photovoltaic performance of the μ -FGPVs is shown in Figure 7.6. The photocurrent decreases as the UV illumination time increases, due to the

photo-degradation of the Eosin Y dye molecules. The photocurrent of the μ -FGPVs measured during two UV-degradation/regeneration cycles is plotted in Figure 7.7. The photocurrent of the cell decreases by $\sim 40\%$ after the device is illuminated with UV for 10 min, and then is recovered with the successive regeneration process of washing, activation and dye-replenishment. During the second cycle, the photocurrent decreased by about 60% with the UV illumination for 30 min is also completely restored. Thus, we could successfully replace the photo-degraded dye molecules with fresh ones during the regeneration process, thereby realizing the self-reparation functionality of a natural leaf in the μ -FGPVs.

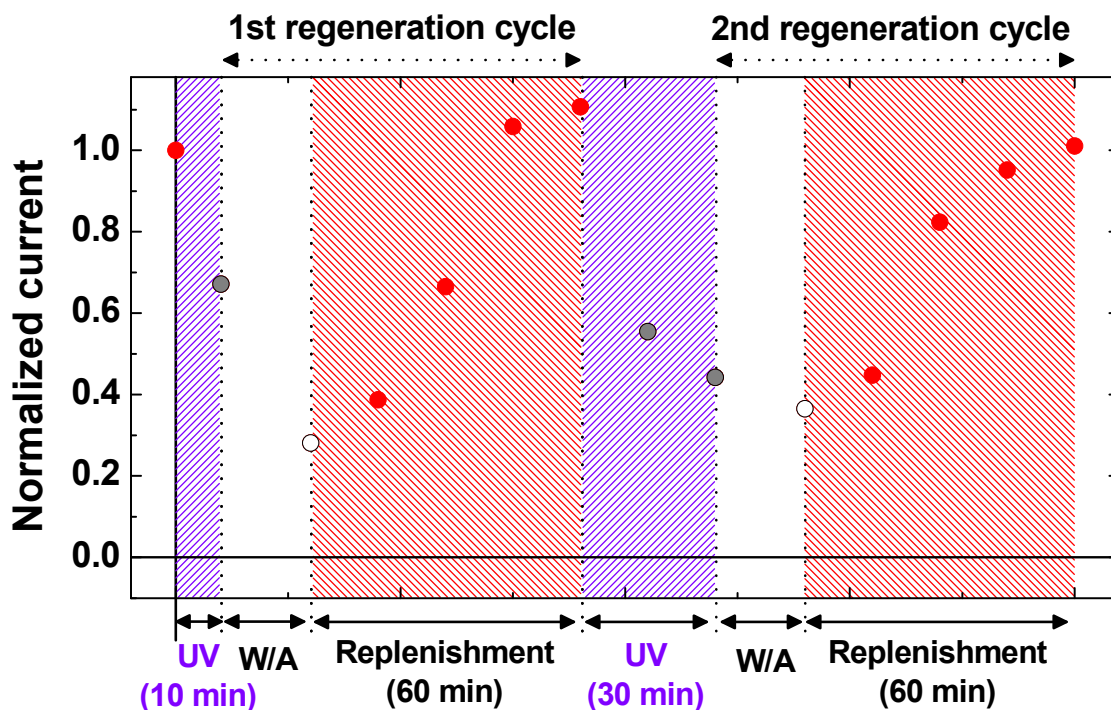


Figure 7.7. Demonstration of the photocurrent recovery of the μ -FGPVs after accelerated degradation by intense UV. W/A stands for the washing and activation steps. The device was washed and activated for 5 hr each. The violet and the red colored regions represent the periods of UV illumination and the dye replenishment, respectively.

7.4. Conclusions

In conclusion, we report a hydrogel based DSSC device with regeneration functionality. The microfluidic channels embedded in the hydrogel, inspired by the venation network sustaining

the vitality of live leaves, could enable the uniform supply of the photoactive dye molecules. We developed a reliable process for dye-replacement by mimicking the self-repair mechanism based on assembly and disassembly of the photosystems in a plant leaf. The key effect that allows to perform the process is the pH-dependent desorption/re-adsorption of the dye molecules on the TiO₂ photoanodes. Finally, we demonstrate the regeneration of the photocurrent of the μ -FGPVs deteriorated by accelerated degradation with the intense UV. These μ -FGPVs are constructed from a naturally derived water gel and biomimetic channel structure. The devices operate and regenerate by the processes resembling those occurring in a natural leaf. We believe that the design of these devices device demonstrates a highly promising path for the potential development of a practical artificial leaf.

7.5. References

1. O'Regan, B. & Grätzel, M. A low-cost, high-efficiency solar cell based on dye-sensitized colloidal TiO₂ films. *Nature* **353**, 737-740 (1991).
2. Grätzel, M. Photoelectrochemical cells. *Nature* **414**, 338-344 (2001).
3. Koo, H.-J., Chang, S. T., Slocik, J. M., Naik, R. R. & Velev, O. D. Aqueous soft matter based photovoltaic devices. *J. Mater. Chem.* **21**, 72-79 (2011).
4. Hinsch, A. *et al.* Long-term stability of dye-sensitized solar cells. *Prog. Photovoltaics Res. Appl.* **9**, 425-438 (2001).
5. Greijer Agrell, H., Lindgren, J. & Hagfeldt, A. Degradation mechanisms in a dye-sensitized solar cell studied by UV-VIS and IR spectroscopy. *Sol. Energy* **75**, 169-180 (2003).
6. Uam, H.-S., Jung, Y.-S., Jun, Y. & Kim, K.-J. Relation of Ru(II) dye desorption from TiO₂ film during illumination with photocurrent decrease of dye-sensitized solar cells. *J. Photochem. Photobiol. A* **212**, 122-128 (2010).
7. Sommeling, P. M., Späth, M., Smit, H. J. P., Bakker, N. J. & Kroon, J. M. Long-term stability testing of dye-sensitized solar cells. *J. Photochem. Photobiol. A* **164**, 137-144 (2004).
8. Grätzel, M. Conversion of sunlight to electric power by nanocrystalline dye-sensitized solar cells. *J. Photochem. Photobiol. A* **164**, 3-14 (2004).

9. Grünwald, R. & Tributsch, H. Mechanisms of instability in Ru-based dye sensitization solar cells. *J. Phys. Chem. B* **101**, 2564-2575 (1997).
10. Nour-Mohhamadi, F., Nguyen, S. D., Boschloo, G., Hagfeldt, A. & Lund, T. Determination of the light-induced degradation rate of the solar cell sensitizer N719 on TiO₂ nanocrystalline particles. *J. Phys. Chem. B* **109**, 22413-22419 (2005).
11. Toivola, M., Peltokorpi, L., Halme, J. & Lund, P. Regenerative effects by temperature variations in dye-sensitized solar cells. *Sol. Energy Mater. Sol. Cells* **91**, 1733-1742 (2007).
12. Aro, E.-M., Virgin, I. & Andersson, B. Photoinhibition of photosystem II. Inactivation, protein damage and turnover. *Biochim. Biophys. Acta, Bioenerg.* **1143**, 113-134 (1993).
13. Ham, M.-H. *et al.* Photoelectrochemical complexes for solar energy conversion that chemically and autonomously regenerate. *Nat. Chem.* **2**, 929-936 (2010).
14. Koo, H.-J. & Velev, O. D. In preparation.
15. Tributsch, H. Reaction of excited chlorophyll molecules at electrodes and in photosynthesis. *Photochem. Photobiol.* **16**, 261-269 (1972).
16. Kay, A. & Graetzel, M. Artificial photosynthesis. 1. Photosensitization of titania solar cells with chlorophyll derivatives and related natural porphyrins. *J. Phys. Chem.* **97**, 6272-6277 (1993).
17. Hagfeldt, A. *et al.* Verification of high efficiencies for the Grätzel-cell. A 7% efficient solar cell based on dye-sensitized colloidal TiO₂ films. *Sol. Energy Mater. Sol. Cells* **31**, 481-488 (1994).
18. Koo, H.-J. & Velev, O. D. Submitted.
19. Wang, Z.-S., Sayama, K. & Sugihara, H. Efficient eosin Y dye-sensitized solar cell containing Br⁻/Br³⁻ electrolyte. *J. Phys. Chem. B* **109**, 22449-22455 (2005).
20. Lee, W.-J., Okada, H., Wakahara, A. & Yoshida, A. Structural and photoelectrochemical characteristics of nanocrystalline ZnO electrode with eosin-Y. *Ceram. Int.* **32**, 495-498 (2006).
21. Guillén, E. *et al.* Photovoltaic performance of nanostructured zinc oxide sensitised with xanthene dyes. *J. Photochem. Photobiol. A* **200**, 364-370 (2008).
22. Koo, H.-J. *et al.* Nano-embossed hollow spherical TiO₂ as bifunctional material for high-efficiency dye-sensitized solar cells. *Adv. Mater.* **20**, 195-199 (2008).

23. Pichot, F. o. & Gregg, B. A. The photovoltage-determining mechanism in dye-sensitized solar cells. *J. Phys. Chem. B* **104**, 6-10 (1999).
24. Wang, Q., Chen, C., Zhao, D., Ma, W. & Zhao, J. Change of adsorption modes of dyes on fluorinated TiO₂ and its effect on photocatalytic degradation of dyes under visible irradiation. *Langmuir* **24**, 7338-7345 (2008).

Chapter 8

Summary and Future Outlook

8.1. Summary

The main goal of my dissertation is to create new functionalities in hydrogel based devices. Agarose hydrogel is soft, moldable and biocompatible and can achieve high ionic conductivity upon addition of electrolytes. We reveal that the advantages allow hydrogels to be a core material for new biomimetic devices. Moreover, the porous hydrogels with embedded microfluidic networks intrinsically form hierarchical channels mimicking the venation network of a natural leaf. The convective and diffusive transport mechanism in the microfluidic hydrogel could assist uniform and efficient supply of solutes.

In the first project, we described an ionic current rectification at the interface of SiO₂ film and water and demonstrated an electrochemical diode with conducting Si, SiO₂ nanolayer and aqueous gel interfaces, named SNAGI diode (Chapter 2). Compared to water media, the hydrogel media improved ionic conductivity and rectifying performance of the diode, presumably because of the charged backbone of the agarose polymer. The rectification performance depended on the agarose concentration and was maximized at the optimum concentration of 0.5 wt.%. The provisional mechanism proposed was based on gating of proton ions by the negatively charged SiO₂ nanolayer. The ionic conductivity was further improved by adding salt and polyelectrolytes so that an extremely high rectification ratio of more than 3×10^4 was achieved. The ionic current based diode showed good rectification under AC bias up to a frequency of 100 Hz. Stable encapsulation of water by the hydrogel media enabled reliable operation for more than 90 min, compared to only water media where the rectification function deteriorated within 50 min. The SNAGI diode is biocompatible, scalable and easy to prepare.

By replacing the solid electrodes of the SNAGI diode with liquid metal, we presented a new type of diode composed entirely of soft materials (Chapter 3). The device consisted of hydrogels interfaced with liquid metal alloy of gallium and indium (EGaIn). The effect of ionic conductivity, pH environment and the presence of an agarose network on the ionic current rectification in EGaIn/electrolyte/Pt diode was thoroughly investigated, towards better understanding of electrochemical phenomena on the EGaIn surface. Two hydrogel layers doped with different polyelectrolytes and sandwiched between the liquid metal

electrodes offer media for ionic transport and control the local pH. Since little oxide skin is formed on the surface of one electrode, the formation or dissolution of an insulating oxide layer on the surface of the other electrode determined the resistance of the whole device. Due to the ionic current-based operation, such a device can potentially function in aqueous environments where regular circuits will be unusable. The all soft matter based devices have potential applications in bioelectronic circuits, artificial neural networks and brain-machine interfaces.

Since the rectifying junction is a key component for photovoltaic operation, we developed a new type of a hydrogel based solar cell by extending the gel based diode concept (Chapter 4). Two photosensitive ions, DAS^- and $[\text{Ru}(\text{bpy})_3]^{2+}$, were used as photoactive molecules embedded in a matrix of water-based agarose. The provisional mechanism of the operation of the hydrogel photovoltaics (HGPsVs) suggests that the dye ions cooperatively work and contribute to the photocurrent generating process both on the surface of the working electrode and in the bulk of the gel. To reduce the cost of HGPsVs without efficiency loss, we found an efficient replacement of the expensive Pt counter electrode by using inexpensive copper coated with carbon materials. A flexible version of HGPsVs was constructed by replacing the rigid glass electrode with a conducting plastic substrate. Biologically derived photoactive molecules, such as Chlorophyll and Photosystem II, were successfully operated in the aqueous gel media of HGPsVs.

The next project demonstrated a light-induced photoreactor based on hydrogel media, which was inspired from a leaf, a natural photoreactor with venation networks (Chapter 5). Due to the thermally reversible sol-gel transformation, the microfluidic channels could be formed in the highly moldable agarose gel by a simple replica molding technique. Photocatalytic particles were embedded and immobilized in the porous gel matrix. Uniform supply of reactants and extraction of products were achieved through the microfluidic network. As an example of a photo-induced reaction, photocatalytic degradation of Methylene Blue and Allura red dyes was demonstrated in the gel reactor. The photocatalyst particles were three dimensionally distributed in the gel, which could facilitate adsorption for the catalytic reaction of the supplied reactants on the catalyst surface. Quantitative analysis of

the photocatalytic degradation rate revealed that the quantum efficiency per catalyst mass of the reactor was higher than those of the recently reported microfluidic reactors. Furthermore, a computational study was performed to understand the transport of solutes in the hydrogel with embedded microfluidic networks (Chapter 6). Two physical phenomena, fluid transport in porous and non-porous media and convection and diffusion of solutes, were the basic mechanisms for the modeling study. Numerical parameters, such as coverage and efficiency, were defined to optimize the channel designs. The dependence of the solute delivery rapidity and efficiency on the channel dimensions and shapes was numerically investigated based on the defined parameters. The validity of the computational study was proven by comparing the simulated results with the experimental data of the temporal infusion of dye solutes in the microfluidic gel media.

Finally, we constructed microfluidic photovoltaics with regeneration functionality (Chapter 7). The hydrogel medium with embedded microfluidic channels uniformly supplied the photovoltaic reagents, such as the photosensitive dye molecules and the redox electrolytes. A reliable process for the replacement of the dye molecules was developed, inspired by the regeneration functionality of photoactive proteins in a plant leaf. The adsorption and desorption of the molecules were controlled by adjusting the pH environment. We demonstrated the regeneration of a prototype device by replacing the dye molecules damaged by the accelerated UV illumination. The open-fluidic concept of the photovoltaic device enabled the discharge and the replenishment of the dye molecules. Such gel based and microvascular channel embedded photovoltaic concepts could allow constructing biomimetic photovoltaic systems with unprecedented functionality.

8.2. Future Outlook

During my Ph.D research, I have tried to construct new biomimetic devices by mimicking materials, structure and functionalities of a natural leaf. The agarose hydrogel used for the research is soft, hydrated and porous, similar to the tissue of a leaf. The channels embedded in the porous hydrogel, analogous to the hierarchical structure of a leaf venation network, help the uniform supply of reagents into a working body of a device. The energy harvesting

photoreaction and the molecular regeneration, inspired by the events occurring in a leaf, have been realized in the gel based devices. Hydrogel based photovoltaic devices with bio-inspired structure and functionality of the last project were constructed on the basis of the knowledge and experience obtained during the work described in the previous chapters. I believe the results prove that the microfluidic hydrogel could be a novel platform for a biomimetic energy harvesting system.

The next step of the development of regenerative hydrogel photovoltaics will be the replacement of the synthetic dye molecules with biologically derived photosensitive molecules. It was proven by the work in Chapter 3 that the photoactive bio-molecules, such as chlorophyll and photosystems, could be successfully used in the hydrated gel medium. An important task to be done for the short-term goal is to find an efficient way for the controllable assembly/disassembly of the bio-molecules on a working electrode. The assembly of the bio-molecules on the electrode surface would facilitate the transport of electrons generated in the molecules for high photocurrent generation. Also, the bio-molecules should be able to be assembled and disassembled on demand for regenerating the molecules when photoinduced damage occurs. The bio-molecules will be modified to contain functional groups for the facile assembly/disassembly on the electrode. The combinations of the functional groups on the bio-molecules and the electrode surfaces will be carefully chosen. The simplest example is to modify the chlorophyll molecules to have many carboxylic acid groups. The modified chlorophyll molecules can be regenerated on TiO₂ electrode via the regeneration process by pH-dependent adsorption/desorption, as described in Chapter 7. Moreover, the attached carboxylic acid groups could convert the hydrophobic chlorophyll to hydrophilic, thereby making them more soluble in water. The other possible option is the combination of thiol-modified bio-molecules and gold electrodes. It is well known that thiol groups exhibit strong binding on gold surface. This binding has been used for anchoring photosynthetic molecules on gold substrates to generate photoelectricity. Since the thiol-gold binding is possibly unstable under UV light, the thiol-modified bio-molecules could be disassembled naturally or by additional UV illumination procedures.

Another potential future goal of the project is biomimetic fuel cells based on biomaterial-embedded hydrogels. Microorganisms, which consume organic substances (fuel) to generate electricity, could be three-dimensionally distributed and immobilized in a hydrogel medium, which will be used for anode compartment of the fuel cells. Microvascular channel networks formed in the hydrogel, could enable uniform and efficient supply of fuel solutions. Conducting materials with 2-D shapes, such as carbon nanotubes, metal nanowires and conjugated polymers, are uniformly dispersed in the hydrogel matrix to provide electrical connectivity between the microorganisms and the electrode. In this concept of biofuel cell device, a regeneration functionality could also be realized. For example, dynamic control of the pore size of the hydrogel medium could allow immobilization of the fresh organisms or discharge of the damaged ones. Such strategies will help us to eventually construct entirely biomimetic energy harvesting systems based on the novel hydrogel platform.